



Technische Universität München

TECHNISCHE UNIVERSITÄT MÜNCHEN

Fakultät für Physik

Lehrstuhl: Prof. Dr. Winfried Petry

**Investigation of strain induced martensite transformations
kinetic in Austempered Ductile Iron (ADI) using neutron
and synchrotron diffraction**

Xiaohu Li

Vollständiger Abdruck der von der Fakultät für Physik der Technischen
Universität München zur Erlangung des akademischen Grades eines

Doktors der Naturwissenschaften

genehmigten Dissertation

Vorsitzende: Prof. Dr. Nora Brambilla

Prüfer der Dissertation: 1. Prof. Dr. Winfried Petry

2. Prof. Dr. Wolfram Volk

Die Dissertation wurde am 18.12.2017 bei der Technischen Universität München eingereicht
und durch Fakultät für Physik am 01.03.2018 angenommen.

PREFACE

The present thesis is submitted for a Ph.D degree from the Technische Universität München (TUM). The work presented in this thesis has been carried out at the Faculty of Physics and Research Neutron Source Heinz Maier-Leibnitz (FRM II) under the supervision of Prof. Dr. Winfried Petry and Prof. Dr.-Ing. Wolfram Volk during the period Juli 2013 to April 2017.

Garching bei München, Juli 2017

Xiaohu Li

ACKNOWLEDGEMENTS

First, I would like to thank all my family for supporting and caring me in all aspects of my life in Germany. Such economic and spiritual support on me is one of the most important essential conditions for completion of my studies in Germany.

Also thanks to Prof. Dr. Winfried Petry and Prof. Dr.-Ing. Wolfram Volk for providing a very interesting research project and a doctoral position for me and let me to participate in the study.

In addition, I would like to give my special thanks to Dr. Michael Hofmann for his full support during my Ph. D study. He gave me not only enough patience and thinking space, but also made the best efforts to coordinate the various departments of the technical staff to help me completing my experimental ideas. He gave me lot of opportunities to participate in different academic conferences, help me improving my express ability and broadening my knowledge. Such full support in the work during the Ph. D study is rare as I know. I am honoured to meet such a Ph. D adviser.

Many different material characterization methods were used in this doctoral thesis. I have got strong support from my colleagues around me in the process of completing these experiments. To be particularly grateful to have Dr. Weimin Gan and Dr. Markus Hoebel, who completed the guidance of the most important experimental part of this thesis, taught me how to process and analyse the experimental data and have been actively involved in the discussion.

I also want to give my thanks to the technical support provided by Dr. Patrick Saal, Dr. Julia Wagner, Dr. Jürgen Peters and Mr. Peter Biber. There are many colleagues who have provided me with help, but I cannot list your names here one by one. I would like to express my gratitude to all of you.

ABSTRACT

The heat treatment process on ADI consists of austenitization, austempering and quenching to room temperature. Finally, ausferritic microstructure and nodule graphite formed in the ADI material. The parameters austempering time and temperature in the heat treatment process directly affect the morphology of ausferritic structure, which furthermore determine the mechanical properties of the material for industrial applications.

Scanning electron microscopy (SEM), transmission electron microscopy (TEM), atom probe tomography (APT) and small angle neutron scattering (SANS) investigations were carried out to quantify the relationship between heat treatment parameters and ausferritic microstructure. At the same time, the process of carbon redistribution during the heat treatment has been explored using in-situ synchrotron diffraction and APT.

The retained austenite in ausferrite is metastable and transforms into martensite during plastic deformation in a similar process as has been found in TRIP steels. The evolution of the martensite phase fraction as a function of plastic deformation has been quantitatively determined using Rietveld refinement of neutron diffraction data taking into consideration the influence of texture formation. Finally, the martensite volume fraction as a function of plastic strain could be modelled using an shear-intersection mechanism taking into account the content of alloying elements by directly measuring the corresponding martensite-start temperature M_s of the material.

Contents

1. Introduction.....	1
1.1 ADI heat treatment and phase transformation during the heat treatment	3
1.2 Microstructure of ADI	6
2. Aims and work program	8
3. Theoretical background	11
3.1 Neutrons and Synchrotron diffraction	11
3.1.1 Properties of neutron and synchrotron radiation	11
3.1.2 Instrumentation and methods	13
3.1.3 Neutron diffractometers STRESS-SPEC and SPODI	15
3.2 Texture	17
3.2.1 Representation of texture	17
3.2.2 Determination of texture with diffraction measurements	21
3.2.3 Texture in <i>bcc</i> and <i>fcc</i> metals	23
3.3 Martensitic transformation	26
3.3.1 Athermal and isothermal martensite	27
3.3.2 Stress and strain induced martensite	30
3.4 Model for strain induced martensitic transformation	33
3.4.1 Influence factors for strain induced martensitic transformation	33
3.4.2 Nucleation models	37
3.4.3 Relaxation of internal strain energy model	38
4. Experimental Procedures	40
4.1 ADI sample preparation	40
4.2 Optical microscopy	40
4.3 SEM and TEM	41
4.4 Tensile, compression and cold rolling experiment	41
4.5 In-situ synchrotron diffraction of ADI during heat treatment	42

4.6	Atom-Probe-Tomography	43
4.7	Determination of M_s -Start –Temperature	44
4.7.1	Dilatometer	44
4.7.2	Neutron diffraction	44
4.8	Small angle scattering using neutron diffraction	46
4.9	Texture analysis using neutron diffraction	47
4.10	Phase analysis using neutron diffraction	47
5.	Data analysis, Results and Discussion	49
5.1	Microstructure of ADI	49
5.1.1	Optical microscopy	49
5.1.2	SEM	50
5.1.3	TEM	52
5.2	Size distribution of different phases in ADI	59
5.2.1	Determination of size and strain using integral breadth and double Voigt method	59
5.2.2	Size distribution of austenite and ferrite using small angle scattering	63
5.3	Phase analysis and carbon content in unstrained ADI	71
5.3.1	Phase fraction of austenite and ferrite in ADI after heat treatment	71
5.3.2	Carbon diffusion during heat treatment	71
5.4	Atom-Probe-Tomography	78
5.4.1	Carbon content in austenite and ferrite	78
5.4.2	Carbon content at grain boundaries	82
5.4.3	Carbon gap	82
5.5	Martensite-Start Temperature	85
5.6	Texture analysis	88
5.6.1	Pole figures and ODFs of compressed and cold rolled ADI	88
5.6.2	Texture formation in compressed and cold rolled ADI	90
5.7	Phase analysis in deformed ADI	93
5.7.1	Deformation behavior of ADI	93

5.7.2	Phase analysis of tensioned, compressed and cold rolled ADI	96
5.8	Simulation and development of martensitic transformation model	199
6.	Summary and future work	102
7.	References	105
8.	Attachment	112
9.	Publication	117

NOMENCLATURE AND ABBREVIATIONS

ADI: Austempered ductile iron

APT: Atom probe tomography

A_s: Austenite-Start-Temperature

A_f: Austenite-Finish-Temperature

bcc: Body-centered cubic

bct: Body-centered tetragonal

b_n: Neutron scattering length

c: Velocity of light, 3×10^8 m/s

d: Sample-detector distance

d_{hkl}: Distance of lattice plane

fcc: Face-centered cubic

f_A: Austenite phase volume fraction

f_M: Martensite phase volume fraction

f_s: Saturation value of martensite phase volume fraction

FWHM: Full width of half maximum

$\Delta G^{\gamma \leftrightarrow M}(T)$: Gibbs free energy difference between austenite and martensite at temperature T

$\Delta G^{\gamma \rightarrow M}$: Driving force of martensite nucleation at M_s

hcp: Hexagonal close-packed

hkl: Lattice planes

K: Scherrer constant

KS: Kurdiumov-Sach

LD: Loading direction

m.r.d.: multiples of random distribution

M_s: Martensite-Start-Temperature

M_S^σ : The maximal Martensite-Start-Temperature caused by stress

M_d : above this temperature no strain-induced martensite can form

M_f : Martensite-Finish-Temperature

n (in equation (3.3)): Exponent dependent on material

n (in equation (3.4)): Deformation mode parameter

ND: Normal direction

NW: Nishiyama-Wassermann

ODF: Orientation distribution function

RD: Rolling direction

SANS: Small-angle neutron scattering

SADP: Selected area diffraction pattern

T_γ : Austenitization temperature

T_{Aus} : Austempering temperature

T_q : quenching temperature

TD: Transverse direction

TRIP: Transformation induced plasticity

uvw: Lattice directions

v : Velocity of particle

V : Size of martensite plate

\emptyset : Coefficient related to material

λ : Wave length

α (in equation (3.3)): Parameter dependent on stacking-fault energy

β : Velocity of particles with respect to the velocity of light

β (in equation (3.3)): Parameter related to chemical driving force

β (in equation (3.4) and in section 5.8): Stability of austenite

β (in section (5.2)): Integral breadth

Γ : Full width at half maximum

ε : Plastic strain

$\dot{\varepsilon}$: Strain rate

1. Introduction

Austempered ductile iron (ADI) has been designed and used in industry for over 40 years. It was first applied in the automobile industry in 1972 to reduce weight and save the total production cost of trucks. In the following decades, the mechanical properties of ADI such as tensile/yield strength, elongation, and abrasion resistance could be improved significantly due to progress in its production. It is nowadays being applied in many different kinds of industrial components like engine brackets, diesel injector clamps, annular gears and others on account of its high fatigue resistance, toughness and ductility [John00].

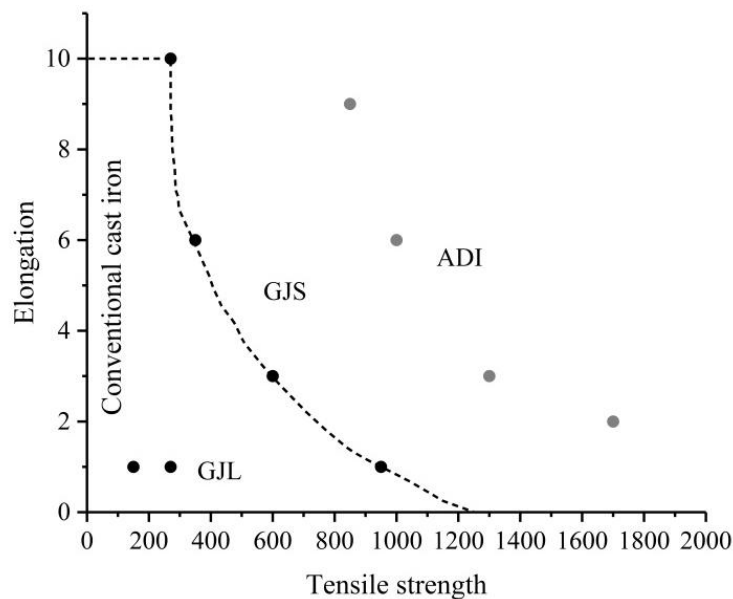


Figure 1.1 Comparison of cast iron properties [Jens03], GJS = Gusseisen mit Kugelgraphit, GJL = Gusseisen mit lamellarem Graphit (German name in new DIN EN 1563).

The predecessor of ADI is conventional cast ductile iron with nodular graphite (Gusseisen mit Kugelgraphit = GJS), a material that has high strength and ductility, which make it to play an important role in the casting industry. Compared to this conventional cast ductile iron, ADI has two major advantages. At first, with the same elongation ADI twice the tensile strength as conventional cast iron (Fig. 1.1) can be reached. In this respect, the tensile strength of ADI is comparable with many kinds of steel. However, compared to steels ADI as a typical cast iron offers the further advantage of free formability from the casting process as well as about 10% less density because of its high graphite content. Finally it is also 20% cheaper than the comparable aluminum component [Jens03] while showing better damping capacity [Jens03].

Its advantages in mechanical properties are mainly the benefit of its so-called ‘‘ausferritic’’ microstructure. More details about the ‘‘ausferrite’’ microstructure and its related heat treatment will be introduced in the following subchapters.

1.1 ADI heat treatment and phase transformation during the heat treatment

The base material cast ductile iron has to undergo a heat treatment involving the following steps to yield the characteristic ausferritic microstructure: (1) austenitization (880~1000°C), (2) quenching to austempering temperature (less than 30s), (3) isothermal austempering (250~450°C) and (4) finally cooling to room temperature. Figure 1.2 summarizes schematically the whole heat treatment process.

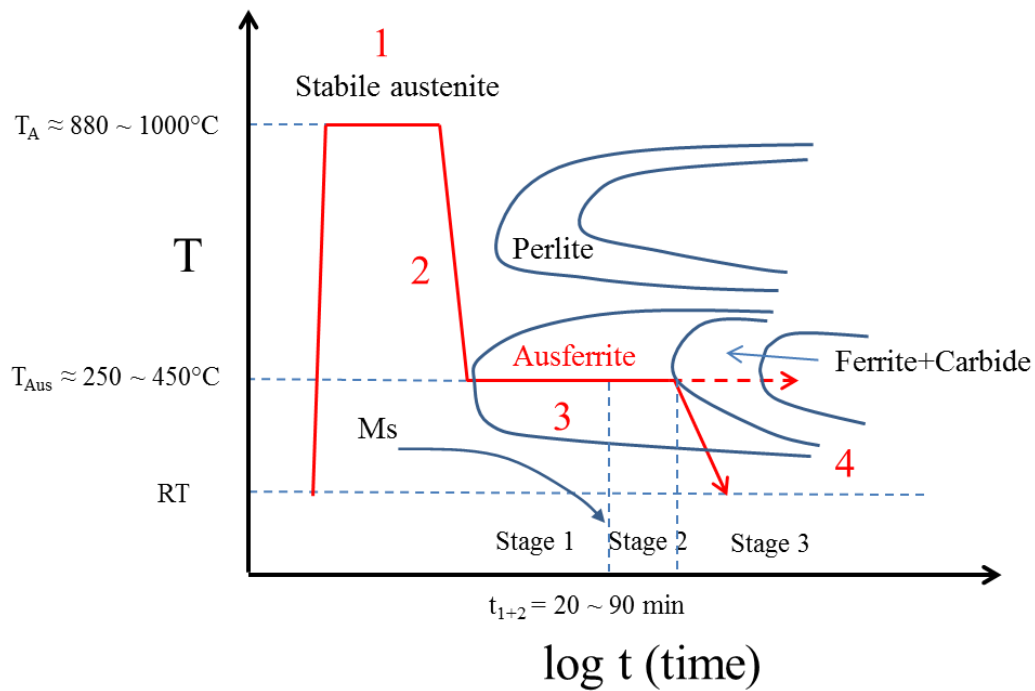


Figure 1.2 TTT-Diagram (Time-Temperature-Transformation) of ADI heat treatment process [Rund04].

The aim of the heat treatment is producing a microstructure of needle-like ferrite (*bcc* structure) in a carbon-supersaturated austenite (*fcc* structure) matrix. The high carbon content stabilizes the austenite matrix at ambient and even lower temperature. The base material cast ductile iron will be austenized in a furnace with inert gas or in a salt bath at least for 30 min, until complete carbon saturation of the austenite (900°C - 0.8 wt%, 950°C - 0.92 wt%) [Leop15] is reached.

The austenisation is followed by rapid quenching to austempering temperature T_{Aus} . High quench rates of around 20 K/s are needed in this step to avoid formation of pearlite (Fig. 1.2). The ADI sample is then hold isothermally at this temperature until the required microstructure is achieved. According to the phase transformations which take place during the isothermal austempering, the austempering can be differentiated in 3 stages (Fig. 1.2). The phase transformation and carbon diffusion taking place during austempering can be described with help of the Fe-Fe₃C phase diagram (Fig. 1.3).

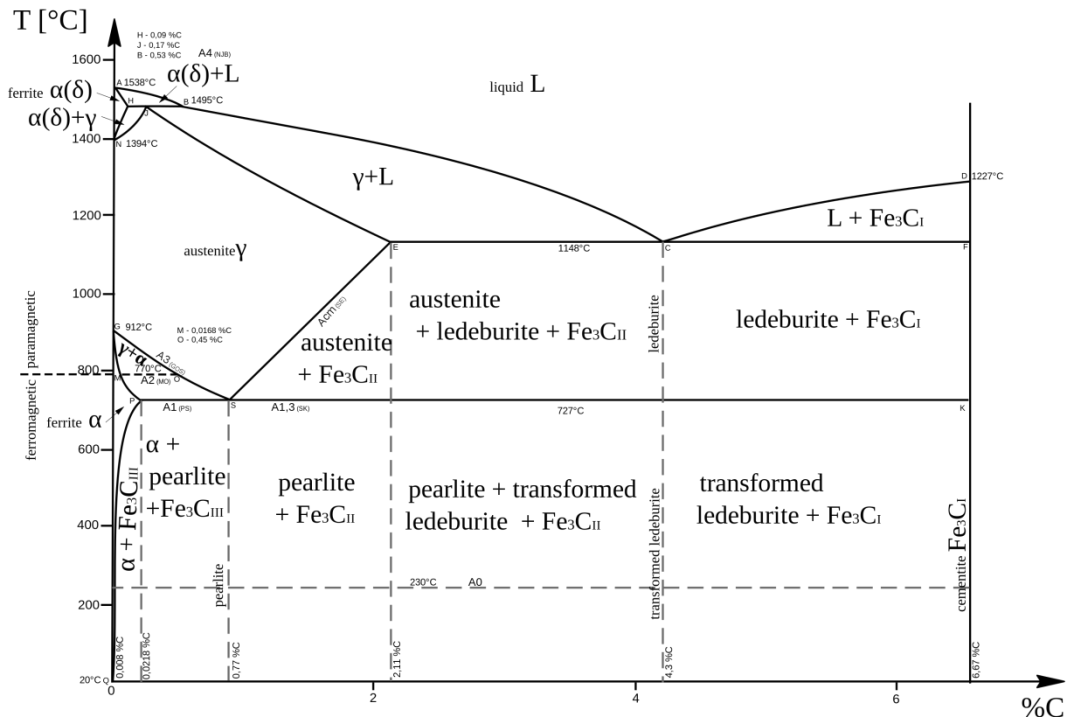


Figure 1.3 Fe-Fe₃C phase diagram [Www-02].

1. Stage: In the first stage, austenite will transform partly to ferrite which has much lower carbon solubility (0.02 wt%) than austenite (Fig. 1.3). Therefore the excess carbon atoms in ferrite are displaced and will diffuse into the surrounding austenite matrix and stabilize it so that further transformation ceases. From ex-situ observation of the isothermal austempering procedure using optical microscopy the directional relationship between austenite and ferrite has been determined [Leop15]. The transformation occurs first nearby the graphite nodules and extends away from the direction of the graphite [Leop15]. At the beginning of this stage, cooling too early to room temperature can cause a transformation of insufficiently stabilized austenite into martensite, which leads to embrittlement of the material. For this reason, the carbon content dependent minimum austempering time must never fall below the time until the carbon content in retained austenite has risen up to a plateau value of about 1.5~1.7 wt%, depending on the austempering temperature [Leop15]. The carbon diffusion between ferrite and austenite during austenite to ferrite transformation is well known and understood in many iron based austenitic alloys like QP (Quench&Partitioning) steel [Jspe03], AISI 316 steel [Jcer14] and ADI [Leop15]. At high austempering temperature of $T_{Aus} \geq 375^\circ\text{C}$, the carbon diffusion from ferrite to retained austenite will be finished almost simultaneously with the phase transformation [Leop15]. While if T_{Aus} is decreased, the carbon diffusion lacks behind the completion of phase transformation [Leop15].

2. Stage: The phase transformation rate drops to lower than 10^{-6} vol%/s [Psa15]. The duration of this stage depends on the austempering temperature [Leop15] and for ADI material production the isothermal austempering should be stopped here, before the Stage 3 reactions set in.

3. Stage: Austempering for too long a time leads to the carbide formation and thus also to the embrittlement of the material, which must be avoided (Fig. 1.2).

Depending on the austempering temperature the material should be austempered so that the amount of stabilized austenite is at maximum before subsequent cooling to room temperature.

The formation of microstructural defects like primary carbides, segregations and porosities etc. must be avoided. Such defects are almost impossible to be eliminated by heat treatment. Addition of other alloying elements into the ADI material is a possible solution to alleviate such problems.

1.2 Microstructure of ADI

In optical micrographs the ausferritic microstructure in ADI is quite similar to some kinds of bainitic microstructures in steel (Fig. 1.4 and 1.5). These are the result of the so-called bainitic isothermal transformation in steels [Hkdh05] which is quite similar to the austenite to ferrite transformation during the ADI heat treatment. However, there is a key difference between the resulting microstructures. Whereas bainite commonly consists of supersaturated ferrite and cementite, ausferrite consists of acicular ferrite and carbon enriched retained austenite, with no stable cementite being found in the ausferrite matrix.

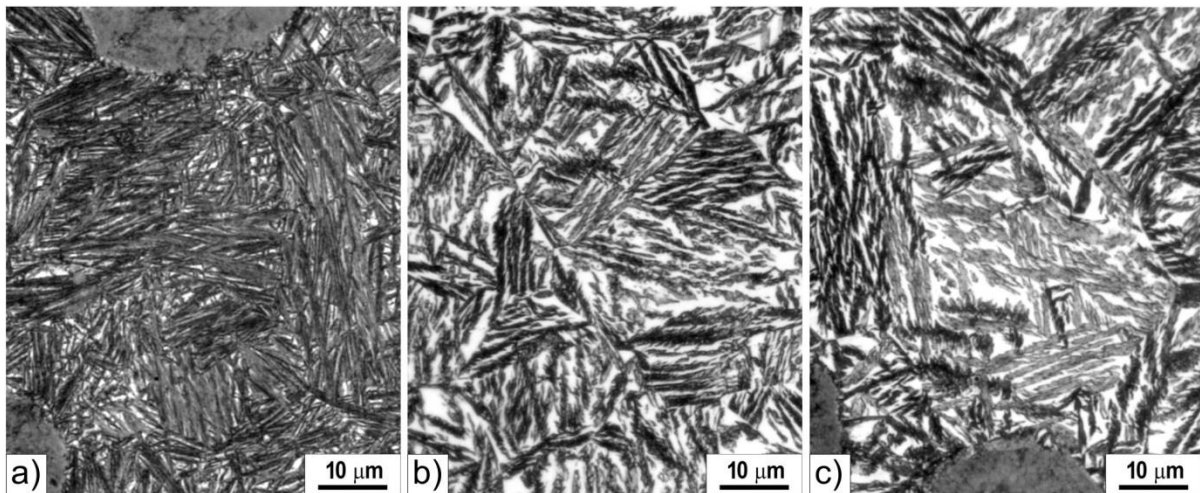


Figure 1.4 a) unalloyed ADI austempered at 300°C/1h, b) 400°C/1h and c) 2h, etched by 3% nital [Rajn14].

The morphology of ausferrite is transformation temperature dependent. The acicular ferrite formed at lower transformation temperature has a larger volume phase fraction and a much finer structure as the one formed at higher temperature (Fig. 1.4). Nowadays computational simulations, for example the one developed by Boccardo *et al*, are able to describe the whole formation process of ausferrite microstructure in ADI [Adbo17-1, Adbo17-2 and literature therein] and are confirmed by SEM and TEM results in this work. The amount and grain size of acicular ferrite determines the hardness and fatigue strength of the resulting ADI material, while the ductility is supported by the carbon enriched retained austenite, thus explaining the increase in ADI mechanical properties depicted in Figure 1.1. ADI austempered at lower temperature has higher tensile strength and smaller elongation while ADI austempered at higher temperature has the opposite properties. Through controlling the transformation temperature and holding time one can derive high strength ADI with relative low elongation or low strength ADI with relative high elongation. Because of the homogenous distribution of

acicular ferrite and retained austenite, the ADI material shows a higher toughness, fatigue strength and ductility as other types of cast iron and is even comparable to some bainitic steels.



Figure 1.5 Optical micrographs of bainite obtained at 200 °C [Yguo15].

2. Aims and work program

2.1 Aims

In this work, the relationship between preparation treatments, resulting microstructure and phase compositions will be highlighted. The understanding of structure – property – relationships is essential for any development of materials. The most important questions to be addressed within this work can be categorized into three topics:

1. Strain-induced martensitic transformation kinetic:

What is the relationship between plastic strain ε and strain-induced martensite phase volume fraction f_M ? Furthermore, can the relationship of other influence factors (like alloying content, grain size, strain rate ect) on the martensitic transformations kinetic be described using a mathematical model.

2. Grain size and distribution of ferrite, austenite and martensite:

What are the effects of austempering temperature and plastic strain on the grain size distributions in ADI materials?

3. Carbon gap and carbon distribution in ADI:

The disappearance of some carbon atoms in ferrite/austenite before and after austempering has been determined previously [Leop15, Psaa15]. The issue of missing carbon is called the carbon gap. Carbon gap has also been shown to be dependent on austempering temperature. Its specific relevance with austempering temperature needs to be quantified.

2.2 Work program

In order to answer the questions raised above, the following series of experiments have been planned and conducted:

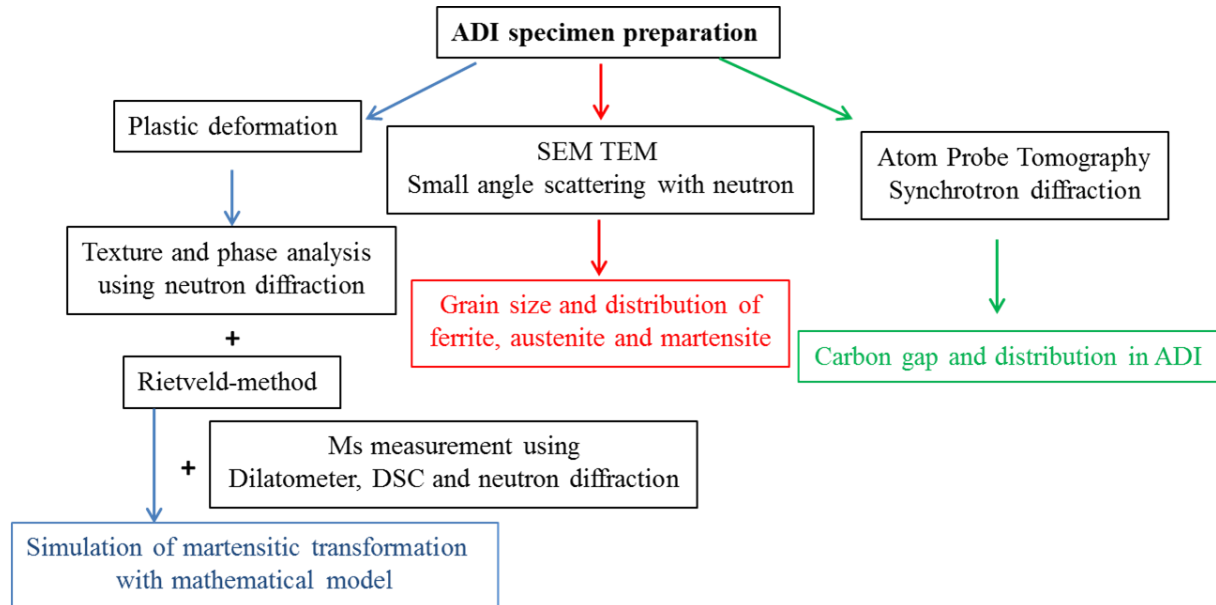


Figure 2.1 The main experimental procedures and techniques with respect to the specific aims (in colored boxes).

1. The strain-induced martensitic transformations kinetic in ADI under plastic deformation have been systematically investigated. ADI samples which have three different nickel contents typically used in industry (0 wt%, 0.5 wt% and 1.5 wt%) have been heat treated at different austempering temperatures T_{Aus} . The alloying element nickel has been shown to prevent the austenite-ferrite transformation from progressing, thereby increasing the final austenite content and enhancing the mechanical properties of the material. Its influence on the phase transformation in ADI during austempering has been investigated previously [Psaal5]. However, its impact on martensite-start temperature M_s in ADI has not been quantified. In this work, the samples were plastically deformed (tensile, compression and cold rolling) to different strain levels. Texture and phase information data were collected using neutron diffraction (section 5.6 and 5.7). Rietveld-refinement has been performed on the neutron powder diffraction data with combination of texture information. On the other hand, the M_s temperature of the prepared ADI samples was determined using dilatometry and neutron diffraction (section 5.5). A mathematical model was developed to explain the relationship

between the volume fraction of strain-induced martensite and its relevant influence factors (section 5.8).

2. SEM and TEM were used to observe the microstructure of ADI. The approximate grain size and shape of phases in ADI can be shown directly in SEM and TEM images (section 5.1). The grain size distribution of different phases can be estimated using small-angle neutron scattering (SANS) data (section 5.3). The relation between austempering temperature T_{Aus} and grain size distribution can be determined.

3. In-situ synchrotron diffraction with high time resolution was carried out on ADI samples during the heat treatment. Carbon diffusion in ferrite and austenite during the heat treatment was investigated by analysis of changes of their peak positions (section 5.2). Atom-Probe-Tomography was performed on ADI samples after heat treatment to investigate the carbon distribution in ADI and elucidate the possible reasons for the carbon gap (section 5.4).

3. Theoretical background

3.1 Neutron and Synchrotron diffraction

Neutron and synchrotron diffraction enable structural analysis of crystalline matter and offer a variety of applications in materials science, physics, chemistry, biology, medicine and other fields of research. Neutrons and synchrotron radiation have wavelengths in the range of atomic distances and share a number of physical properties, which make both of them powerful tools for material research. Nevertheless in certain aspects their properties are different, which allows distinguishing them between the ways, means of solving problems and the details in the practical applications. For a better understanding of their applications in the material research, their basic physical properties will be given in the following section.

3.1.1 Properties of neutron and synchrotron radiation

Neutron radiation is a particle wave, which can be described by Schrödinger equation. The neutron has a mass of 1.675×10^{-27} kg and its energy depends on this mass and its own velocity. On one hand, due to the interaction between neutrons and the nucleus particles in the scattering atoms, its scattering length b_n depends sensitively on the order number Z and the mass number A of the scattering atoms [Wrei06]. On the other hand, different to X-rays, the scattering length of neutrons, b_n , varies with relative small fluctuations throughout the whole periodic table, both of which allow identifying the elements with similar Z or even isotopes (difficult or even impossible with X-rays) (Fig. 3.1). Due to its uncharged nature, neutron radiation has a high penetration ability into solid materials (some mm to cm), which makes it possible to perform stress/strain and phase analysis in large specimen with a complicated geometry.

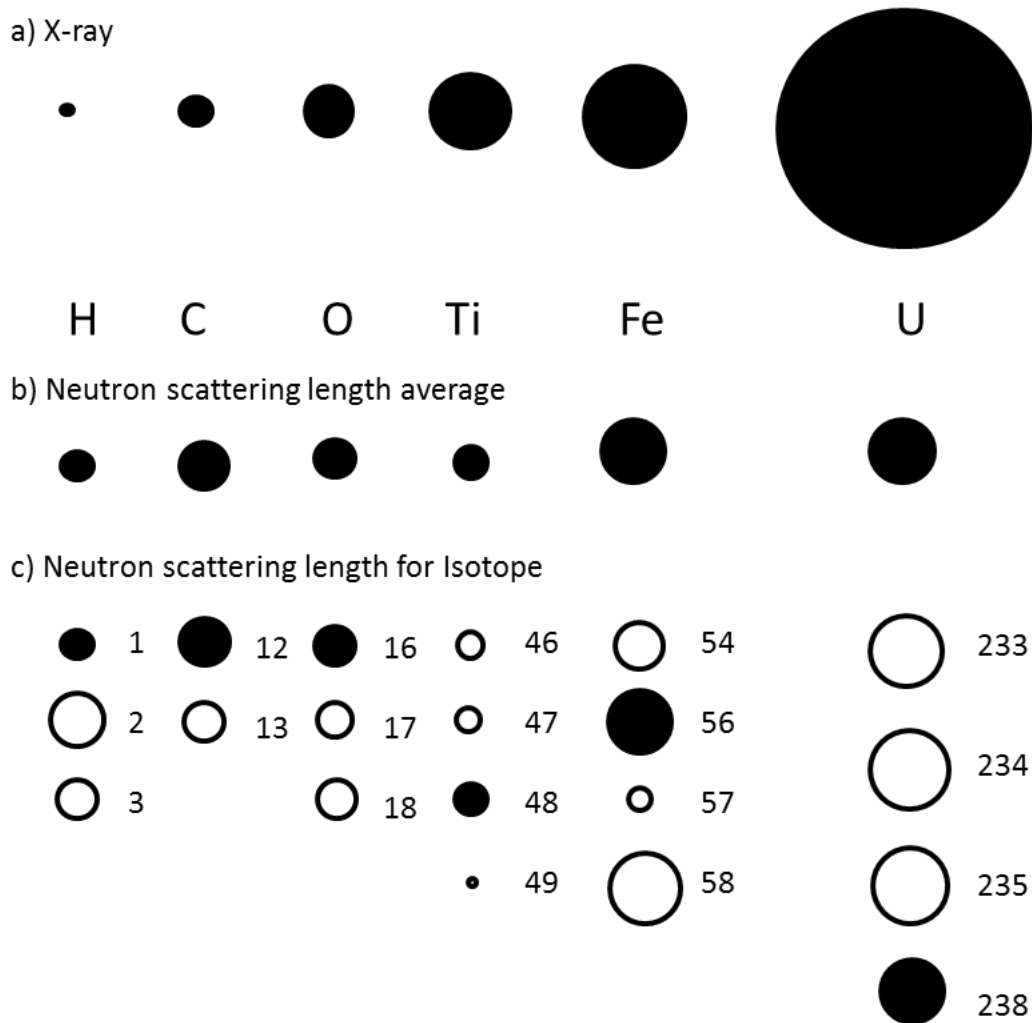


Figure 3.1 Scattering lengths for X-ray (a) and averaged for neutrons (b). The scattering length for each isotope of the respective element (c) [Wrei06].

However, the interaction between neutrons and scattering atoms is not only limited to the nucleus. The dipole moment of the neutron interacts with the magnetic moment of the atomic shells in the magnetically ordered materials, which leads to an additional interaction similar as the nuclear interaction. Due to this reason neutron diffraction became the classic research method in investigation of magnetic structures [Wrei06].

Synchrotron radiation is electromagnetic radiation emitted by charged particles (electrons and positrons), accelerated to relativistic velocities [Wrei06] (Fig.3.2).

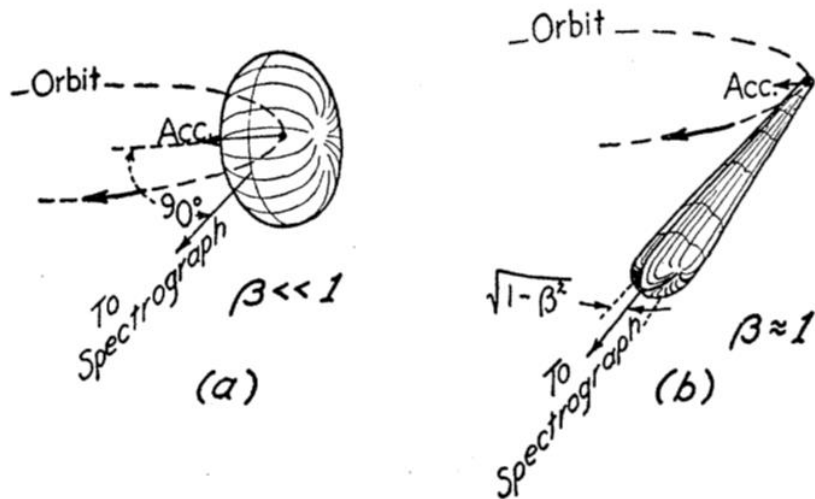


Figure 3.2 The electromagnetic radiation emitted from charged particles. (Left) The particles with nonrelativistic velocities at the low energy state. (Right) With relativistic velocity $\beta = v/c$, velocity of particles with respect to the velocity of light [Dhto56].

Synchrotron radiation has a continuous spectrum with a wavelength ranging from infrared to hard X-rays. Compared to neutron radiation the high intensity, small source size and high brilliance make the synchrotron radiation advantages for rapid kinetic measurements, experiments with small samples and some space resolved techniques. In order to make full use of their respective advantages in scientific research, neutron/synchrotron scattering facilities are equipped with dedicated scattering instruments and devices.

3.1.2 Instrumentation and methods

An overview of the experimental hall and neutron guide hall of the Research Neutron Source Heinz Maier-Leibnitz (FRM II MLZ) at TU Munich is shown in Figure 3.3 as an example.

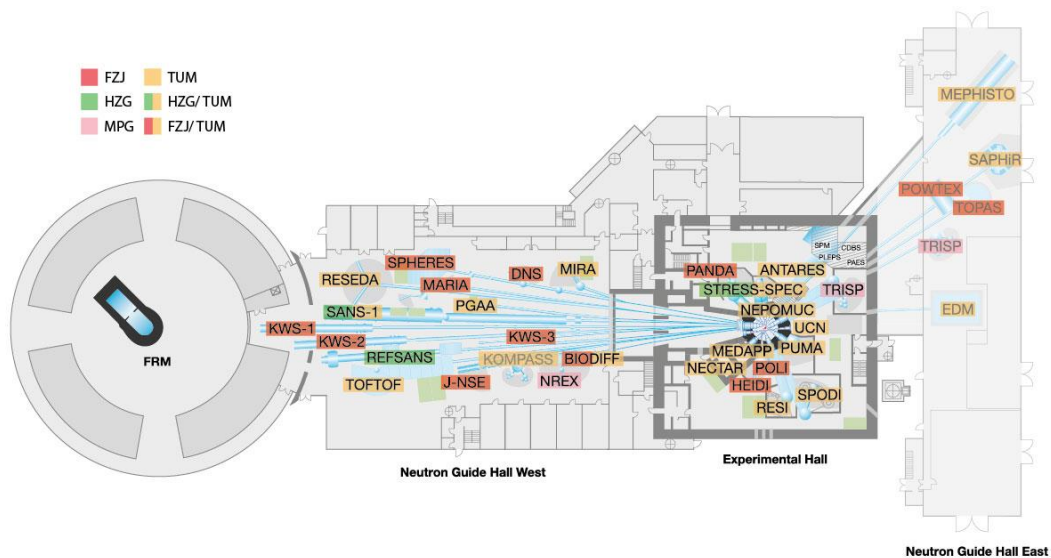


Figure 3.3 Instrument overview with corresponding partners (FZJ - Forschungszentrum Jülich, TUM – Technische Universität München, HZG – Helmholtz-Zentrum Geesthacht, MPG – Max Planck Gesellschaft) [Www-01].

Table 3.1 Selected instruments used in the current work and their main research areas in material science. ND: neutron diffraction, SD: synchrotron diffraction

Scientific field	Instrument (Radiation source)	Methods / Technique
Stress analysis	STRESS-SPEC (FRM II)	Angle-dispersive ND
Microstructure analysis	SANS-1 (FRM II) (PETRA III/DESY)	Small-Angle ND/SD
Texture analysis	Beamline P07 HEMS (PETRA III /DESY) STRESS-SPEC (FRM II)	Monochromatic ND/SD
Phase analysis	SPODI (FRM II)	Neutron powder diffraction

The neutron source FRM II offers a wide neutron spectrum ranging from ultra-cold to hot neutrons and has been equipped with over 30 different scattering instruments. Each instrument can be equipped further with different detectors and other related devices like robots, cryostats, light furnaces, magnets etc, used to change the experimental environment to satisfy the special requirements in the scientific research. Such a facility configuration makes the contribution of neutron research possible to progress in many scientific fields, especially in material science. The main research fields in the material science using neutron/synchrotron diffraction and their related instruments, methods are partly listed in table 3.1.

The instruments STRESS-SPEC and SPODI (FRM II) bear the main task of experimental measurements of this Ph.D thesis. Their basic configurations and scope of application will be introduced in detail in the next subchapter.

3.1.3 STRESS-SPEC and SPODI

The diffractometer STRESS-SPEC can be applied for residual stress analysis, texture determination and some structural applications (phase transformation dynamics, spatially resolved phase analysis) [Mhof15].

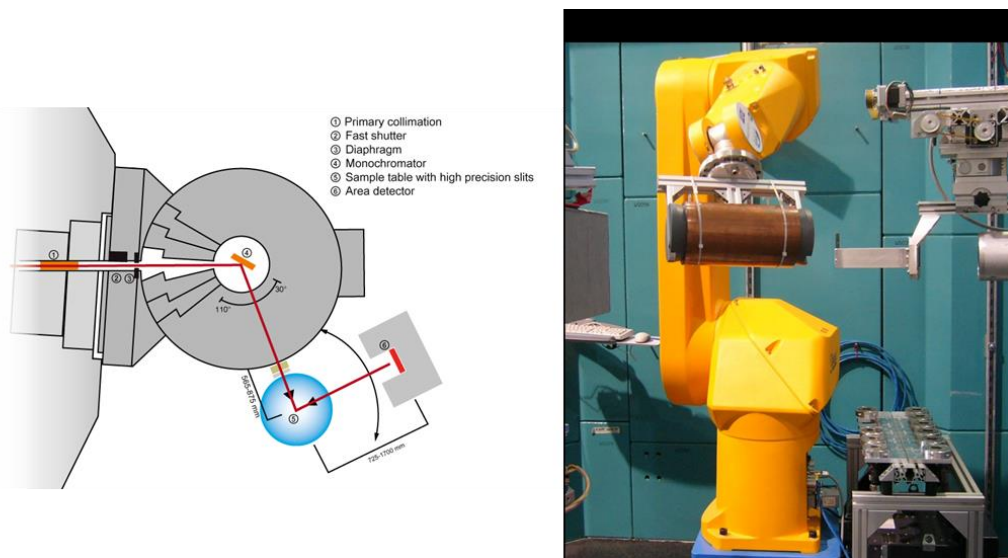


Figure 3.4 Schematic configuration of STRESS-SPEC (left) and Robot sample holder (right) [Mhof15].

STRESS-SPEC is situated at the thermal beam port SR-3 of FRM II. The instrument comprises a set of three different monochromators (Ge (511), Si (400) and PG (002)), a large sample table and a ^3He position sensitive area detector. With this setup and a continuous take-off angle from 35° to 110° a good balance of resolution and intensity can be realized for the different measuring problems. A 6-axes robotic arm can be used instead of the original sample table to offer even more flexible sample positioning and automatic sample changing.

Using a closed cycle cryostat and a high temperature furnace as devices the sample temperature environment can be controlled from 3 K to 2173 K. Thus solid phase transformations or magnetic structure changes within this temperature range can be determined quantitatively).

SPODI is a powerful instrument for structure solution and Rietveld refinement of crystal and magnetic structural parameters [Mhoe15]. The multi-detector system consists of 80 ^3He position sensitive detectors (each detector covers 2°) with 300 mm effective height. In front of

each detector, a 10° collimator is placed enabling good angular resolutions over the whole scattering angle regime. The good resolution is further supported by a large monochromator take-off angle of 155° .

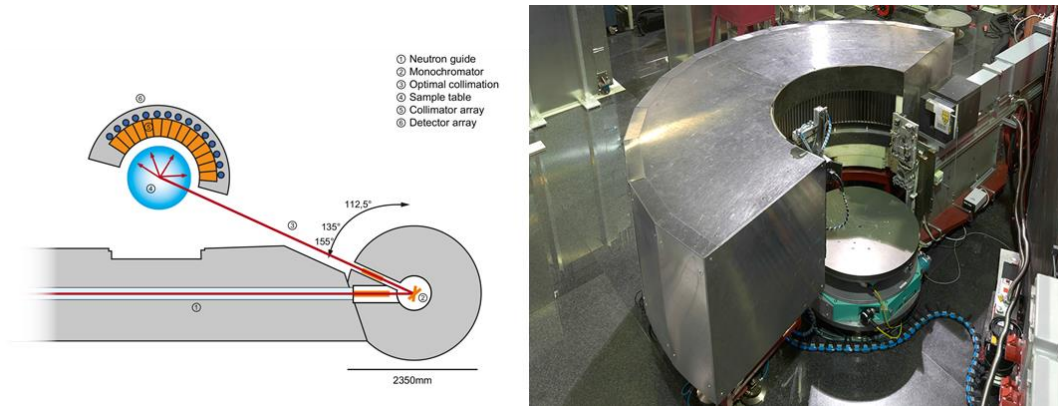


Figure 3.5 Schematic configuration of SPODI (left) and detector system (right) [Mhoe15].

3.2 Texture

Texture is defined as non-uniform distribution (or preferred orientation) of crystallographic orientations of individual grains within a polycrystalline material [Ufko98]. A polycrystalline material is equivalent to an aggregate of many single crystallites. The preferred orientation (texture) can be expressed by the Miller indices using two vectors in the form of $(hkl)[uvw]$, which is used to describe the crystallographic planes $\{hkl\}$ and plan directions $\langle uvw \rangle$ of a single crystal (Fig. 3.6). The detailed texture information is usually represented in the form of a 2-dimensional Pole figure or the 3-dimensional orientation distribution function (ODF). Many material properties like strength, stress resistance, deformation behaviors etc. are highly dependent on the texture in material. In addition, texture formation during plastic deformation also influences the results of quantitative phase analysis. In this subsection, the route to present the texture distribution, experimental texture measurements and texture development in face-centered cubic *fcc* and body-centered cubic *bcc* metals will be introduced.

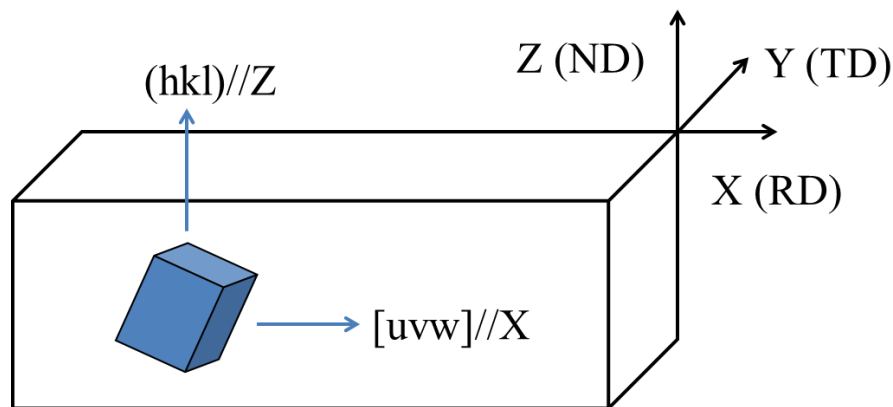


Figure 3.6 Orientation specification via $(hkl)[uvw]$ of a single crystal in a polycrystalline material. ND: normal direction, TD: transverse direction, RD: rolling direction.

3.2.1 Representation of textures

All the plane normals and directions in the 3D crystal structure can be represented as points on the reference sphere (Fig. 3.7 a). After projection onto a circle plane, the points on the reference sphere can be shown in a stereographic projection (Fig. 3.7 b).

When we now consider a polycrystalline specimen (Fig. 3.7 c), one can represent in similar fashion the relation between crystallite orientation and specimen geometry in the stereographic projection (Fig. 3.7 d). In case the grain orientations in the specimen are almost random or without texture, the pole densities in the pole figure are about 1 times random

(multiples of random distribution, *m.r.d.*), while in case of texture it is greater than 1 times random (Fig. 3.8).

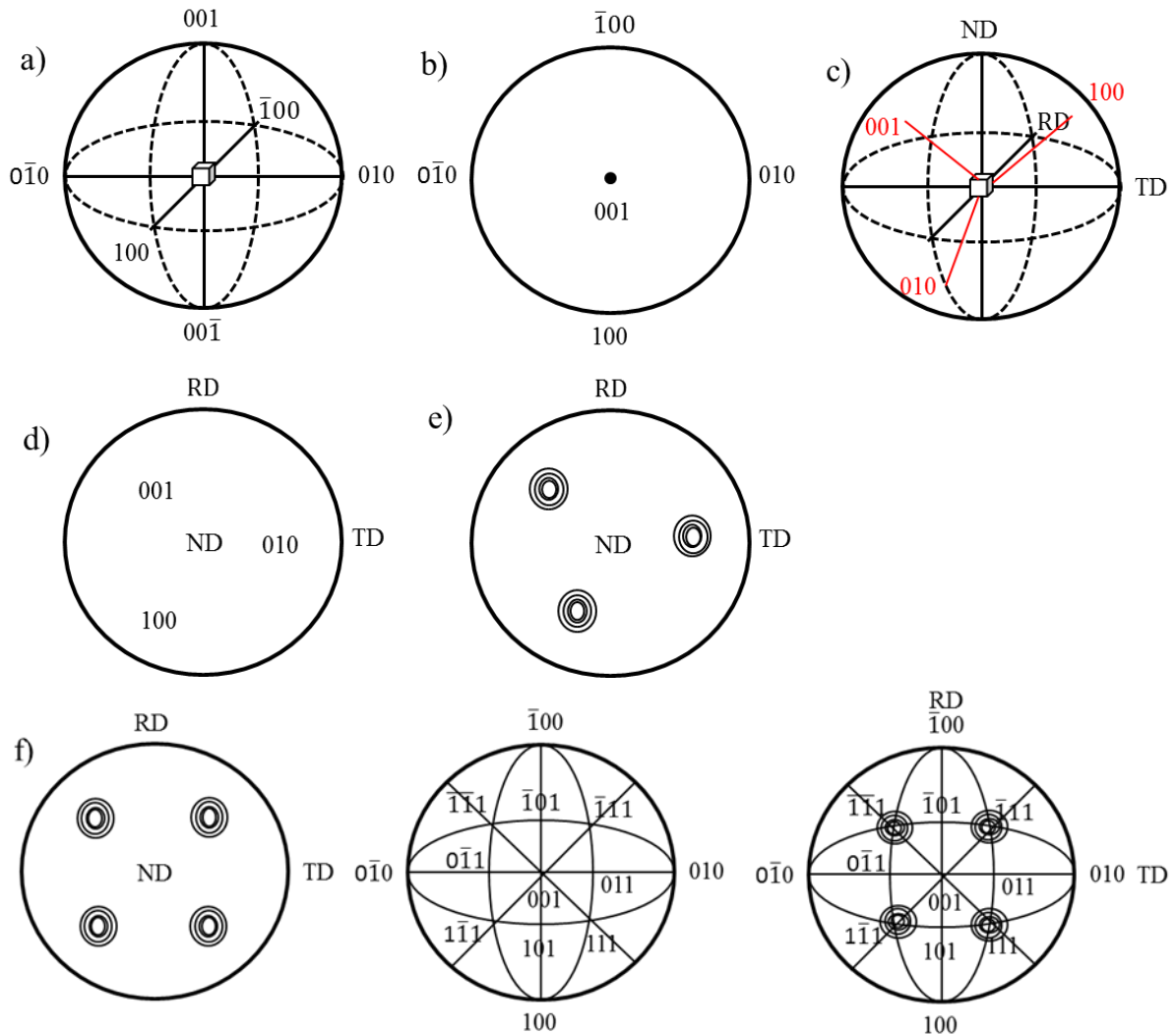
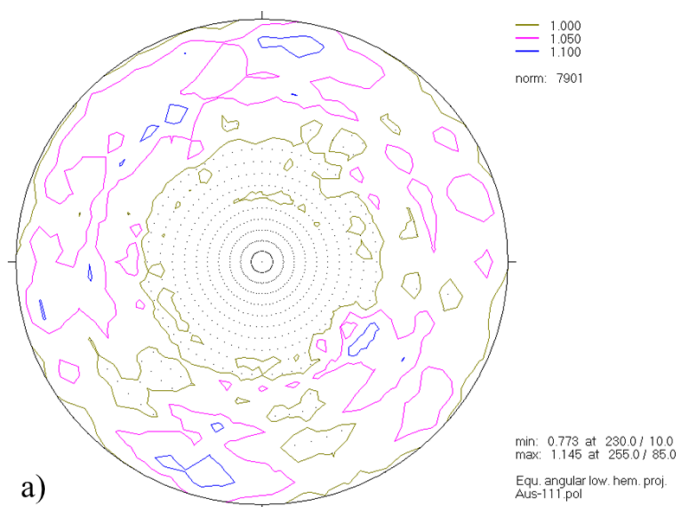


Figure 3.7 Representation of Pole figure after [Ssuw14].
 a) Plane normals of a cubic single crystal present at the center of the reference sphere.
 b) The (001) stereographic projection from (a).
 c) Plane normals of a grain in a polycrystalline specimen present on the reference sphere.
 d) The stereographic projection from (c) from ND (normal direction).
 e) Showing pole densities as contour lines.
 f) Comparison of pole figure and stereographic projection. Left: (111) Pole figure of a cold rolled specimen. Middle: (100) stereographic projection. Right: Pole figure and stereographic projection superimposed on each other.

The standard stereographic projection of a crystal system (cubic, hexagonal, tetragonal etc) is a particular mapping that projects the crystal orientations in a 3-D space onto a 2-D plane

[Ssuw14]. In a standard stereographic projection (for example: Figure 3.7 f, middle, 001 stereographic projection of cubic system), the normal direction of plane $(hkl) = (001)$ is chosen perpendicular to the projection circle and placed in the center. The information of other planes will be based on the spatial relationship with (001) plane projected on the corresponding positions of the (001) stereographic projection. Comparing the measured pole figures with standard stereographic projection, the texture orientation and specimen geometry can be easily read out (Fig. 3.7 f). For a correct comparison, it is necessary to define the coordinate system of the measured pole figures (Fig. 3.7 left, RD = rolling direction, ND = normal direction and TD = transverse direction to rolling as an example) and make sure that the stereographic projection and the projection plane of the measured pole figure have the same coordinate system. Otherwise the pole figures must be first rotated to the relevant stereogram.

As pole figures can be obtained directly through experimental measurements the procedure to show the crystal orientations and specimen geometry together in a 2-dimensional stereographic projection is an appropriate way to qualitatively describe the texture in a polycrystalline material. However, the crystal orientation in materials has a 3-dimensional structure, so that using 2-dimensional projection to describe the 3-dimensional structure will inevitably lead to loss of useful information. Therefore using the orientation distribution function (ODF) in a 3-dimensional space, whose coordinates are defined by 3 Euler angles (Φ , ϕ_1 , ϕ_2) to describe the distribution of crystal orientation, is the usual way to overcome this problem [Ssuw14].



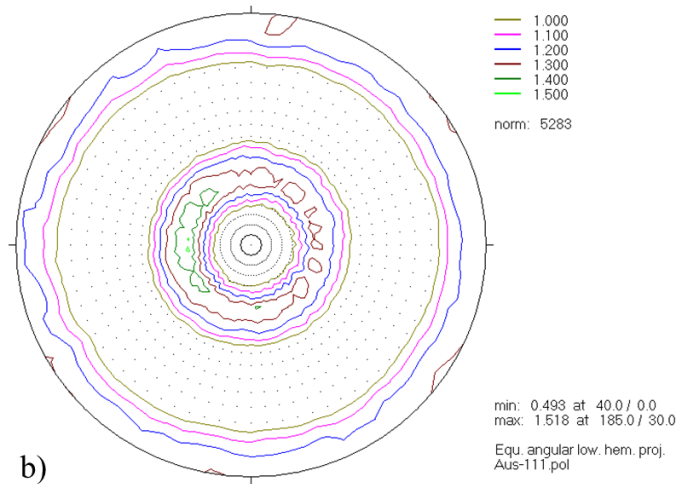


Figure 3.8 a) Pole figure of austenite (111) reflection in ADI without plastic deformation. (The crystallite orientation is almost random; the maximum of *m.r.d.* in the Pole figure is 1.145)
 b) Pole figure of austenite (111) reflection in ADI with 40% plastic strain. (The austenite crystallites have shown preferred orientation on the (111) planes; the maximum of *m.r.d.* in the Pole figure is 1.518)

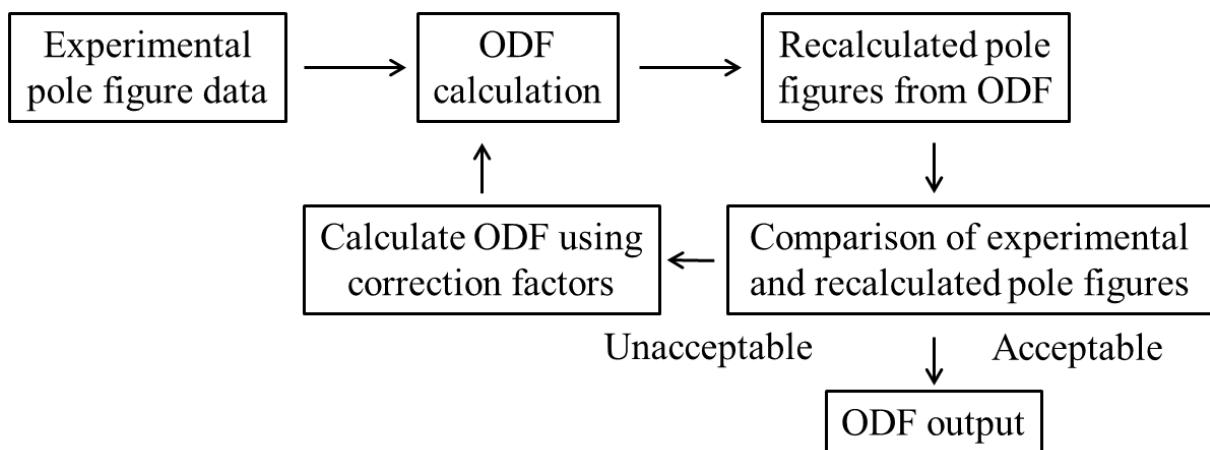


Figure 3.9 Schematic calculation of ODF (orientation distribution function) from pole figures [Ssuw14].

Figure 3.9 shows the calculation procedure for an ODF from the measured pole figure data. Normally, two pole figures (from two Bragg reflections) of a phase which are not parallel to each other in 3-D space are required to be used for quantitative ODF calculation. For high symmetric crystal system (for example: *bcc*) it is also possible to use just one pole figure for quantitative 3-D texture analysis (ODF calculation). Through calculation with several mathematical functions (Bunge notation [Hbun87]) the measured numerical pole figure data will transform into the ODF which includes all the crystal orientations in the specimen. In general, the calculation of ODF requires the measurement of two different pole figures. But for a high symmetrical crystal structure, it is sufficient to calculate the complete ODF by

measuring one pole figure. Bunge [Hjbu65], Roe [Rjro65] and Williams [Will68-01, 02] have proposed this procedure independently and have derived the important texture components of cubic crystals as shown in Figure 3.10. The calculation can be achieved using several freely available software packages like Pfplot, MTEX, LaboSoft and etc. More details about the derivation of the mathematical functions and the coordinate system rotations of the ODF are shown in [Ssuw14].

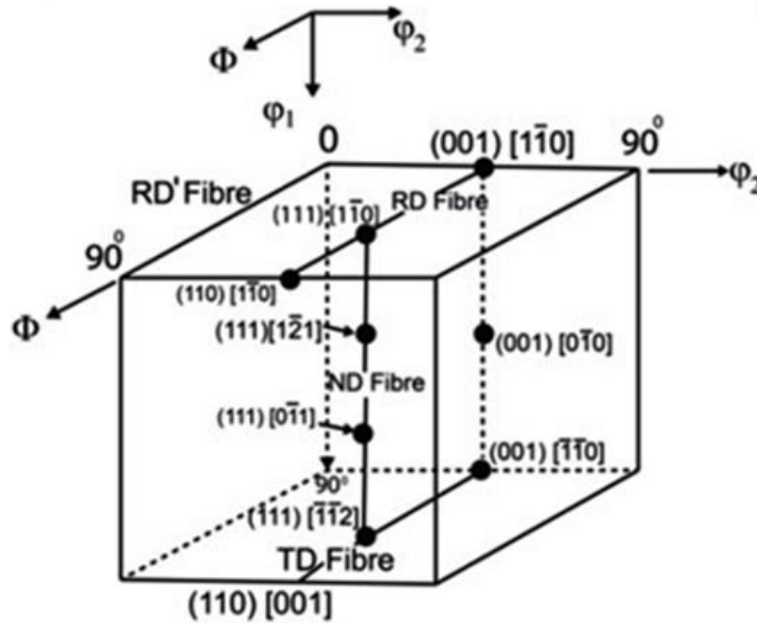


Figure 3.10 3D Euler space with important texture components [Ssuw14]. All the texture components can be shown in this 3D Euler space in the form of $(hkl) [uvw]$. The main texture components of *fcc* and *bcc* metals are located in the plane view of the $\phi_2=45^\circ$ section and shown again separately in Figure 3.12.

3.2.2 Determination of texture with diffraction measurements

The determination of texture can be achieved through X-ray diffraction [Jmar99], synchrotron diffraction [Hrwe03], electron diffraction with TEM [Jmos90, Jinw95] and neutron diffraction [Hjbu82]. Each method has its own characteristics and the choice of the measurement technique for an actual sample needs be undertaken with this in mind.

Figure 3.11 represents a pole figure measurement with two variable angles for tilting ($\chi = 0^\circ \sim 180^\circ$) and rotation ($\phi = 0^\circ \sim 360^\circ$). In addition, the corresponding sample coordinate system is also defined. Using a two dimensional area detector several points in a pole figure can be measured simultaneously. After tilting and rotation of the sample around χ and ϕ the intensity of selected reflections can be obtained and such the corresponding whole pole figures will be derived. For detailed information about specific equipment and methods the reader is referred

to standard references like [Hjbu65, Rjro65 and Ssuw14]. Here only a simple comparison on the choice of different methods is introduced.

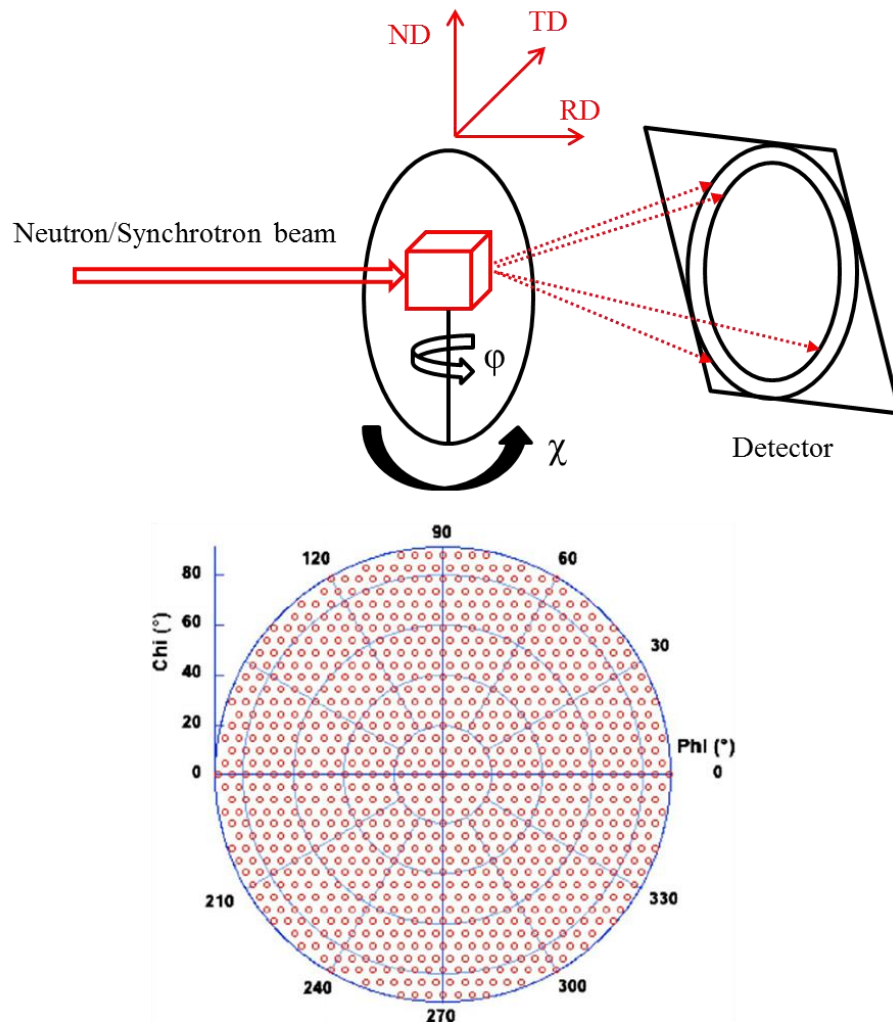


Figure 3.11 Top: Schematic overview of diffraction geometry in pole figure measurements. Bottom: Resulting pole figure $5^\circ \times 5^\circ$ grid (as expressed in the measurement angles χ (chi) and ϕ (phi)).

As the penetration capability of laboratory X-ray sources is quite limited for metals and ceramics and their wave length range restricted, it is mainly being used for texture investigations on the surface of fine grained materials. However, as it is a laboratory based source it is easily accessible and until now the cheapest method. Synchrotron radiation on the other hand has much higher penetration capabilities, but due to its limited beam size and divergence, it is usually used for fine grained materials only. Electron diffraction with TEM enables to visualize the texture distribution within the grains [Jmos90, Jinw95], making it possible to analysis the interaction of neighboring grains for instance during plastic deformation processes. EBSD is more suitable for coarse-grained materials and yields in principle only 2-D information. Finally neutron diffraction is suitable for bulk specimen

almost without limitation in grain size ranging from nm up to mm. It is also possible to determine magnetic pole figures using neutron diffraction. Due to its relatively good angular resolution and the possibility to use a large wavelength range even measurements on materials having densely packed diffraction peaks are possible.

3.2.3 Textures in *bcc* and *fcc* metals

In ADI the ausferrite matrix contains mainly *bcc* ferrite and retained *fcc* austenite from which the ferrite phase originates during the austempering process. It has been shown for many types of steels [Yohm01], [Hkdh90], [Yohm96], [Moka90] that a certain orientation relationship between the parent and product phases exists during and after the transformation [Ufko98]. This depends on those close-packed planes and directions, with which the respective phase boundaries will have the lowest surface energy. The *fcc* austenite (A) and *bcc* ferrite (F) in ‘ausferrite’ have been found to have the Kurdjumov-Sach (KS) or Nishiyama-Wassermann (NW) orientation relationship [Vaya14, Fbar10].

$$\text{Kurdjumov-Sach:} \quad \{111\}_A \parallel \{011\}_F, \langle 1\bar{1}0 \rangle_A \parallel \langle 1\bar{1}1 \rangle_F$$

$$\text{Nishiyama-Wassermann:} \quad \{111\}_A \parallel \{011\}_F, \langle \bar{2}11 \rangle_A \parallel \langle 0\bar{1}1 \rangle_F$$

For example, in Kurdjumov-Sach (KS) relationship, the $\{111\}$ planes of austenite is parallel to the $\{110\}$ planes of ferrite; correspondingly, $\langle 1\bar{1}0 \rangle_A$ directions is parallel to the $\langle 1\bar{1}1 \rangle_F$ directions. This scheme is also valid in strain induced martensitic transformation and the martensite, which transformed from retained austenite, also has the KS and NW orientation relationship with the originating austenite [Vaya14, Fbar10].

The texture development in metals depends in principle solely on the crystal structure. Nevertheless many studies and articles on texture formation in metals have shown that many other variables like microstructure, alloying elements, deformation mode or temperature can influence the texture development severely thus making the prediction of texture formation in metals due to plastic deformation quite complex in practice. In the following we will present a summary of experimental results for textures in materials containing *fcc* and *bcc* phases.

The most common slip system in *fcc* metals is slip along the $\{111\}$ close-packed plane in $\langle \bar{1}10 \rangle$ direction. In *bcc* metals, slip occurs along the planes of type $\{110\}$, $\{123\}$ and $\{112\}$ in the direction of $\langle 111 \rangle$, for which their Burgers vectors are the shortest and have the lowest activation energy [Ufko98]. Most of these components are present in the $\varphi_2=45^\circ$ section of the ODF (Fig. 3.12) and is therefore commonly used to describe the texture distribution in *fcc* and *bcc* metals.

compression of *fcc* metals should be the same and vice versa [Ufko98]. The texture development caused by rolling is always more complicated as the ones caused by uniaxial deformation. However over years a multitude of investigation on the texture development in ferritic steels yielded a comprehensive description on texture orientations of rolled *bcc* as functions of temperature, deformation levels and alloying elements [Drab94, Msud81, Rkra93]. A summary of main *bcc* and *fcc* texture components is listed in table 3.2.

3.3 Martensitic transformation in ADI

Due to its high occurrence frequency in different materials and its close relationship with material mechanical properties, martensitic transformations were always an important subject of investigations in the material research since they were first found in steels by Adolf Martens in 1890 [Csm92]. Martensitic transformation is defined as diffusionless transformation with short-ranged atom displacement. Over thousand papers have been published until now with subjects ranging from crystallography changes to thermodynamics and kinetics. Its definition is nowadays not only limited to the transformation from *fcc* austenite to *bct* martensite in steels, it has also been observed in many other elements like Ti (*bcc* \leftrightarrow *hcp*), alloys like Cu-Sn (*bcc* \leftrightarrow *fcc*), chemical compounds and ceramic materials [Erpe70]. Here only a brief overview on the current knowledge of martensitic transformation in ADI will be given.

As shown in chapter 1.2 ADI consists of acicular ferrite and highly carbon enriched retained austenite. The carbon enriched austenite is metastable and several reports exist indicating a partial transformation to martensite when ADI is subjected to deformation [Hnha04, Dmys14, Wböh15]. Formation of martensite in ADI was first observed on the fractured surface of tensile specimens and the surface of cold rolled specimens using X-ray diffraction and microscopy [Jara97], while Rietveld refinement of X-ray diffraction data allowed following the quantitative evolution of martensite with plastic deformation up to 25% [Jlga03]. The effect is well known in steels as transformation induced plasticity (TRIP) and has been used since the early 70's to enhance mechanical properties [Sdan70]. A prerequisite for this martensitic transformation is the existence of metastable retained austenite. The martensitic transformation is directly linked to the stability of the retained austenite, which contains several influence parameters for the martensitic transformation like austenite grain size, alloying element contents in austenite and stress state of austenite. It can be approximately scaled by the M_s temperature [Ccap03, Ksug92]. Martensite will start to form when the Gibbs free energy of austenite gets larger than the Gibbs free energy of martensite plus a critical driving force for martensitic transformation (ΔG_{crit}). Either thermal martensite induced by cooling or strain induced martensite is formed [Mmaa10].

In general one distinguishes the martensitic transformation according to external conditions, as athermal / isothermal martensite or stress / strain induced martensite.

3.3.1 Temperature induced: Athermal and isothermal martensite

Upon cooling martensite begins to form at a specific temperature M_s . As the cooling temperature falls below M_s , a certain amount of martensite appears rapidly. Simultaneously, the transformation induced strain energy increase in the system stabilizes the retained austenite. Therefore undercooling of the stabilized austenite is necessary in order to increase the driving force for further transformation. The total volume fraction of martensite increases with decreasing temperature and the transformation is completed at the martensite finish temperature M_f (see as an example the martensitic transition in a NiTi shape memory alloy, Figure 3.13). In some cases, even if the temperature dropped close to 0K, austenite will not fully transform to martensite ($M_f < 0K$). The difference between athermal and isothermal martensite is only their transformation time dependence, which is related to the nucleation controlled kinetic, and will be briefly introduced as follows:

Athermal martensite transformation is time independent as nearly all of the martensite is generated immediately when the target cooling temperature M_t ($M_s < M_t < M_f$) is reached, with only a small amount formed during the isothermal holding [Znis78] (Fig. 3.14 a).

On the other hand in some alloys the martensitic transformation has clear time dependence as the formation of martensite occurs mainly during the isothermal holding (Fig. 3.14 b).

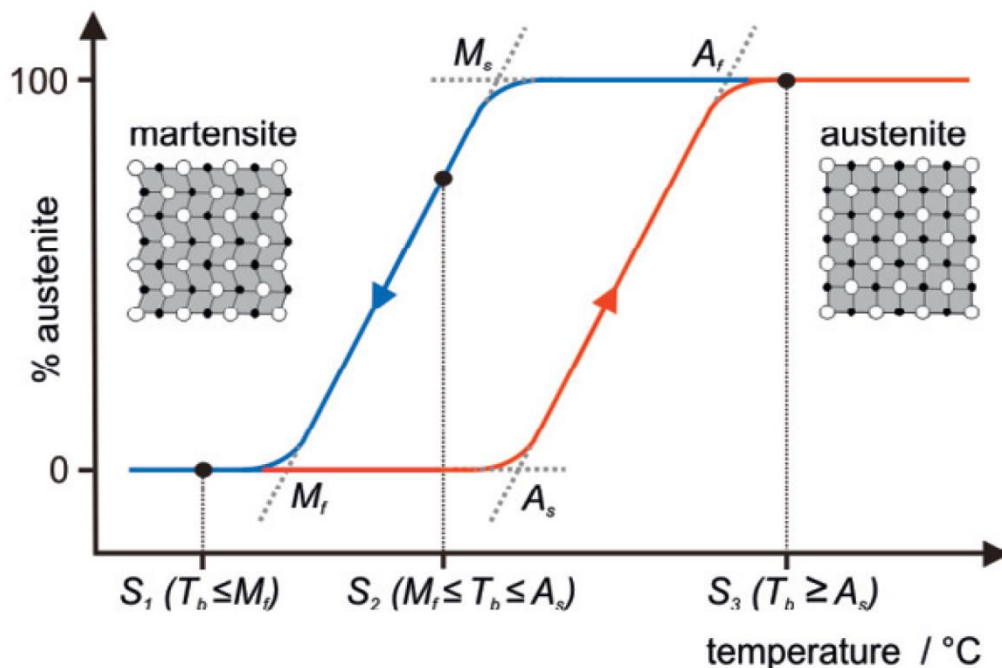


Figure 3.13 Schematic illustration of the phase transformation and the hysteresis of NiTi-SMAs [Rpfe13].

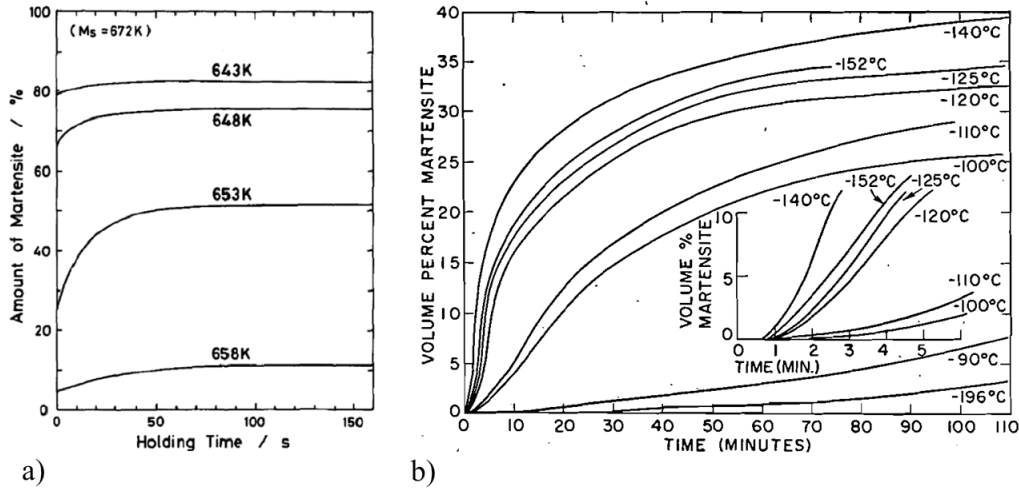


Figure 3.14 a) Athermal martensite of Fe-15%Ni alloy at different cooling temperature during isothermal holding [Mvil14]. b) Isothermal transformation results of Fe - 23.2 wt% Ni - 3.62 wt% Mn showing temperature dependence and incubation time [Chsh55].

In the athermal martensitic transformation, also named “*Umklapp*” transformation, the nucleation is based on the fast kinetics of internal twinning. The rapid transformation rate of this also explains the independence between M_s and cooling rate. The morphology of the resulting martensite is plate shaped and can be characterized by a twinned substructure [Mvil14].

In isothermal martensitic transformation, named “*Schiebung*” transformation, on the other hand the nucleation is mainly based on the movement of interfacial dislocations either at the beginning of isothermal holding (Fig. 3.14 b) or during the holding of (Fig. 3.14 a),. Here the morphology of martensite is lath shaped. In the final part of isothermal holding (Fig. 3.14 b) the slow increase of the martensite volume fraction is associated with thermo-elastic growth [Mvil14] or auto catalytically produced martensite nuclei [Srpa67].

According to [Hkdh82, Smcv09, Dpko59], there is an exponential relationship between the volume fraction of athermal martensite and temperature in the range between M_f to M_s which can be expressed using the Koistinen-Marburger equation (3.1) [Dpko59]. In the original publication the material dependent parameter b in equation (3.1) is assumed to be constant, which is suitable for carbon steels.

$$\frac{f_M}{f_A} = 1 - \exp[b(T - M_s)], b = 1.1 \times 10^{-2} \quad (3.1)$$

f_M : volume fraction of martensite

f_A : volume fraction of austenite

T : quenching temperature

b : parameter related to M_s and M_f [Hyyu97, Fhuy15]

Later Magee [Clma70] has developed this equation using martensite nucleation theory and delineated the relationship of parameter b to the driving force of nucleation ($\Delta G^{\gamma \rightarrow M}$, equation (3.2)). Here the influence of chemical composition is already included in the phase specific free energy part of the equation developed by Magee [Yywe14]. This equation is more accurate than K-M equation and both of them are used to calculate the volume fraction of martensite in middle or high carbon steel. In these steels the M_s temperature is low enough, so that the carbon partitioning effect during the martensitic transformation can be ignored [Yywe14]. However, the parameters V and \emptyset are very difficult to determine experimentally which prevented a wider application of equation (3.2) to determine b . In most cases, the K-M equation is therefore still the preferred choice for the calculation of the relationship between martensite phase fraction and temperature.

$$b = V \times \emptyset \times \partial(\Delta G^{\gamma \rightarrow M})/\partial T \quad (3.2)$$

V : size of martensite plate

\emptyset : coefficient related to material

No unified theory describing the isothermal martensitic transformation has been established until now. Hence to describe isothermal martensitic transformation kinetics empirical equations have also been used [Esma52, Srpa67 and Ppri08]. However, the scope of application of these empirical equations is not as wide as the K-M equation for athermal martensitic transformation. This is because the main factors dominating the isothermal martensitic transformation change due to variations in the chemical composition of the material. For instance in Fe - 23.2 wt% Ni - 2.8 wt% Mn steel [Ppri08], the isothermal martensite nucleation rate was determined to be dominated by the grain size of the parent austenite. The driving force for continuation of the transformation in an austenite grain stems from the increased strain of the formerly transformed austenite region. The nature of the isothermal martensitic transformation in such Fe-Ni-Mn alloys can be explained by classical

homogenous nucleation theory² [Srpa67]. On the other hand in Fe - 30 wt%Ni alloy, the isothermal martensitic transformations kinetic has been explained using reaction path theory² [Esma52]. Isothermal martensitic transformations have not been found in ADI materials. Therefore, further formulation and discussion of isothermal martensitic transformations kinetic will not be given in this work.

3.3.2 Stress and strain induced martensite

Stress-assisted as well as strain-induced martensite formation occurs between an upper temperature limit M_d and M_s . As in case of the formation of athermal martensite, at M_s the difference of free energy between austenite and martensite is the same as the driving force of martensitic transformation and no external energy is needed to initiate the transformation. At a certain temperature T above M_s , the difference of Gibbs free energy between martensite and austenite becomes smaller than the driving force of martensitic transformation (Fig. 3.16). To initiate the martensitic transformation, the gap between the Gibbs free energy difference of austenite and martensite ($\Delta G^{\gamma \leftrightarrow M}(T)$) and the driving force of martensite transformation ($\Delta G^{\gamma \rightarrow M}$) needs to be overcome by increasing internal strain energy of austenite using external stress. The external stress will destabilize the austenite phase and increase M_s . A linear relationship between external stress and M_s has been determined in Fe-Ni-C and Fe-Ni-Cr-C alloys by Bolling and Richman [Gfbo69, 70-1, 70-2, Rhri71] (Fig. 3.15). By increasing the loading temperature T , the gap between $\Delta G^{\gamma \leftrightarrow M}(T)$ and $\Delta G^{\gamma \rightarrow M}$ becomes larger, so that higher stresses are needed to initiate martensitic transformation (Fig. 3.16). Therefore, after reaching the maximal yield strength σ_y at M_s^σ , strain-induced martensitic nucleation which needs lower stress will dominate the continuation of transformation for higher loading temperatures [Gbol72]. At higher temperatures e.g. $T > M_s^\sigma$, the stress needed to initiate stress-assisted martensite formation has to be larger than the yield strength at that temperature which cannot be achieved in practice.

² Difference between classical homogenous nucleation theory and reaction path theory see [Gbol06,Tjza52]

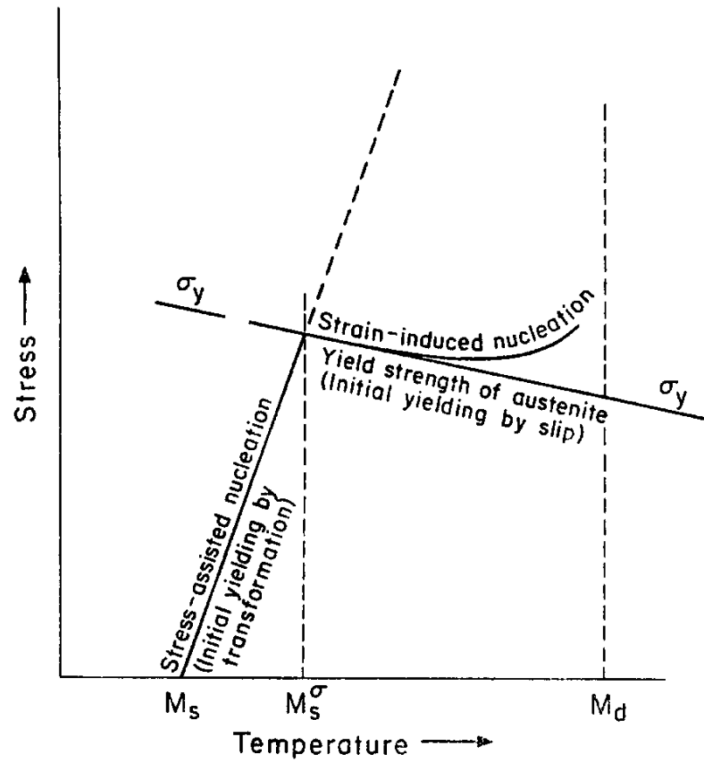


Figure 3.15 Temperature range of stress-assisted (below M_s^σ) and strain-induced martensitic (above M_s^σ) transformation [Gbol72].

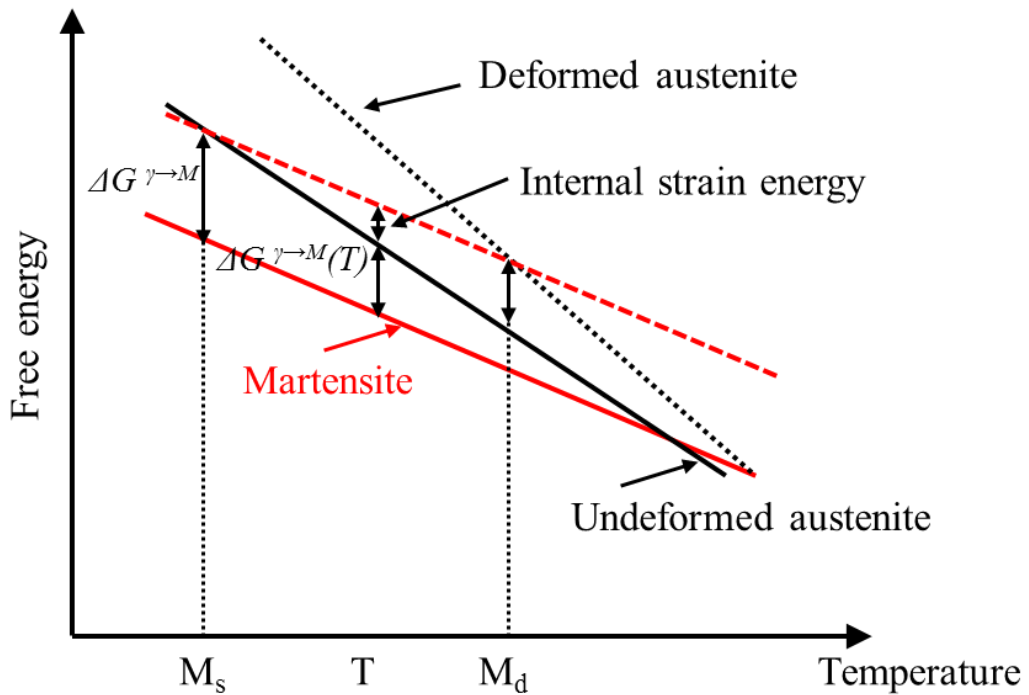


Figure 3.16 The free energy diagram of strain induced martensitic transformation (according to [Hesh01]).

Strain-induced martensitic formation was first explained by Olson and Cohen using an intersection-shear mechanism [Gbol72]. The formation of martensite nucleation embryos is generated by two $\{111\}\langle 112\rangle$ intersecting shear systems [Gbol72]. One is called T/3 shear with a displacement in the order of $\frac{a_{fcc}}{18}\langle 112\rangle$ and the other called T/2 shear with a displacement of $\frac{a_{fcc}}{12}\langle 112\rangle$ on the $\{111\}$ slip plane [Lbra07]. During plastic deformation more and more $\{111\}\langle 112\rangle$ slip systems will be activated. Such activation results in creation of new martensite embryos. Different to stress-assisted martensitic transformation, where its evolution depends on the same nucleation embryos, the strain-induced martensitic transformation is sustained by the formation of new martensite nuclei [Gbol72]. Since the strain-induced martensitic transformation is directly related to slip, the factors that influence the slip formation directly control the martensitic transformations kinetic.

3.4 Models for strain induced martensitic transformation

Models developed to describe the strain induced martensitic transformations kinetic explain the relationship between the martensite volume fraction f_M and plastic strain ε . The mathematical formulas in these models should contain all or at least the most important influence factors like temperature, grain size, chemical compositions etc. In the past few decades after strain induced martensitic transformation was found, the relationship between these factors and the martensitic transformation rate has already been identified in many works [Jchi11, Ksug92, Gnha96, Rece56, Jtal05 and Hnha04].

3.4.1 Influence factors for strain induced martensitic transformation

The influence factors that have significant impact on strain induced martensitic transformation have been identified in literature (s. above) as shape, location, and size of the austenite grains as well as chemical composition of austenite, plastic deformation mode, strain rate and loading temperature. Before establishing a mathematical model, the relationships between each factor and the martensite phase fraction will be reviewed:

Microstructure (Shape and location of austenite grain)

In TRIP steels the stabilization of retained austenite is achieved by special heat treatments and addition of different alloying elements [Jchi11, Ksug92]. The work hardening behavior (Fig. 3.17 left) as well as the martensitic transformation rate (Fig. 3.17 right) of TRIP steels of two different austenite microstructures resulting from different heat treatments (lamellar and equiaxed), were observed to be significantly different. Compared to the TRIP steel with equiaxed microstructure, the TRIP steel with lamellar microstructure has higher work hardening exponent n value (Fig. 3.17, $n > 0.2$, formation of martensite) at higher strains which corresponds to a slower transformation rate, and consequently, higher stability of retained austenite. The results indicate that the grain form plays an important role in the austenite stability. Furthermore it could be shown that the location/surrounding of the austenite grains is of similar importance. Lamellar austenite grains are surrounded by harder bainite, whereas the equiaxed austenite grains are surrounded by ferrite. The harder bainite is able to bear more stress and strain as the ferrite thereby enhancing the austenite stability [Jchi11].

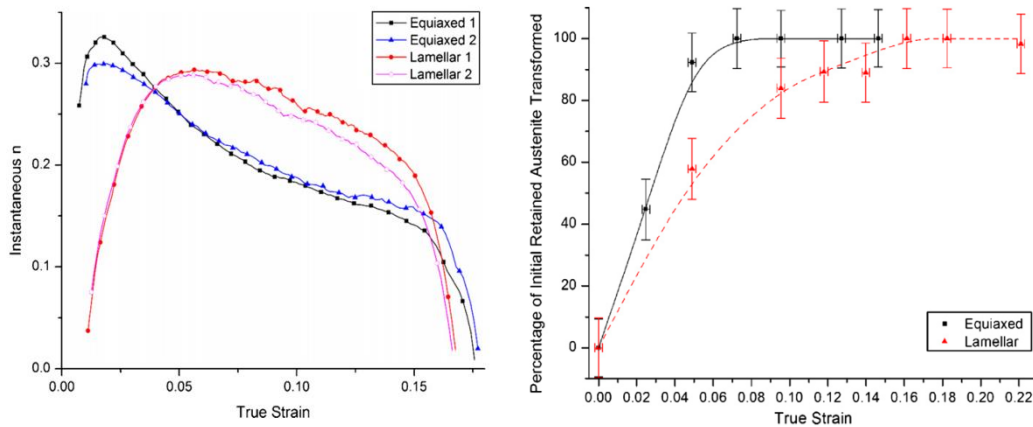


Figure 3.17 The instantaneous n (left) and transformed percentage of initial retained austenite as a function of true strain (right) for equiaxed and lamellar microstructures of TRIP steel with a bainite hold of 100s at 450°C [Jchi11].

Microstructure (austenite grain size)

The effect of grain size on the strain induced martensitic transformation has been investigated for many different steel alloys like Fe-C-Mn-Si TRIP steel [Gnha96], Fe - 30wt% Ni alloy [Rece56], Fe - 31 wt% Ni - 0.28 wt% C steel [Mume75] to name a few. Finer austenite grains increase the austenite stability by reducing the probability of forming martensite nucleation sites. This is clearly reflected in the decrease of M_s temperature with reducing grain size (Fig. 3.18).

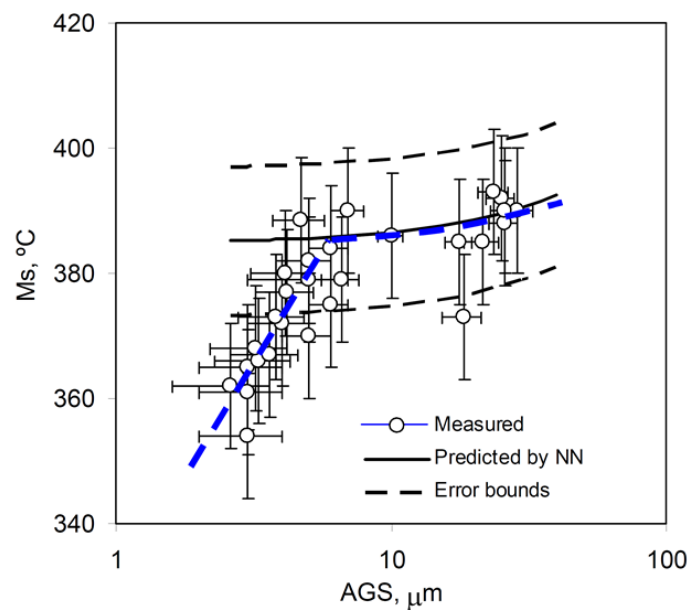


Figure 3.18 Measured M_s and as a function of austenite grain size (AGS) [Agar15].

However, the correlation between M_s temperature and the austenite grain size is different for different grain size ranges. The finer the grain size, the higher the correlation between M_s temperature and grain size will be. Once the grain size reaches a certain value, for example in case of Fe - 31 wt% Ni - 0.28 wt% C steel this is around 150 μm , the M_s is seemingly not affected by further grain size changes any more. The reason behind the change in slope of the M_s vs. grain size plot has not been understood sufficiently until now and is still a matter of debate.

Chemical composition

Alloying elements in austenite decrease the M_s by increasing the chemical driving force for the martensite transformation. According to their crystallographic location, the alloying elements can be divided into two types. Nonmetallic alloying elements with small atomic radii like C, N, O are located in octahedral interstitial sites of the austenite, while metals like Ni, Cr, Mn, Cu substitute Fe in its original site positions. Either of them lead to distortion in the austenite lattice and decrease of the free Gibbs energy of austenite and therefore stabilize the austenite lattice. In numerous studies on the effects of alloying elements on the martensite start temperature M_s it has been shown that among all elements, carbon is by far the strongest austenite stabilizer per weight percentage (wt%) (see Figure 3.19 and [Esro46, Wste56, Kwan65, Asto12, Ragr46, Ccap03, Smcv12]).

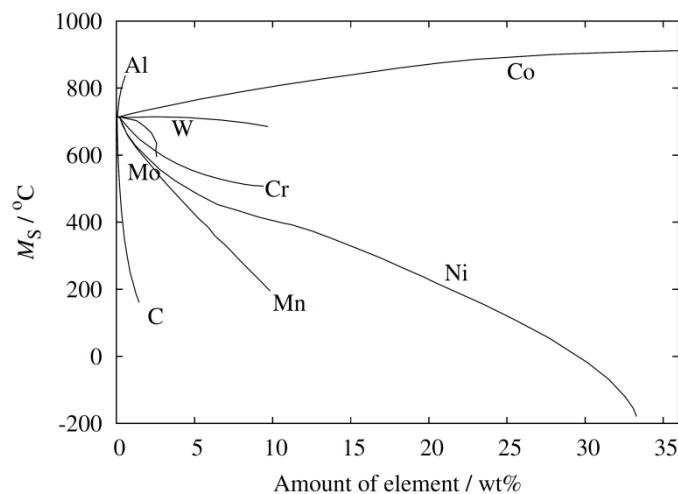


Figure 3.19 M_s temperature of Fe-X binary system [Mizu70]

However, the carbon content in steels needs to be limited to retain good ductility and corrosion resistance properties. Thus stabilization of retained austenite in steels is achieved mainly using large amounts of additional and expensive alloying elements like Ni, Cr or Mn.

On the other hand the carbon content in ADI is high (~3.6 wt%) and stabilization of retained austenite can be achieved through the heat treatment alone without or with only a small amount of additional alloying elements.

Deformation mode

The effect of deformation mode on the martensitic transformation has been studied for instance in 304 stainless steel (Fig. 3.20). The morphology of martensite formation is different with different deformation modes [Tiwa98]. The influence of this factor on the martensitic transformation is also temperature dependent. At lower deformation temperature, the martensitic transformation rate is less affected by the deformation mode. The higher the temperature is, the greater the difference in martensitic transformation rate with different deformation modes.

However, the effect of deformation mode on martensitic transformation is not widely studied in different materials. This lack of sufficient data makes this factor difficult to be expressed and quantified in mathematical models.

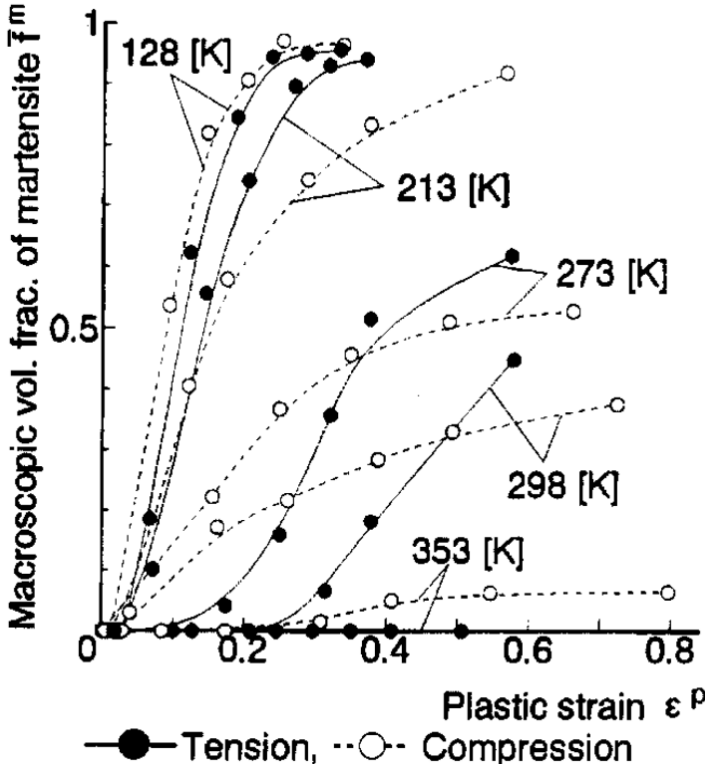


Figure 3.20 Plot of martensite phase fraction and plastic strain in 304 austenitic stainless steel [Tiwa98].

Strain rate $\dot{\epsilon}$ and loading temperature T

The effect of strain rate on the martensitic transformation was found being mainly related to adiabatic heating of the deformed material caused by high strain rates [Jtal05, Hnha04]. The adiabatic heating result from the phase transformation and the plastic deformation, and it decreases the chemical driving force of martensitic transformation. Since the strain rate causes changes in the sample temperature, it can be combined with loading temperature into one parameter in corresponding models (Fig. 3.21).

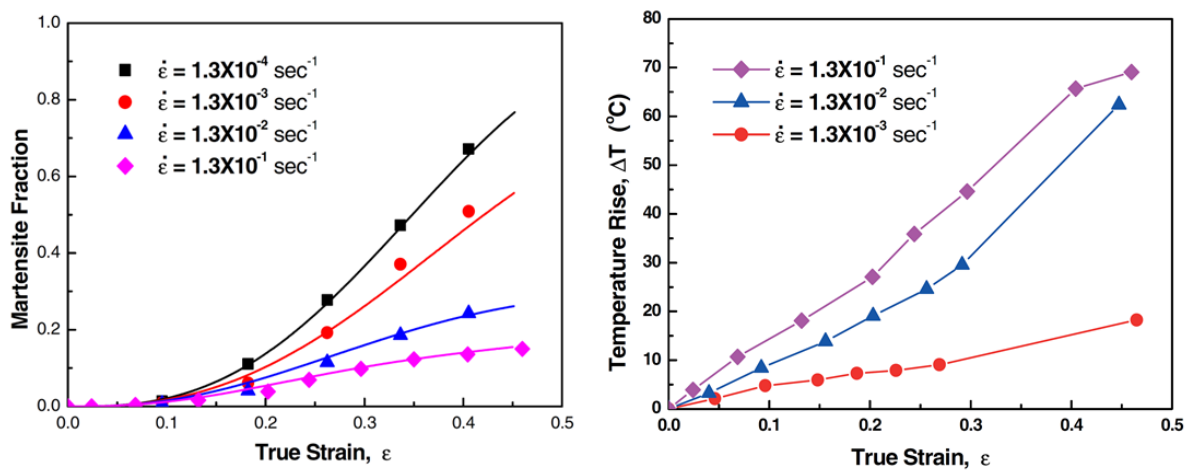


Figure 3.21 Martensite volume fraction in 204M stainless steel during tension for various strain rates (left). Sample temperature rise during tension for various strain rates (right) [Hnha04].

In the last few decades several models were developed to describe strain induced martensitic transformation kinetics in TRIP and other austenitic steels. Widely accepted models were developed by Olsen-Cohen [Gbol75], Stringfellow [Rgst92] and Burke-Matsumura-Tsuchida (BMT-model) [Jbur65, Omat87, Ntsu00].

3.4.2 Nucleation model

Olson and Cohen [Gbol75] regarded shear-band intersections as the primary nucleation sites for the strain induced martensite formation. This model yields a sigmoidal curve saturating before complete transformation and adequately describes the kinetics of the phase transformation in austenitic steels with just two temperature dependent parameters. The first parameter α accounts for the formation of the shear-band intersections as a function of strain and is dependent on stacking-fault energy. The second parameter β relates the probability of a shear-band intersection to form a martensitic nucleation site with chemical driving force of martensite formation.

It used a simplistic formula to represent a complex problem, which will inevitably produce some errors. For instance when different materials show a different transformation behavior at the same loading temperature this formulation cannot fully explain the transformation behavior. Stringfellow and co-workers therefore tried to advance this model realizing that the cause for strain induced martensitic transformation not only depends on plastic strain and temperature, but also on the stress state of austenite, austenite grain size and alloying compositions [Rgst92, Jbur65, Omat87, Ntsu00].

$$f_M/f_A = 1 - \exp\{-\beta[1 - \exp(-\alpha\varepsilon)]^n\} \quad \text{Olsen-Cohen model} \quad (3.3)$$

f_M : volume fraction of martensite

f_A : volume fraction of initial austenite

α : parameter dependent on stacking-fault energy

β : parameter related to chemical driving force

n : exponent dependent on material

3.4.3 Relaxation of internal strain energy model

Shin *et al* [Hcsh01] have proposed a model where the martensitic transformation is considered as a continuous relaxation process of internal strain energy accumulated during plastic deformation. The transformation is realized as a successive two stage processes with formation of nucleation sites at locations of high internal strain energy like shear-band intersections and grain boundaries and ensuing martensitic transformation at these sites described above by Olson and Cohen. The model relates directly the austenite stability to the strain induced martensite transformation rate, also taking into account the corresponding deformation mode.

$$f_M/f_s = 1 - \exp\{-\beta(\varepsilon - \varepsilon_0)^n\} \quad (3.4)$$

f_M : volume fraction of martensite

f_s : saturation value of martensite volume fraction

β : stability of austenite

ε : plastic strain

ε_0 : critical inelastic strain where martensitic nucleation starts

n : deformation mode parameter

The parameters α , which describes the dependence on stacking-fault energy, and β , which describes the relationship on the chemical driving force, in Olson's and Cohen's model

(equation (3.3)) have been converted into parameter β (austenite stability) in this new model (equation (3.4)). A series of previous studies have shown (section 3.4.1) [Jchi11, Ksug92, Gnha96, Rece56, Jtal05 and Hnha04], that the relationship between plastic strain and martensite phase fraction is been affected by various factors, such as chemical composition of austenite, grain size, grain shape, loading temperature, strain rate etc. The changes in these factors ultimately affect the stability of austenite. Thus the new model integrates all the influencing factors onto austenite, using the austenite stability to characterize the most important influence factors which is the greatest advancement of the new model. However, the austenite stability in the new model is only expressed as a numerical value and is not clearly defined. Hence it will be studied and discussed further in this work.

4. Experimental Procedures

4.1 ADI sample preparation

The base material cast ductile iron was produced by Bosch Rexroth AG with the dimension of 140 mm × 110 mm × 20 mm plates. Its chemical composition is listed in table 1 (see also [Psaa16]). Three different alloying compositions were cast varying only in the nickel content (Table 4.1). These three types of cast ductile iron were then machined to standard threaded cylindrical tensile samples for tension experiments, cylindrical shaped samples for compression and low temperature experiments and strip-shaped samples for cold rolling tests. The process parameters for the different ADI heat treatments [Lmei13, Psaa16] carried out on samples are listed in table 4.2. While the samples for tension and cold rolling were heat treated in a salt bath, the samples for compression and low temperature experiments were heat treated in a mirror furnace with inert Ar gas atmosphere [Lmei13, Psaa16].

Table 4.1 Chemical composition of the starting cast ductile iron material used for the heat treatments.

Elementary chemical compositions in wt%	C	Si	Mn	Ni	Cu, Mo, P, S	Fe
	3.6~3.7	2.3	0.2	0 0.5 1.5	less than 0.08	balance

4.2 Optical microscopy

The ADI samples with the heat treatment and deformation parameters as listed in table 4.2 and section 4.4 were embedded in thermosetting embedding agents using an ATM OPAL 410 heat embedding machine. After stepwise grinding and polishing of different levels, the ADI samples were etched by a color etching method [Fhai08] using LePera solution (1 wt% Na₂S₂O₅ in aqueous dilution and 4 vol% picric acid in ethanol) for 10 to 30 s. The phases with different colors were characterized using a Leica DM 600 microscope and are shown in section 5.1.

Table 4.2 Heat treatment conditions of ADI before plastic deformation. The second column indicates the austenitisation temperature the sample sets were subjected to (marked by “x”), the third column shows the corresponding austempering temperatures and the last column indicates the Ni content.

ADI samples	Austenitization T_γ [K]		Austempering T_{Aus} [K]			Ni content		
	1173	1223	573	623	673	0wt%	0.5wt%	1.5wt%
Tensile samples	×	×	×	×	×	×		
Compression samples	×		×	×	×	×	×	×
Cold rolling samples	×		×			×	×	×

4.3 SEM and TEM

The same samples prepared for optical microscopy were also used for investigation with high resolution SEM using a Zeiss NVision 40 focused-ion-beam-system (FIB).

For TEM experiments three further ADI samples austenitized at 900°C and austempered at 350°C (unstrained, 42% strained and quenched to 77 K) were mechanical polished to 100 μm and cut into a round sheet with a diameter of 2 mm. Finally, the center of the samples was electro-polished in GATAN691 machine at 4.5 Volt at 6° to 100 nm thickness. A JEM2100 transmission electron microscope was conducted at room temperature to determine the true morphology of “ausferrite”. The morphology and orientation relationship of the phases in ADI were confirmed in bright/dark field of TEM images by the calculation of the spots in selected area diffraction pattern (SADP).

4.4 Tensile, compression and cold rolling experiment

The samples for neutron diffraction experiments after plastic deformation were prepared as follows:

Tensile deformation:

The six groups ($2T_\gamma \times 3T_{Aus} \times 1$ Ni content, table 2) of cylindrical tensile ADI samples (dimension: gauge length = 30 mm, diameter = 6 mm, M10 threads) were deformed in a stepwise manner using a test rig [Mhoe13] from 0% strain level to fracture with a 0.5% increment in strain. The strain was measured using a clip on strain gauge (Instron type 2620-602). Typical stress-strain curves of tensile ADI samples ($T_\gamma = 900^\circ\text{C}$, $T_{Aus} = 300, 350$ and 400°C) are shown exemplarily in Figure 1a. In the case of tensile deformation, in-situ neutron

diffraction measurements were performed on these samples to determine the phase fractions. The plastic strain of tensile samples was calculated according to the corresponding stress-strain curves (Fig. 1b). In contrast, pre-deformed samples were used for the texture measurements.

Compression deformation:

The nine groups ($1T_\gamma \times 3T_{Aus} \times 3$ Ni contents, table 2) of cylindrical ADI samples (dimension: length = 10 mm, diameter = 6 mm) were prepared for the compression tests. The length/diameter dimensions of the samples were chosen according to the ASTM and the German DIN standard 5100 such as to avoid buckling. Sample surfaces were carefully machined to be parallel and lubricated to minimize barrelling in accordance with the ASTM standard E9-89a for compression testing. The samples were then deformed ex-situ using the test rig [Mhoe13] at a strain rate of $3.7\sim 4 \times 10^{-4} \text{ s}^{-1}$ from 0% to 45% strain level with 5% or 10% increment in strain. Due to the small dimensions no strain gauge could be attached to the sample. Therefore the strain during deformation was determined by the crosshead position of the tensile rig taking into account the elastic deformation of the rig. Finally the true strain of the samples was checked and calculated by measuring the change in length of the samples after each compression using a high precision calliper.

Cold rolling:

The three groups ($1T_\gamma \times 1T_{Aus} \times 3$ Ni contents, table 2) of long strip-shaped ADI samples (dimension: length 100 mm, thickness 4 mm, width 6mm) were cold rolled with a laboratory rolling device. The cold rolling was performed at a strain rate of about $3 \times 10^{-3} \text{ s}^{-1}$ according to the calculation of thickness change and the average cold rolling time. The samples were deformed ex-situ from 0% to 50% strain level with 10% increment in strain.

4.5 In-situ synchrotron diffraction of ADI during heat treatment

The in-situ synchrotron diffraction measurements were performed at beamline P07 PETRA III/DESY [Norb14]. The purpose of the measurements is to indicate the carbon diffusion in ferrite grains during the austempering. A Bähr DIL805 quenching dilatometer with induction heating was used for the in-situ ADI heat treatment during the synchrotron measurements to ensure high quenching rates as well as excellent temperature stability (Fig. 4.1). For this the respective cylindrical ADI sample (0 wt% Ni content, dimension: length 10 mm, diameter 4 mm) with a thermocouple welded on its surface (ensure the accuracy of the sample temperature change as shown in Figure 4.1) was placed in the center of heating collar, fixed

by the two deformation poles of the dilatometer. The experiment conditions and parameters are shown in table 4.3.

Table 4.3 Austempering conditions of ADI samples prepared for synchrotron diffraction measurements and synchrotron measurement time resolution. All the ADI samples were austenitized at 900°C for 30 min. The wave length of synchrotron beam is 0.14235 Å and the sample-detector distance is 1558.6 mm.

ADI (0 wt% Ni)	Austempering T_{Aus}	Time [min]	Time in fast mode with time resolution 2s [min]
	[°C]		
	450	30	5
	400	40	10
	350	60	20
	300	90	30
	250	120	45

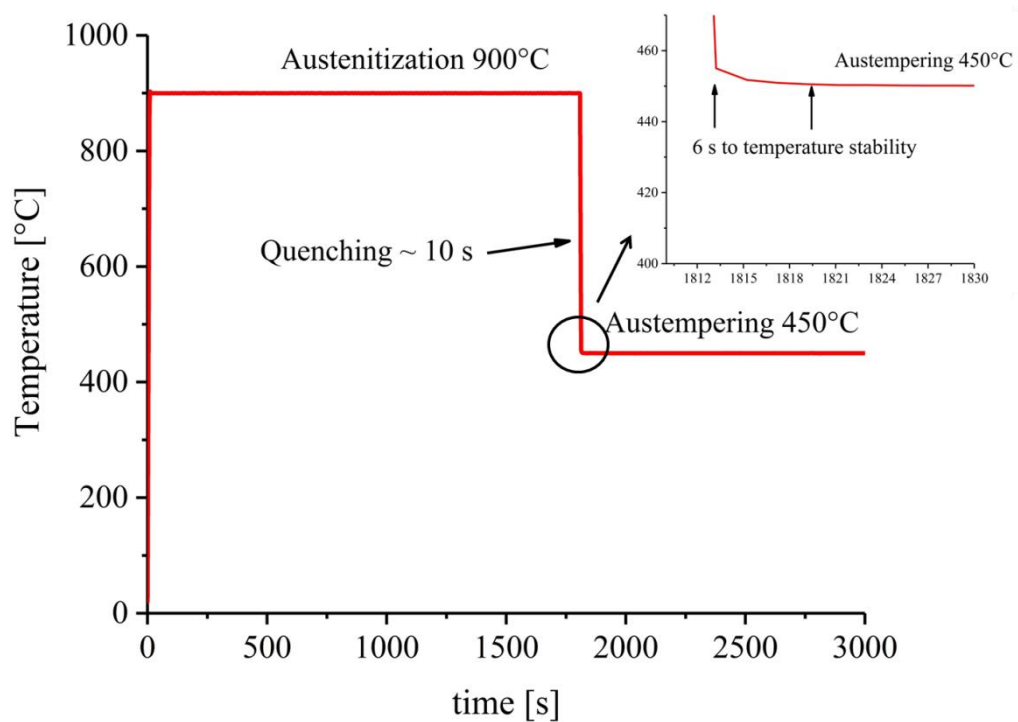


Figure 4.1 Measured temperature curve of the ADI heat treatment process by using quenching dilatometer showing the excellent temperature stability of this setup.

4.6 Atom-Probe-Tomography (APT)

To visualize the carbon distribution on the atomic level APT measurements were performed under the conditions shown in table 4.4. From three separately austempered ADI samples ($T_{Aus} = 300^{\circ}\text{C}$, 375°C and 425°C) small needlelike specimen for APT measurements

were prepared by standard electro-polishing method [Djla13]. The size of the needle tip area is about 250 nm × 60 nm × 60 nm. The chemical compositions in austenite, ferrite grains and their interface boundaries have been determined. In addition, the spatial structure of phases with a grain size smaller than 50 nm can be characterized using APT.

Table 4.4 Atom probe tomography measurement parameters.

APT mode	Detection rate	Pulse rate	Pulse energy/fraction	Temperature
Voltage mode	0.5 %	200 kHz	50 pJ	50 K
Laser mode	0.5 %	200 kHz	20 %	50 K

4.7 Determination of M_s -Start –Temperature

In order to determine the M_s temperature as a function of different austempering temperatures and Ni contents dilatometry as well as neutron diffraction was used.

4.7.1 Dilatometer

A Bähr DIL805 quenching dilatometer with induction heating was used to determine M_s of ADI samples above room temperature. The sample temperature was measured by a thermocouple welded on its surface. Each sample was heated with a heating rate of 200 K/s to 1173 K (900 °C) and austenitized at this temperature for 30 min until the carbon content equilibrium in austenite was reached [Lmei13], followed by rapid quenching to austempering temperature (573 K (300 °C), 623 K (350 °C) and 673 K (400 °C)) with a cooling rate of 100 K/s. The austempering time varied from 0 min to 20 min (incomplete austempering). After austempering the samples were quenched with helium gas with a constant cooling rate of 2 K/s to room temperature. M_s was determined as the point of change in the volume expansion according to Yang and Badeshia [Hsya07].

4.7.2 Neutron diffraction

For samples austempered longer than 20 min the M_s temperature is below room temperature at which the phase transformation could not be observed using the dilatometer. Therefore nine groups of ADI samples (heat treatment and chemical composition are the same as for the compression samples in table 4.2) austempered longer than 20 min were quenched in a modified continuous-flow cryostat to different temperatures between 77 K and 160 K (see Figure 4.2 for this setup). The austempering times (e.g. 22 min at $T_{Aus}=673$ K (400 °C), 30 min at 623 K (350 °C) and 60 min at 573 K (300 °C)) were chosen according to Saal [Psaa16]

as the point in time when the phase transformation reaches its plateau and the carbon content stays constant. High resolution neutron powder diffraction data were taken from the samples and quantitative phase analysis was performed to calculate the resulting martensite volume fraction f_M with respect to the initial austenite fraction f_A .

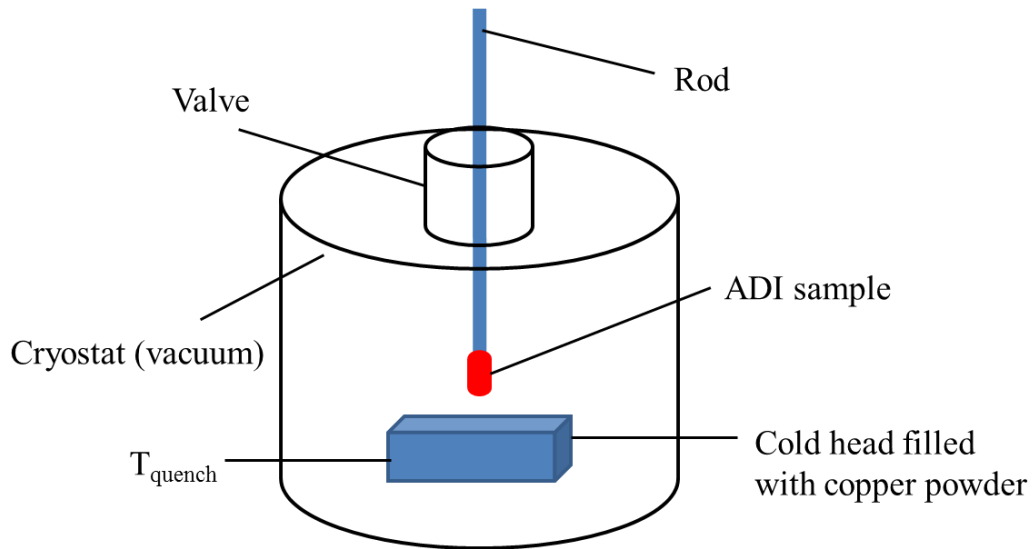


Figure 4.2 Configuration of the modified continuous-flow cryostat with a bed of copper powder installed on its cold head. The samples were then mounted on a moveable rod and introduced into the cryostat via a vacuum valve into the copper powder to be quenched down to the desired temperature.

Table 4.5 Initial austenite and ferrite phase fraction in ADI (with 3 different nickel content, austenitized at 1173 K (900 °C) and austempered at 3 different temperatures) from Rietveld-refinement of the neutron diffraction data using Maud (error bars are calculated as the mean deviation from the results of the refinements when changing different line broadening, size-strain models during the fitting process). The phase fractions of the initial heat treated samples were derived without taking into account texture.

Austempering Temperature [K]	573 (300 °C)		623 (350 °C)		673 (400 °C)	
	Austenite	Ferrite	Austenite	Ferrite	Austenite	Ferrite
0 wt% Ni	22.4(0.3)	77.6(0.3)	33.5(0.9)	66.5(1.0)	40.2(1.2)	59.8(1.2)
0.5 wt% Ni	22.1(0.2)	77.9(0.2)	35.8(1.1)	64.2(1.1)	46.1(1.4)	53.9(1.4)
1.5 wt% Ni	25.9(0.3)	74.1(0.3)	39.6(0.5)	60.4(0.5)	47.2(1.4)	52.8(1.3)

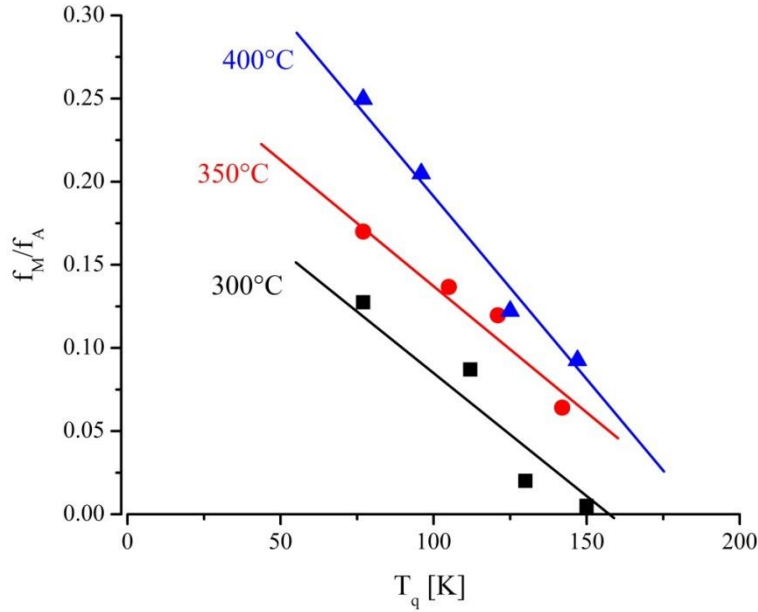


Figure 4.3 Fraction of martensite f_M/f_A in ADI (0wt% Ni) vs. T_q quench temperature. The samples were austempered at 300°C, 350°C and 400°C, respectively.

Exemplarily, the results of samples with 0wt% Ni are shown in Figure 4.3 as a function of quenching temperature. From the calculated martensite fractions the M_s temperature can be calculated using the Koistinen-Marburger (K-M) [Dpko59] relation as described later in detail in section 5.5.

4.8 Small angle scattering using neutron diffraction

Small angle neutron scattering (SANS) is well suited for characterizing the size distribution of nm-sized particles in ADI. The small angle scattering measurements using neutron diffraction were carried out at the SANS-1 instrument of FRM II [Ahei15]. The ADI material contains ferromagnetic ferrite and nonmagnetic austenite, so the SANS signal consists of a magnetic part and a nuclear part. Only the nuclear part can reveal the grain size distribution. In order to obtain the information on the nuclear part more accurately, the two sets of ADI samples were measured by SANS-1 at an average neutron wavelength of $\lambda = 12$ nm in 0 Tesla/1.5 Tesla magnetic fields in order to be able to separate nuclear and magnetic scattering contributions. The sample-detector distance was set at 20m, 8m and 2m resulting in Q-range from 0.013 nm^{-1} to 2.6 nm^{-1} , where

$$Q = \frac{4\pi}{\lambda} \times \sin\theta \quad (4.1)$$

One of the sets of ADI samples was austenitized at 900°C and austempered separately at 275°C, 300°C, 350°C and 400°C without deformation. The other set of ADI samples was austempered at 350°C and compressed to 0%, 10%, 20%, 30% and 44% strain levels. The heat treatment and compression deformation conditions were as the same as in section 4.1 and 4.4, respectively.

4.9 Texture analysis using neutron diffraction

For all ADI samples complete pole figures of ferrite (110) and (200) and austenite (111) and (200) reflections were measured at the materials science diffractometer STRESS-SPEC at FRM II [Mhof15] with a wavelength of 1.68 Å using a Ge (311) monochromator. In the measurements the loading direction (LD) of the compression samples and the normal direction (ND) of the cold rolling samples were perpendicular to the incoming beam direction (Fig. 4.4).

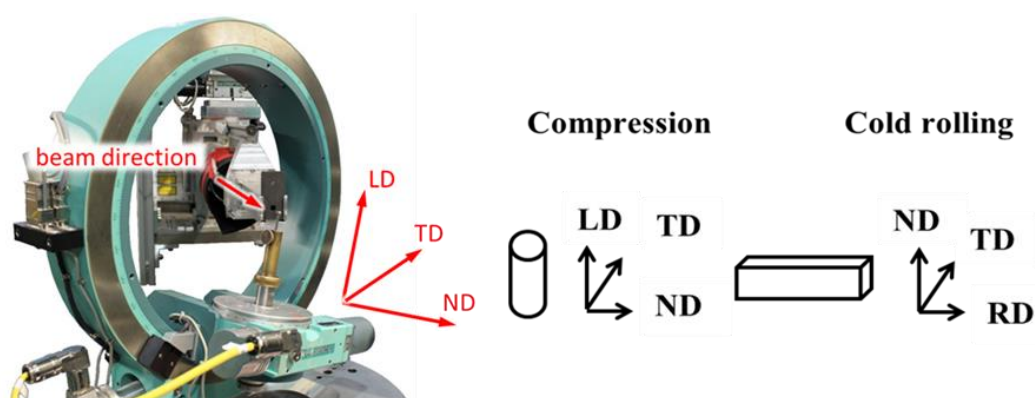


Figure 4.4 (Left) Measurement configuration with a compression sample at STRESS-SPEC [Mhof15]. (Right) Definitions of the sample coordinate system of the compression (and tension) and cold rolling specimen used for pole figure measurements. LD: loading direction; ND: normal direction; TD: transverse direction; RD: rolling direction.

The orientation distribution functions of crystallites (ODFs) and then the inverse pole figures were calculated from the measured complete pole figures using the harmonic method [Mdah89].

4.10 Phase analysis using neutron diffraction

High resolution neutron powder diffraction data were collected using the diffractometer SPODI at FRM II [Mhoe15] within a 2θ range = 10~152° and step width of $\Delta 2\theta = 0.05^\circ$. The wavelength was set to 1.5483 Å using a Ge (551) monochromator. For quantitative phase analysis the software package MAUD [Llut97, Mfer94] was used in which texture

information via the ODF and Rietveld refinement methods can be combined. The corresponding texture parameters were based on the ODF determined at diffractometer STRESS-SPEC.

5. Data analysis, Results and Discussion

5.1 Microstructure of ADI

5.1.1 Optical microscopy

After color etching with LePera-solution all the known phases in ADI can be characterized by different colors: spherical black graphite, needle like blue ferrite, white retained austenite region (Fig. 5.1a) and brown strain induced martensite within retained austenite region in compressed ADI (Fig. 5.1b).

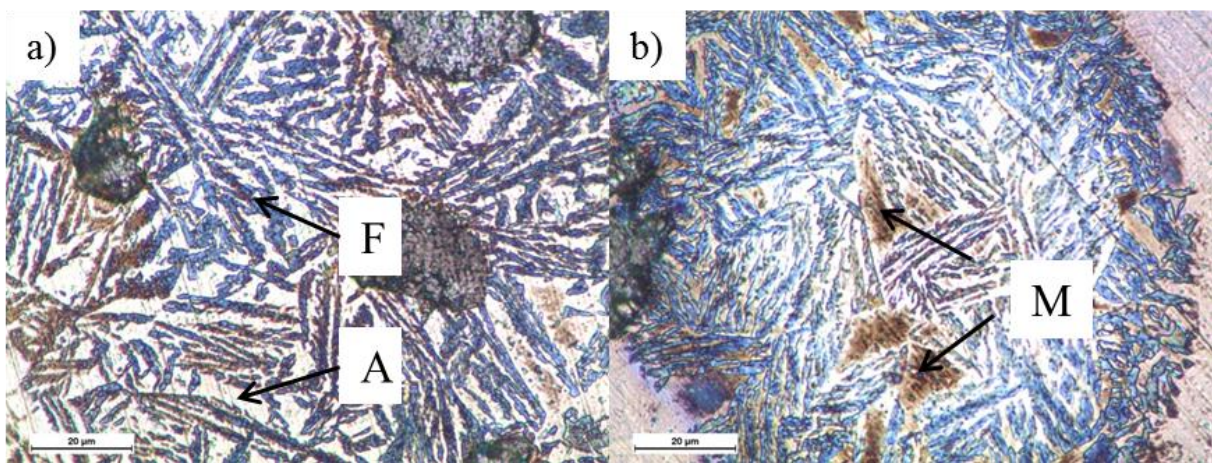


Figure 5.1 Microstructure of ADI under optical microscope, A = austenite, F = ferrite and M = martensite. a) unstrained ADI austempered at 400°C for 20 min. b) compressed ADI of a) to 42% strain level.

The existing duplex ferrite/austenite structure (ausferrite) which depends on the austempering temperature and time dominates the mechanical properties of ADI. The relationship between the morphology of ausferrite matrix, heat treatment conditions (austenitization temperature T_γ , austempering temperature T_{Aus} and time) and its influences to mechanical properties has already been studied in [Leop15, Psaa16, Mkac07] using the optical microscope and mechanical testing in details. Due to the limited magnification of optical microscope, the needle like blue ferrite region was estimated to have a length ranging from several microns up to tens of microns with a width of dozens or hundreds of nanometers to several micrometers, while the retained austenite grain size in the micrometer range. For martensite it was not possible to extract the grain size properly by optical microscopy.

5.1.2 SEM

Comparing the SEM image (Fig. 5.2) with the images from the optical microscope (Fig. 5.1), it is observed that the blue needle-like ferrite region in Figure 5.1 is actually the part which was corroded by the etching solution.

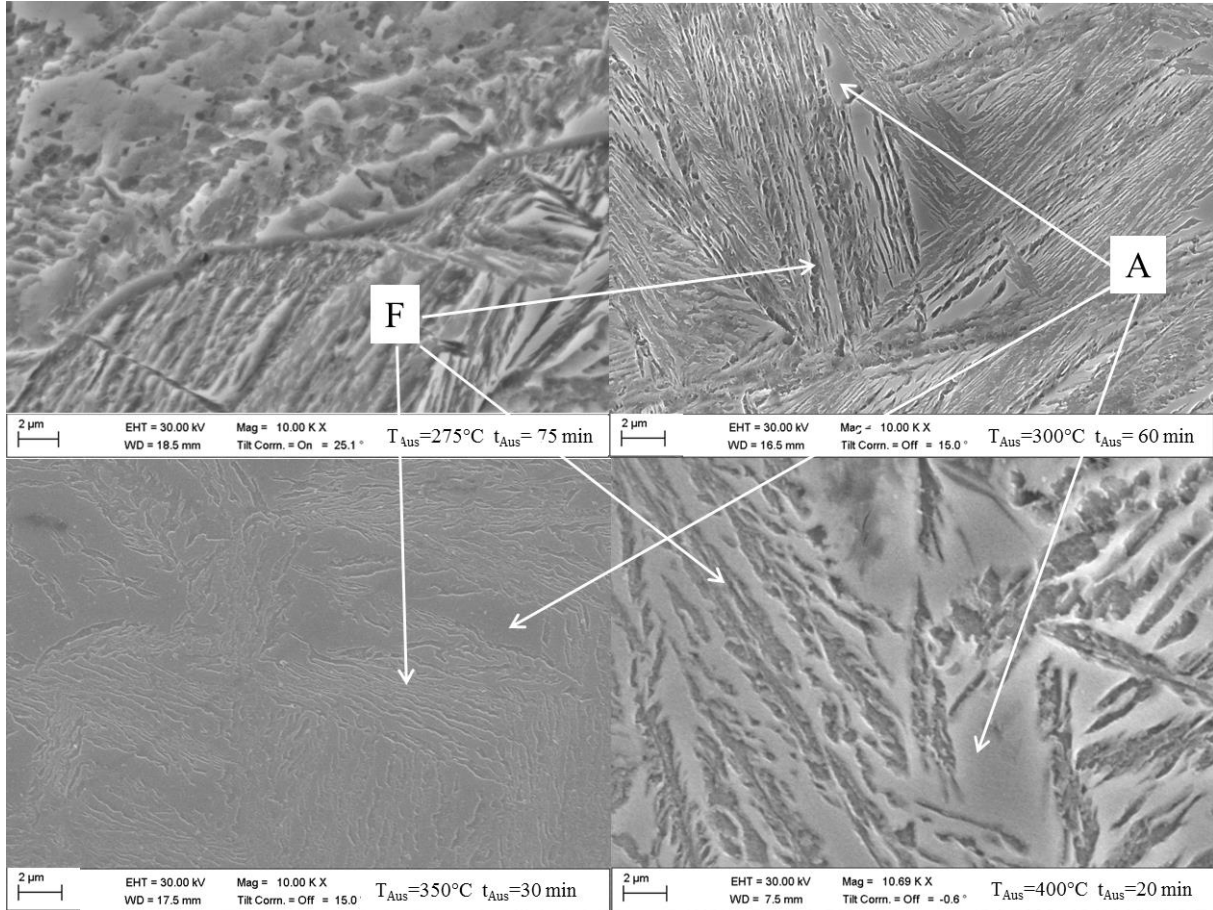


Figure 5.2 Microstructure of ADIs (austempered at $T_{Aus} = 275, 300, 350$ and 400 °C, austempering time varied by T_{Aus}) under SEM (Magnification 10000 \times). The degree of etching in sample austempered at 350 °C is less than that of other samples, so the color and morphology of phases appear different compared to the other samples shown here. The ADI austempered at 400 °C has been compressed to 30% strain level.

The ferrite region shows a clear dendritic structure and austenite region shows a blocky structure in the SEM (Fig. 5.2). However, the area of the eroded ferrite which was etched cannot fully reflect the size and the original appearance of its grain. In addition, SEM cannot provide clear grain boundary information for grains with grain size in nanometer range. Therefore SEM measurements are not able to confirm directly whether a continuous ferrite region stems from a single ferrite grain or not. As the same limitation in spatial resolution applies, electron backscatter diffraction (EBSD) is also not able to solve this problem.

Reducing the degree of etching and increasing the magnification of SEM, the microstructure of ADI presents a different view as shown in Figure 5.3.

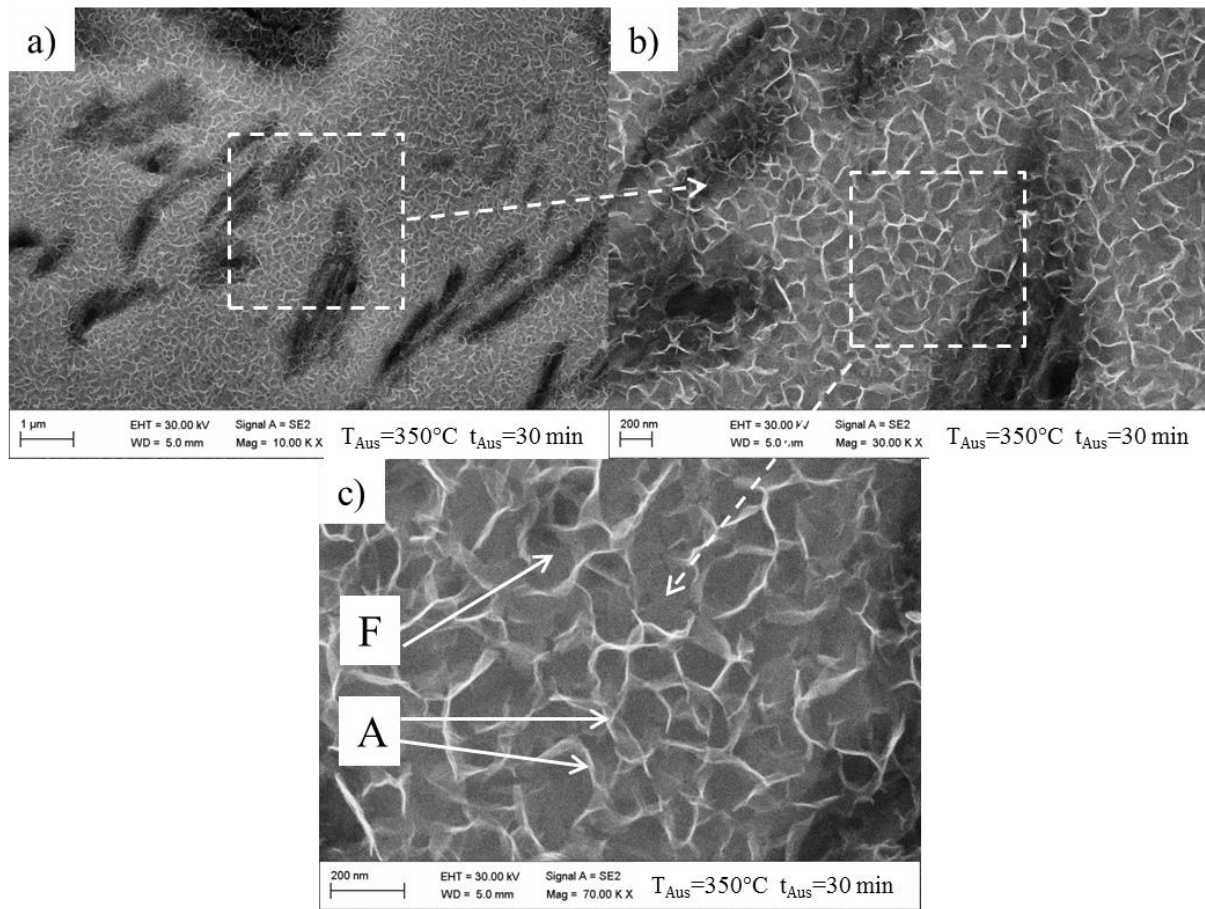


Figure 5.3 Microstructure of ADI austempered at 350°C for 30 min. a) 10000× magnification, b) 30000× magnification and c) 70000× magnification.

After mild etching, ferrite and austenite regions are clearly visible. The acicular black areas in Figure 5.3 a, b) correspond to the black areas considered to be ferrite in Figures 5.1 and 5.2. The surrounding grey areas correspond to the blocky austenite areas in Figures 5.1 and 5.2. In addition to that, a large number of irregular lamellar structures appear homogeneously distributed on the whole sample surface (Fig. 5.3).

The size of these lamellas are estimated to have a length of 100 ~ 200 nm and a width of 10 ~ 20 nm. These lamellar structures coincide with the austenite films simulations [Adbo17-1] and have been confirmed also later in section 5.1.3 in TEM measurements. The areas between the lamellar structures correspond to ferrite (Fig. 5.3 c). Hence the complete morphology of ferrite and austenite seems to be more complicated than the images shown in Figure 5.1 and 5.2 suggest, and it consist of acicular ferrite and blocky austenite and additional austenite films (Fig. 5.4) as suggested in the model of Boccardo [Adbo17-1].

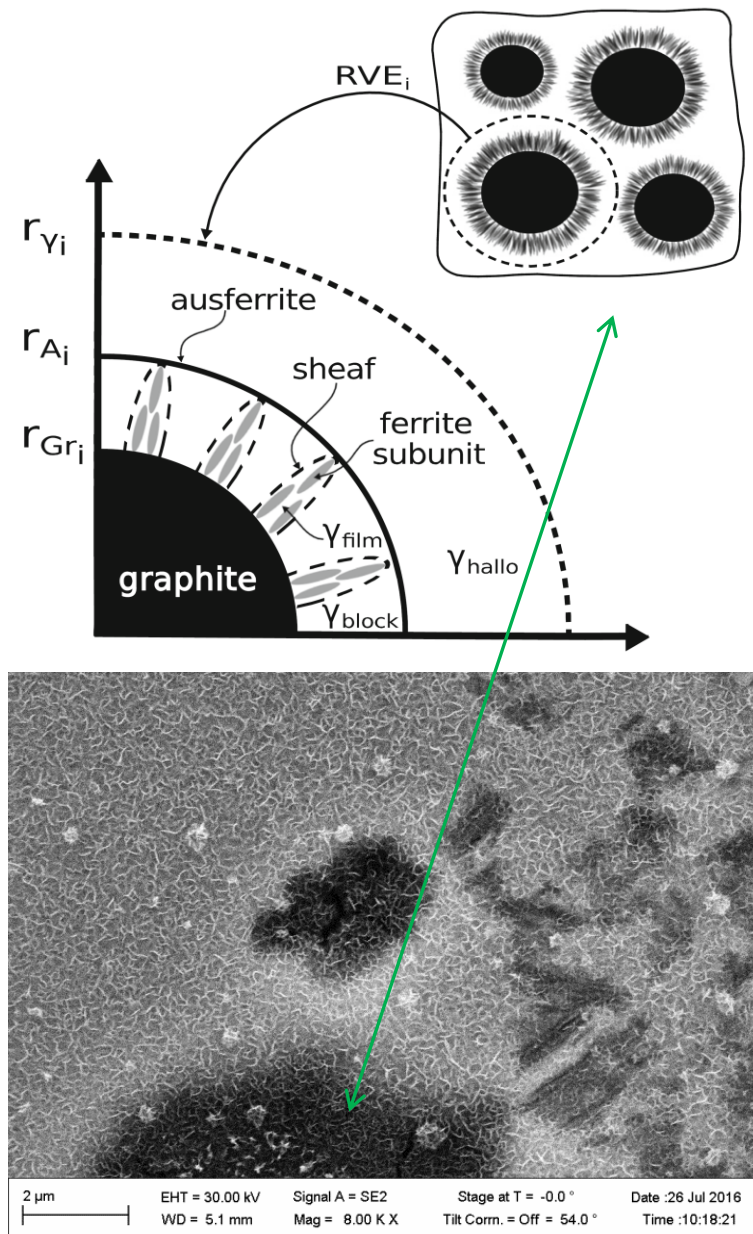


Figure 5.4 (top) Volume element of a graphite nodule in ADI, which shows the morphology of ausferrite as it is proposed to model the ausferritic transformation [Adbo17-1]. (bottom) Microstructure of ADI sample austempered at 350°C for 30 min.

5.1.3 TEM

TEM measurements on three ADI samples (austempered at 350°C, unstrained, strained and quenched) with much higher magnification and without etching effect (some grains are eroded out by etching solution) were applied to investigate the orientation relationship and the grain morphology of austenite, ferrite and martensite for more details. In contrast to the optical microscopy and the SEM the samples for TEM were prepared using electropolishing to thicknesses of 100 nm (see chapter 4.3 for details). Under this preparation condition, all the

phases (grains) in the observed area in TEM images are kept intact, unlike the samples prepared for SEM, some phase (ferrite) were eroded by the etching solution. It also explained why the morphology of the observed ADI is not exactly the same in TEM and SEM.

In previous studies of steels containing ferrite and austenite [Jbse13, Fgca08, Brsh14], ferrite was found exhibiting white colour and austenite exhibiting black colour in bright field TEM investigations (BF). Therefore we assume the same holds for ADI materials.

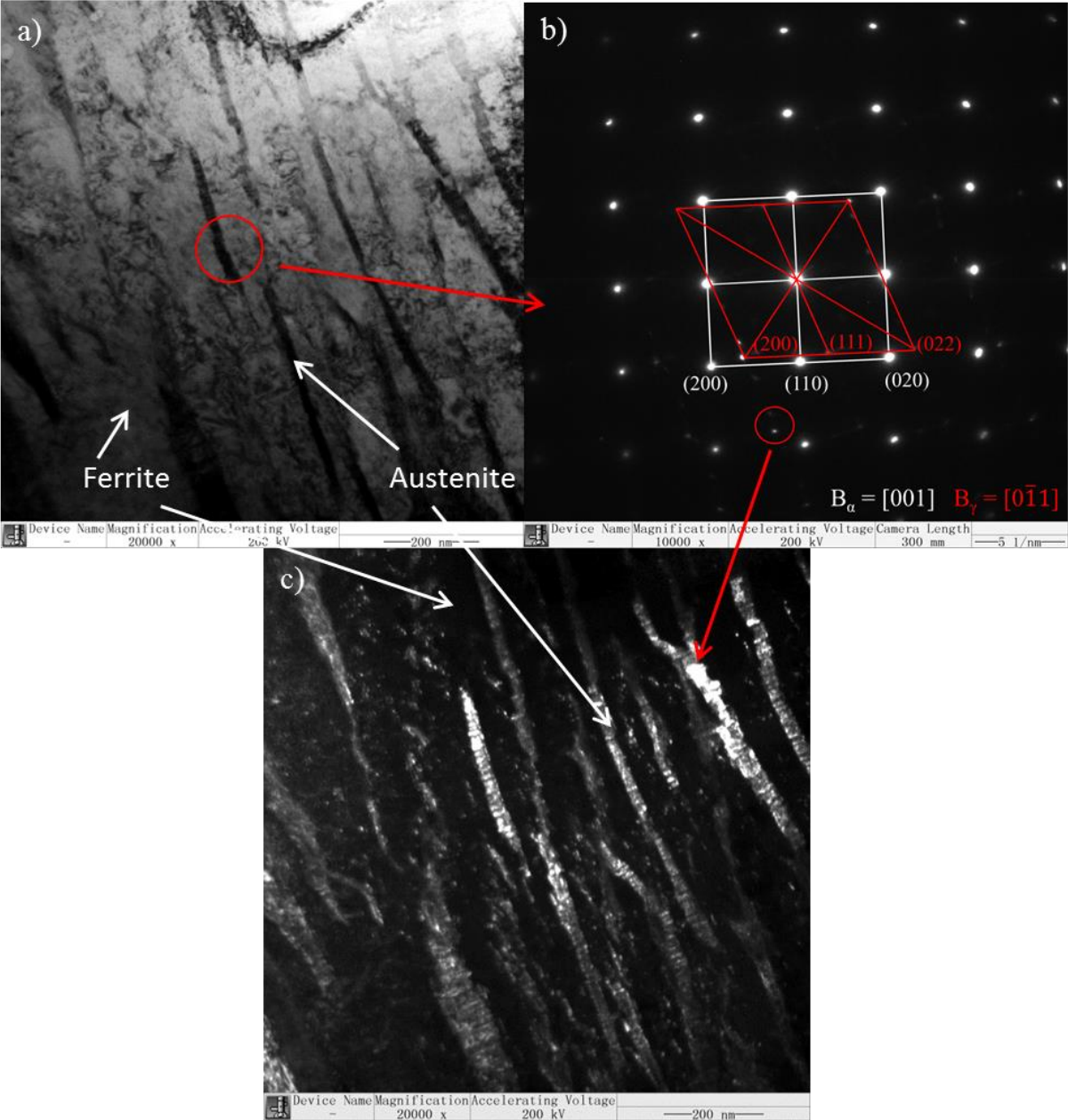


Figure 5.5 a) TEM micrograph (BF) of ADI austempered at 350°C for 30min. b) The corresponding SADP taken from the red circle in a). c) Dark field image of a) using the circle marked signal in b).

Figure 5.5 (a, b) shows a typical BF TEM image and its corresponding selected area diffraction pattern (SADP) pattern of ausferrite morphology in ADI austempered at 350°C. In this ADI sample, the morphology and orientation relationship of ferrite and austenite in ADI has been investigated. The shape of austenite grains is mainly needle-mesh like, rarely appearing in massive blocks (Fig. 5.5 c)). In contrast, the shape of ferrite is mostly massive. This is completely different from what was observed under the optical microscope (Fig. 5.1), but is quite consistent with the results observed from SEM (Fig. 5.3). According to the size and shape of austenite (Fig. 5.5 c), the needle-like phase appearing in Figure 5.3 has been confirmed as austenite. Combining Figures 5.3 and 5.5, the needle like austenite grain size can be estimated with a length of about 100~500 nm and width of 20~100 nm, respectively, the ferrite has a grain size of 50~300 nm. In addition, a typical N-W orientation relationship ($[001]_F // [0\bar{1}1]_A$) between austenite and ferrite was found in ADI (Fig. 5.5 b).

In the same ADI sample a small amount of carbide precipitation has been observed in the vicinity of austenite grains after intensive TEM investigation (Fig. 5.6 c)). Four types of stable carbides (θ -Fe₃C, Fe₆C, h-Fe₇C₃ and γ -Fe₂₃C₆) are the most likely to form in cast iron [Awie11, Cmfa09]. Due to the location of the carbide spots in SADP (Fig. 5.6 b), the crystal structure of carbide has been calculated to be closest to γ -Fe₂₃C₆. The formation of carbide provides a possible and reasonable explanation for the appearance of the carbon gap in ADI. The reason for its formation, location and chemical composition will be discussed in section 5.4 together with the APT results.

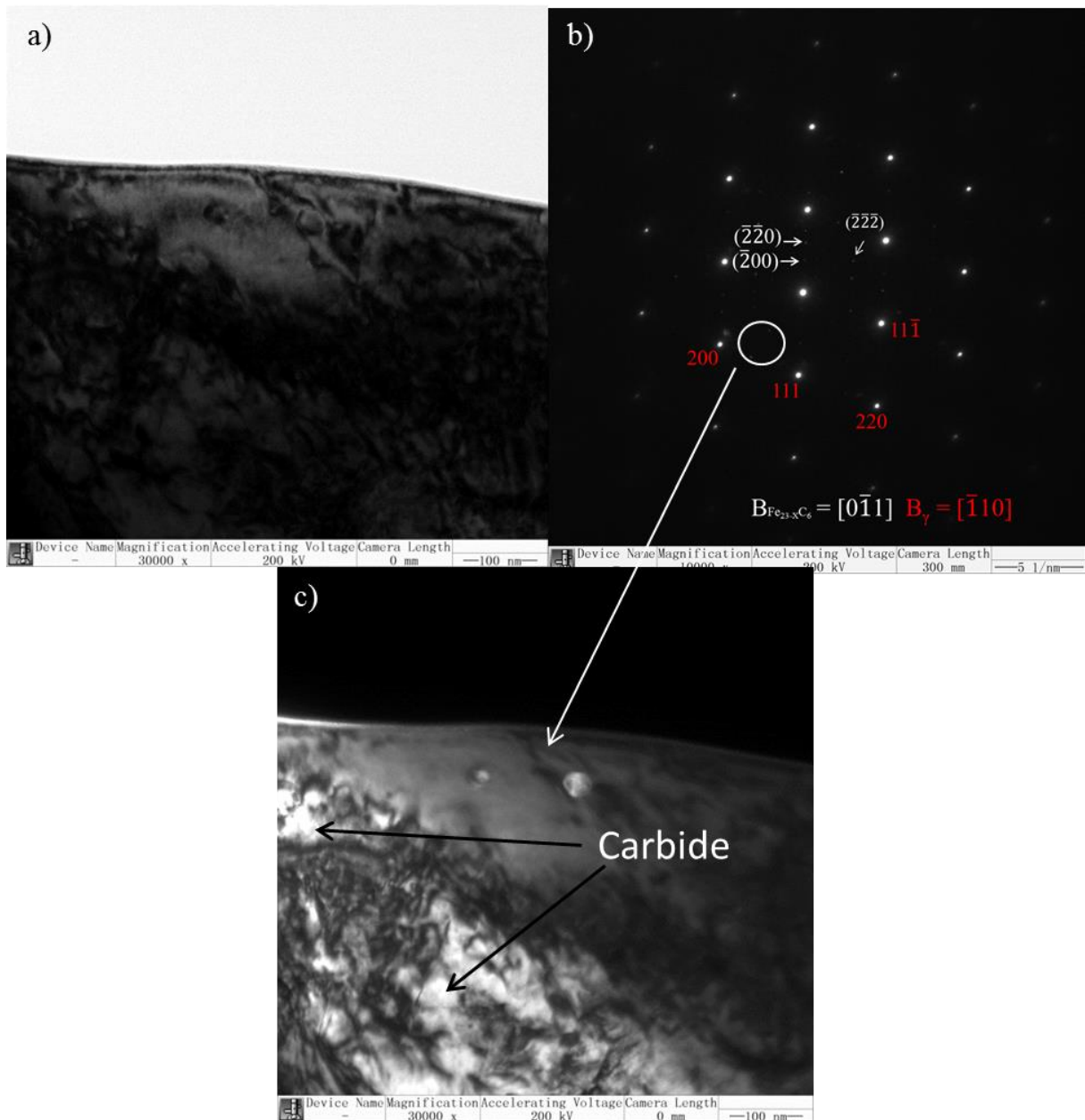


Figure 5.6 a) TEM micrograph (bright field) of ADI austempered at 350°C for 30min. b) The corresponding SADP taken from the whole area of a). c) Dark field image of a) using the circle marked signal in b).

Athermal martensite in quenched ADI material has been found using SADP to have a typical K-S orientation relationship with the surrounding austenite matrix (Fig. 5.7 a, b). The crystal structure of *bct* martensite is close to *bcc* ferrite and exhibits a light grey colour in the BF TEM image (Fig. 5.7 c). Due to the constraints of the initial retained austenite morphology, the martensite grain morphology is not regular, and varies between small lath and plate like shapes with a grain size of 10~50 nm.

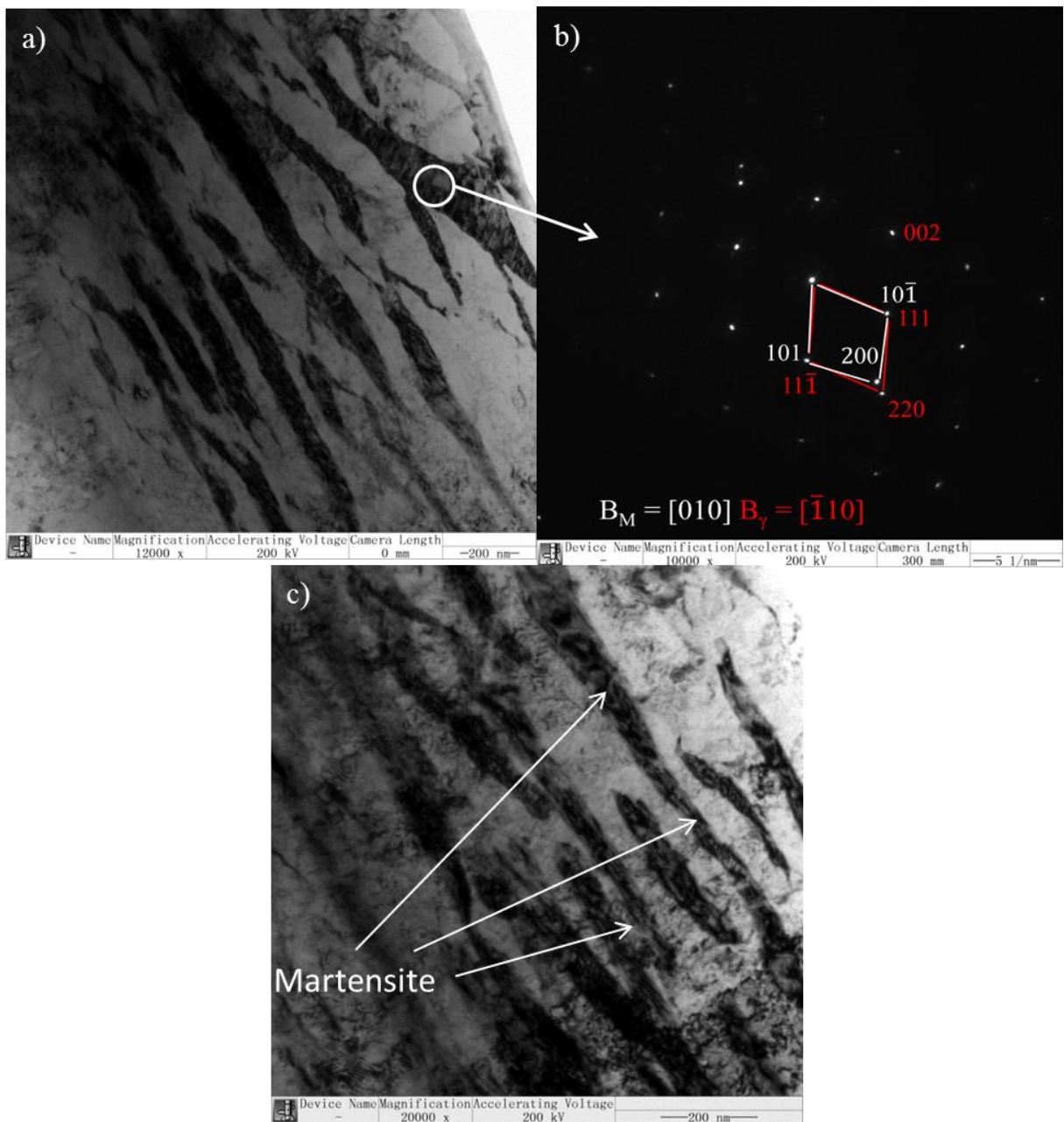


Figure 5.7 a) TEM micrograph (bright field) of ADI austempered at 350°C for 30min and quenched with liquid N₂ to 77K. b) The corresponding SADP taken from the whole area of a). c) Bright field image of the sample at another location where the typical morphology of martensite in the quenched sample can be more clearly seen. Martensite can be identified as white/grey areas in the black needles.

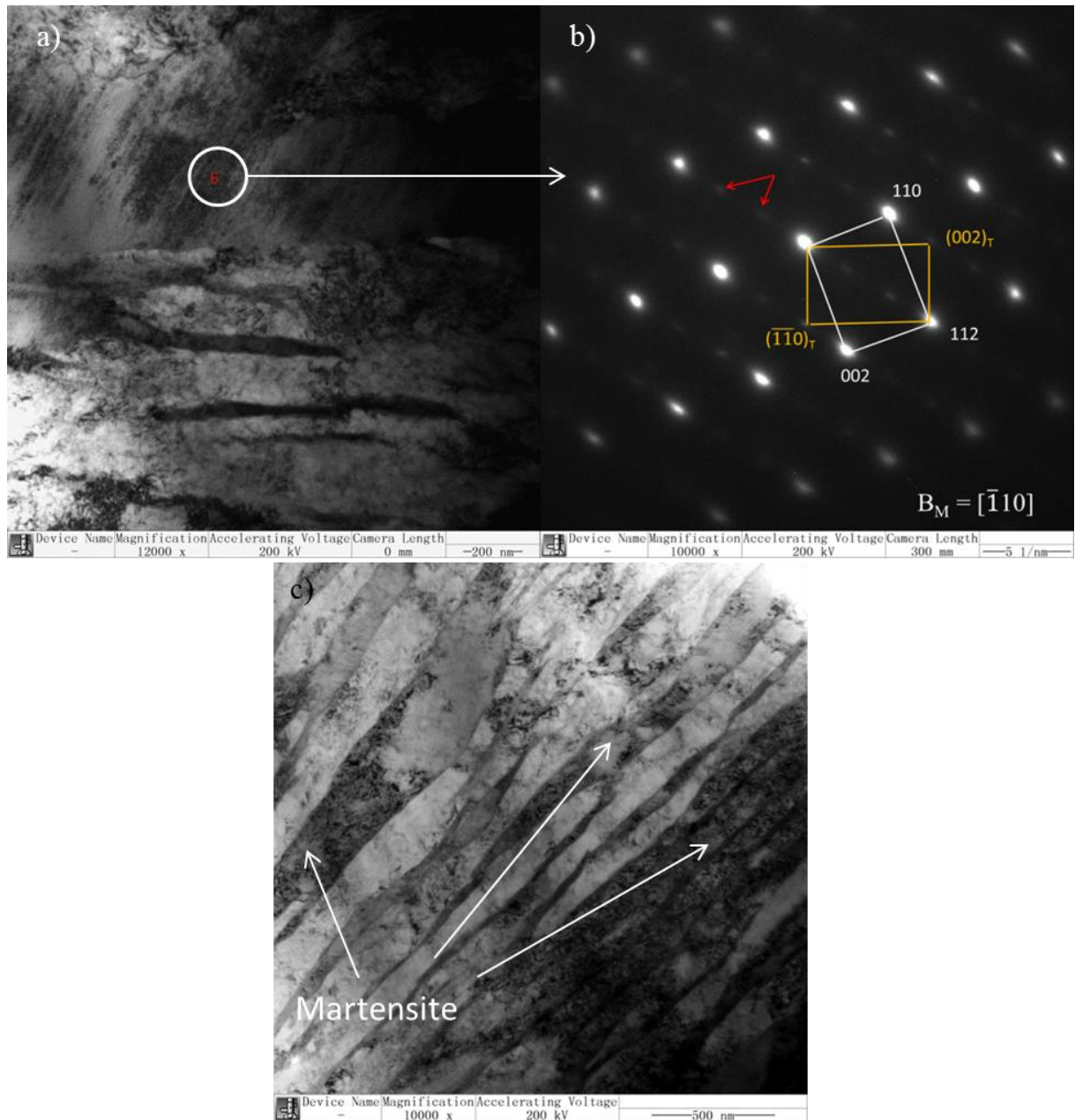


Figure 5.8 a) TEM micrograph (bright field) of ADI austempered at 350°C for 30min and compressed to 42% strain level. b) The corresponding SADP taken from the whole area of a), extra spots were marked with red arrow. c) Bright field image of the sample at another location where the second morphology of martensite in the compressed sample is shown.

Different from the athermal martensite, the morphology of strain induced martensite is composed of plate like martensite as main component and twinned martensite within plate martensite matrix as substructure (Fig. 5.8 a). The SADP (Fig. 5.8 b) indicates the twin spots (yellow) in addition to the normal *bct* $[\bar{1}10]$ zone diffraction spots and the red arrows indicate two extra twin spots at $1/3(112)$ and $2/3(112)$ in addition to the main martensite matrix. These extra spots have been observed frequently in martensitic steels and are always considered to

be double diffraction of the $\{112\}\langle 111\rangle$ twinning structure between the martensite matrix and twin [Hyle10, Asto13]. In a recent report these extra spots have been confirmed by the high resolution TEM, correspond to a nanoscale, metastable ω phase in high carbon steel [Twli15].

5.2 Size distribution of different phases in ADI

Commonly used line broadening analysis methods for the grain size and microstrain estimation are based on the integral breadth method [Dbal99], Fourier method [Bewa50] and double Voigt method [Jila80]. The whole calculation process of the simplified integral breadth method is straightforward and is the basis for all the other line broadening analysis methods. It works very well and effective if the peak shapes are close to pure Gaussian or Lorentzian. The Fourier method is susceptible to error due to peak overlapping which limits its use for crystal structures with high complexity. Nevertheless, it is the most general method of extracting size and strain information. Finally the double Voigt method offers both feasibility and accuracy, and is for example implemented in the Rietveld refinement code MAUD, which was used in this work. The relationship between grain size, microstrain and austempering temperature T_{Aus} has been investigated in section 5.2.1 using line broadening analysis for the synchrotron diffraction patterns of ADI austempered at different temperatures. The results were calculated using different methods for comparison. In section 5.2.2, the influences of austempering temperature and plastic deformation on the grain size distribution of different phases in ADI have been investigated by small angle neutron scattering.

5.2.1 Determination of size and strain using integral breadth and double Voigt method

The theoretical basis for size-strain calculation using line broadening analysis begins with calculation of integral breadth β . The whole process of simplified integral breadth method (Williamson-Hall plot) has been introduced as follows. The calculation process with double Voigt method is basically the same as integral breadth method (see [Dbal99]).

For Gaussian and Lorentzian peak shape functions the relationship between integral breadth and full width at half maximum Γ can be expressed by equation (5.1).

$$\text{Lorentzian } \beta = (\pi/2) \times \Gamma \quad (5.1a)$$

$$\text{Gaussian } \beta = \{\pi/(4 \times \ln 2)\}^{1/2} \times \Gamma \quad (5.1b)$$

β : Integral breadth, the width of a rectangle with the same height and area as the diffraction peak, in radians 2θ .

Γ : Full width at half maximum.

The grain size and micro-strain have the following relationship with integral breadth β and theta θ :

$$D_v = K \times \lambda / \{\beta \times \cos\theta\} \quad (5.2a)$$

$$\varepsilon_{str} = \beta / \{4 \times \tan\theta\} \quad (5.2b)$$

D_v : Volume weighted crystallite size

ε_{str} : Weighted average strain

K : Scherrer constant, is in the range of 0.87 ~ 1.0.

λ : Wavelength of the synchrotron beam.

The observed integral breadth is composed of three parts: instrumental broadening β_{inst} , crystallite size β_{size} and microstrain β_{strain} . The instrumental peak broadening β_{inst} can be obtained after Rietveld refinement on the line broadening standard reference sample LaB₆. The equation (5.3a) can then be converted to (5.3b) after substitution of equation (5.2) into (5.3a).

$$\text{Lorentzian: } \{\beta_{obs} - \beta_{inst}\} = \beta_{size} + \beta_{strain}$$

$$\text{Gaussian: } \{\beta_{obs}^2 - \beta_{inst}^2\} = \beta_{size}^2 + \beta_{strain}^2 \quad (5.3a)$$

$$\text{Lorentzian: } \{\beta_{obs} - \beta_{inst}\} \times \cos\theta = \lambda/D_v + 4\varepsilon_{str} \times \sin\theta$$

$$\text{Gaussian: } \{\beta_{obs}^2 - \beta_{inst}^2\} \times \cos^2\theta = \lambda^2/D_v^2 + 16\varepsilon_{strain}^2 \times \sin^2\theta \quad (5.3b)$$

β_{obs} , β_{inst} , β_{size} , β_{strain} : Observed integral breadth, Integral breadth caused by instrument, crystallite size and microstrain.

The calculated grain size and microstrain of austenite, ferrite of ADIs using simplified integral breadth method and double Voigt method by analysing the synchrotron diffraction pattern of experiment part 4.5 are shown in Figures 5.9 and 5.10, respectively.

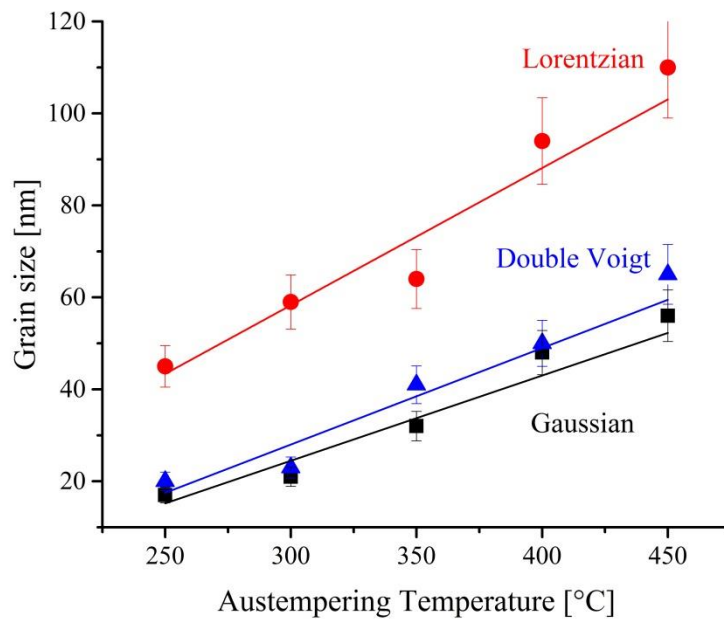


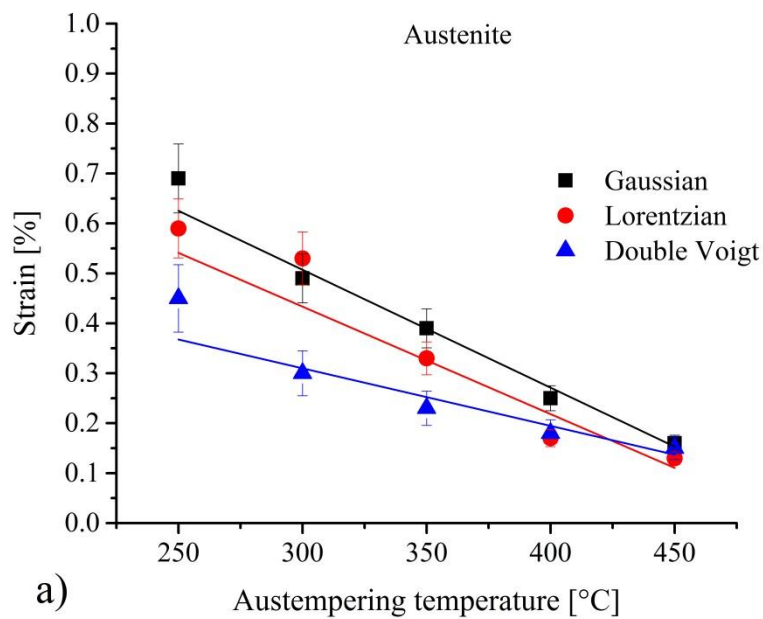
Figure 5.9 Calculated average grain size of austenite using integral breadth and double Voigt method.

Due to the instrument resolution, only grain size below about 100 nm can be accurately evaluated by synchrotron diffraction. The results of SEM and TEM (section 5.1.2 and 5.1.3) have shown that the size of many ferrite grains is much larger than 100 nm, outside of the accurate calculation range. This is reflected in the case of using integral breadth method to calculate the ferrite grain size and strain where it is found, that the size part β_{size} , in equation (5.3a) is almost zero or even negative. Therefore, one can conclude that the full width at half maximum changes of ferrite reflections in different austempered ADIs are mainly caused by instrumental effects and microstrains. Although the size of many austenite grains is less than 100nm (Fig. 5.5), austenite with grain size larger than 100nm are clearly present in form of blocky austenite in ADI (Fig. 5.7). Therefore, the calculated average value of austenite grain size (Fig. 5.9) can only describe the relationship between the crystallite size of a part of the austenite grains and austempering temperature, not the average of all austenite grains. In the existing powder diffraction techniques, there is no method to accurately measure grain size values spanning a range from a few nanometers to a few microns. However, the results in Figure 5.9 indicate, a proportional relationship of the austenite grain size to austempering temperature consistent with the observed results of optical microscopy and SEM.

The discussion on the relationship between grain size and austempering temperature is based on the mechanism of austenite to ferrite transformation. Whether austenite or ferrite, their grain sizes are in nanometer-scale (section 5.1.3), and the phase transformations kinetic is controlled by ferrite nucleation rate and carbon diffusion [Jspe03]. As the austempering

temperature increases, more and larger ferrite grains nucleate in the unit time. In addition, the carbon diffusion rate is accelerated, so that the carbon concentration profile at the austenite/ferrite interface achieved paraequilibrium more rapidly [Jspe03] (= phase transformation stop). So at high austempering temperature larger austenite and ferrite are formed eventually while the ferrite and austenite formed at low austempering temperature have comparably smaller grain sizes. Further results and discussion the relationship between grain size and austempering temperature is given in section 5.2.2.

The microstrain (lattice strain) caused by the phase transformation, calculated by the integral breadth and double-Voigt method are illustrated in Figure 5.10.



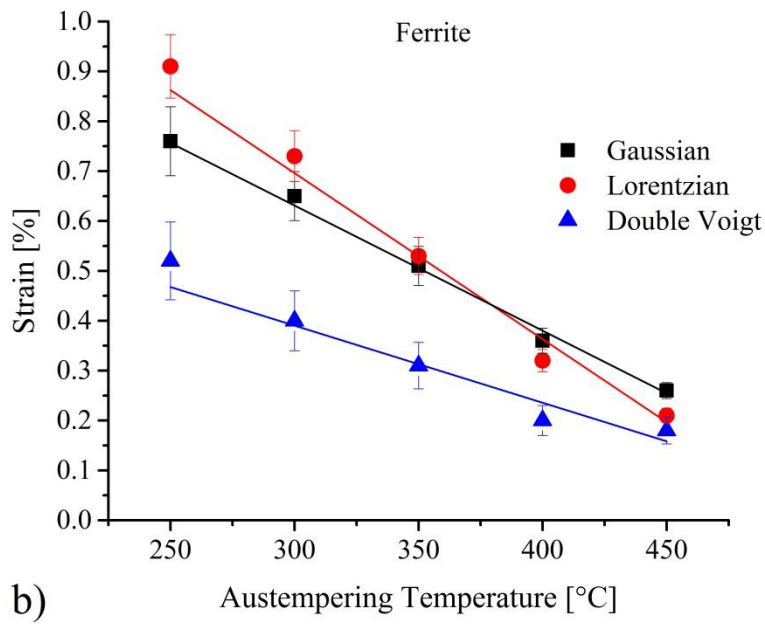


Figure 5.10 Calculated average microstrain of austenite a) and ferrite b) using integral breadth (Williamson-Hall plot) and double-Voigt method.

The microstrains in ferrite and austenite are inversely proportional to the austempering temperature and the values calculated with the various methods are at the same level. The microstrain in ferrite is mainly caused by interstitial carbon. The inverse linear relationship of microstrain in ferrite and austempering temperature (Fig. 5.10 b) can be explained by the relationship of the content of supersaturated carbon in ferrite and austempering temperature and will be discussed in more details in chapters 5.3 and 5.4. However, the carbon content in austenite and austempering temperature does not have a similar relationship as in ferrite. Previous studies with neutron diffraction confirmed that the carbon content of austenite in ADI austempered at 350°C was higher than in ADI austempered at other temperatures [Leop15]. Moreover, the carbon solubility of austenite is much higher than that of ferrite, so that the main reason for the appearance of microstrain in austenite is most likely the constraints imposed by the surrounding ferrite grains.

5.2.2 Size distribution of austenite and ferrite using small angle scattering

The small-angle neutron diffraction SANS can be used to calculate grain size distributions of different phases in ADI, which cannot be done by the other methods such as line broadening analysis, SEM and TEM. Nevertheless, to distinguish the different phases within the size distribution function requires the knowledge from other experiments. The main purpose of the SANS experiments on the two groups of samples in section 4.8 is to

understand the effect of austempering temperature and plastic deformation on the size distribution.

According to the equation (5.4) and the experimental settings (see section 4.8), the measureable range of grain size was from 3 nm to 162 nm in austempered ADI samples (Fig. 5.11 a) and from 3 nm to 465 nm in compressed ADI samples (Fig. 5.11 b).

$$d = \frac{2\pi}{q} \quad (5.4)$$

The SANS intensity distribution contains size information of carbide (shown in section 5.1, Figure 5.6), austenite and part of ferrite. The signal is composed of 2 components, a nuclear $Nuc(q)$ and magnetic $Mag(q)$ scattering contribution. The information about grain size distribution is mainly contained in $Nuc(q)$.

$$I(q, B) = Nuc(q)^2 + Mag(q)^2 \times \sin^2\Psi(q, B) \quad (5.5)$$

After comparing and calculating the measured data of samples with 0 Tesla and 1.5 Tesla, the normalized scattering profile of $Nuc(q)$ has been extracted from the measured data using standard methods [Lafe87] and shown in Figure 5.11.

Figure 5.11 a) has shown the normalized scattering intensities of unstrained, austempered ADI samples. The curves in Figure 5.11 a) indicate, the intensities of all the curves $I(q = 0)$ are almost the same³, which means, the austempering temperature has no significant effect on the average grain size and morphology of austenite and ferrite. The average grain size of austenite and ferrite in ADIs austempered at different temperatures should be all at the same order of magnitude.

³ Intensity ~ scattering volume V_s , V_s is proportional to the volume of particles in the measuring range. It changed, when size distribution and number of particles changed.

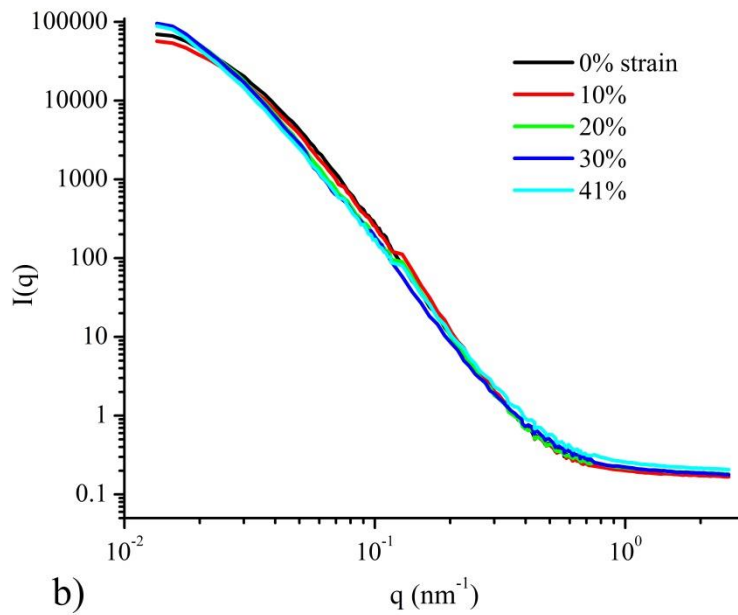
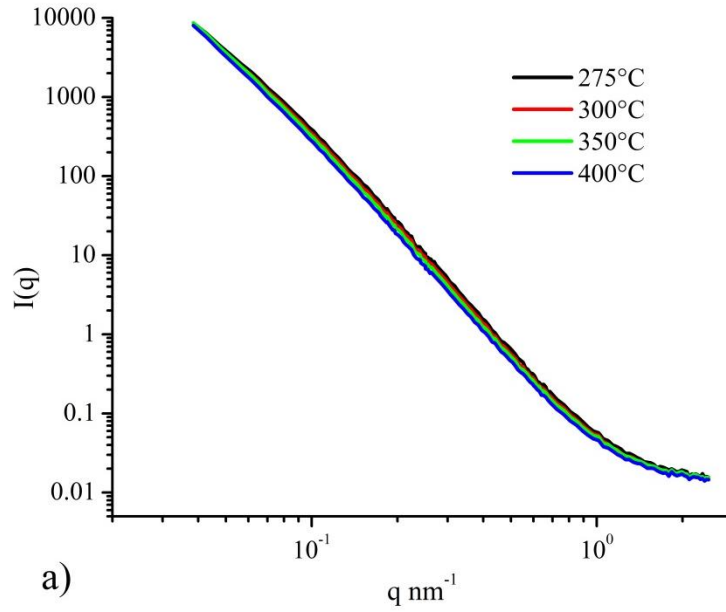


Figure 5.11 a) The measured and normalized SANS data ($Nuc(q)$) of ADIs austempered at 275°C, 300°C, 350°C and 400°C. Q range from 0.03846 nm^{-1} to 2.469 nm^{-1} , refers to a particle size range from 2.5 nm to 162 nm.
 b) The measured and normalized SANS data ($Nuc(q)$) of ADIs austempered at 350°C and plastic deformed from 0% to 41% strain level. Q range from 0.01348 nm^{-1} to 2.586 nm^{-1} , refers to a particle size range from 2.4 nm to 466 nm.

Figure 5.11 b) shows the normalized scattering intensities of compressively deformed ADI samples. The intensities $I(q = 0)$ of curves in Figure 5.11 b are significantly different from

those of curves in Figure 5.11 a, indicating that the plastic deformation changed the scattering volume V_s . However, the shape of the curves is not changing significantly, indicating that the morphology of the grains in ADI is kept basically the same before and after plastic deformation.

According to the observed microstructure of carbide, ferrite and austenite shown by TEM, APT (see chapter 5.4) and the typical example plots for different types of related scattering objects [Jkoh13], the grain sizes of ADI are divided into a large particle region ($d \geq 50$ nm, austenite and ferrite) and a small particle region ($d \leq 50$ nm, carbide and carbon cluster). Only when the appropriate models are selected, the fitting results are meaningful and can truly reflect the grain morphology and size. The choice of the model is divided into three steps. First, the possible models to be used are selected after the observation of SEM, TEM and APT on the samples. Second, according to the comparison of scattering plots and example plots of the models to be used, the models for further fitting with software can be determined. Third, the different selected models after step 2 are substituted into software SASfit [Jkoh13] for fitting and the results are compared with other experimental results (SEM, TEM, APT) to determine the most appropriate models. Finally, two related models (form factor for scattering object) were selected in the software SASfit for fitting. The model ‘‘Gaussian chain’’ [Jkoh13] is more suitable for large particles, while the ‘‘Benoit’’ model [Jkoh13] is suitable for the small particles. The parameters of fitting have been substituted in equation (5.6) for the calculation of particle size distribution function and the results were illustrated in Figure 5.12, 5.13 and 5.14.

$$h(R) = \frac{N_R}{N} = \frac{1}{R\sigma\sqrt{2\pi}} \exp\left(-\frac{\ln(R/R_0)^2}{2\sigma^2}\right) \quad (5.6)$$

$h(R)$: Particle weighted size distribution function.

N_R : Number of particles with size R .

N : Total number of particles.

R : Particles size in nm.

R_0 : Average particle size in nm.

σ : Width parameter of normal distribution function.

Most of the particles with an average diameter less than 50 nm in ADI material are carbides or carbon cluster (Fig. 5.12a). Due to their small volume fraction, they are difficult to detect in the standard phase analysis procedure using diffraction methods (section 5.7). Comparing the TEM bright field and dark field images in Figure 5.5 with the result of particle size distribution function, it was observed, that the uneven colour of the white ferrite and

black austenite regions is due to the fact that these two phases are intertwined and mixed. Therefore, the white and black regions (ferrite and austenite) in the TEM images (see Figure 5.5 as example) cannot completely display the real morphology of the phases and the particle size can be described more accurately by the particle size distribution function.

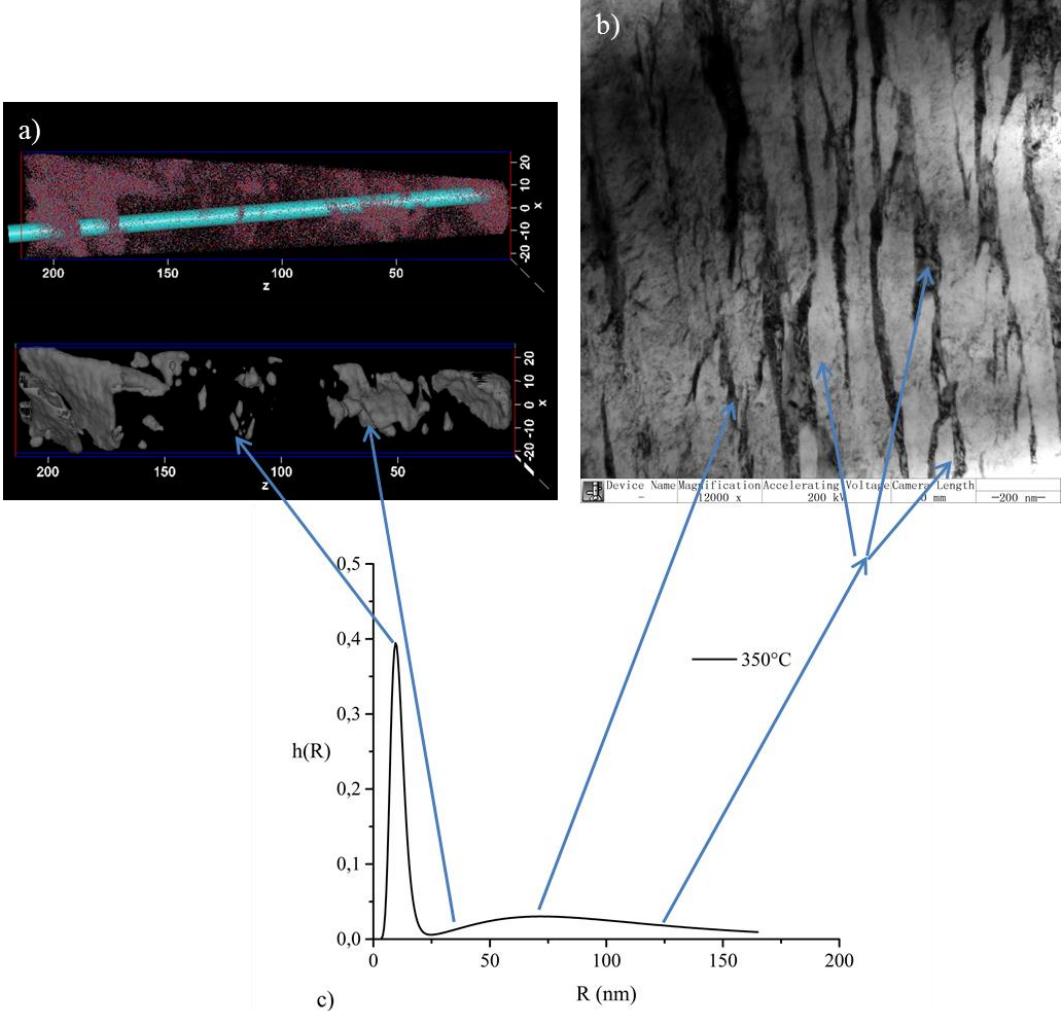


Figure 5.12 a) 3-D APT map of carbon atoms in ferrite and the 3-D morphology of corresponding carbon enriched areas in ADI austempered at 350°C.
 b) TEM micrograph (BF) of ADI austempered at 350°C.
 c) Particle size distribution function of ADI austempered at 350°C.

The number of small particles represented by carbide and carbon clusters decreases as the austempering temperature increases (Fig. 5.13). This is consistent with the assumption that the carbon gap decreases with increasing austempering temperature (see chapter 5.4.3 for details). Such reduction is achieved by reducing the number of particles rather than changing the average particle size. The austenite and ferrite grain size, which represent the large particles, increases with increasing austempering temperature and has a wide distribution range. Due to

the limited measuring range ($d \leq 165$ nm), no information on even larger particles can be derived.

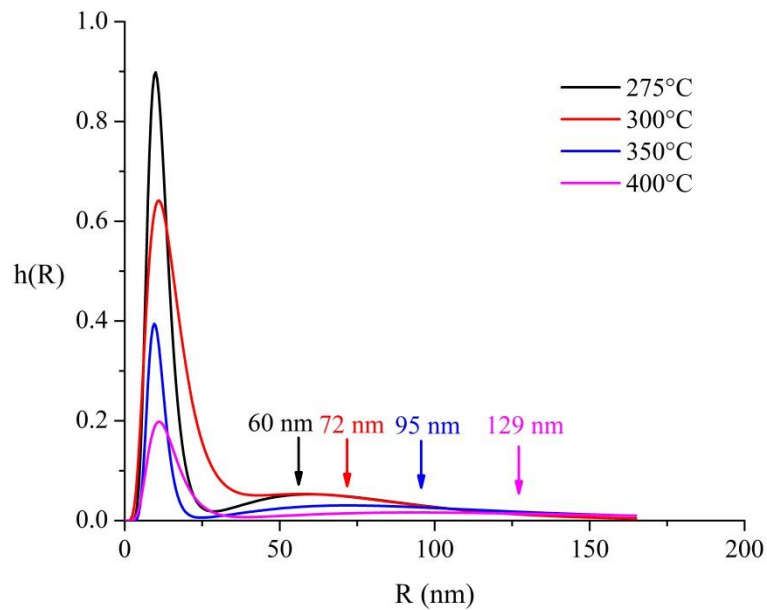


Figure 5.13 Particle size distribution functions of ADIs austempered at 275°C, 300°C, 350°C and 400°C. The average particle sizes of large particles in ADIs have been shown in the same colours of their corresponding curves.

The size distribution functions of ADI austempered at 350°C and plastically deformed to different compressive strain levels are shown in Figure 5.14. The measuring range has been expanded for this experiment to 465 nm and the vast majority of particle size information is included. The effect of plastic deformation on the particle size distribution can be discussed in two parts. First, the proportion of small particles decreases as the deformation increases and their distribution range widens. Second, the average size of large particles increases as the deformation increases, while the particle size distribution becomes gradually more uniform during plastic deformation (Fig. 5.14c).

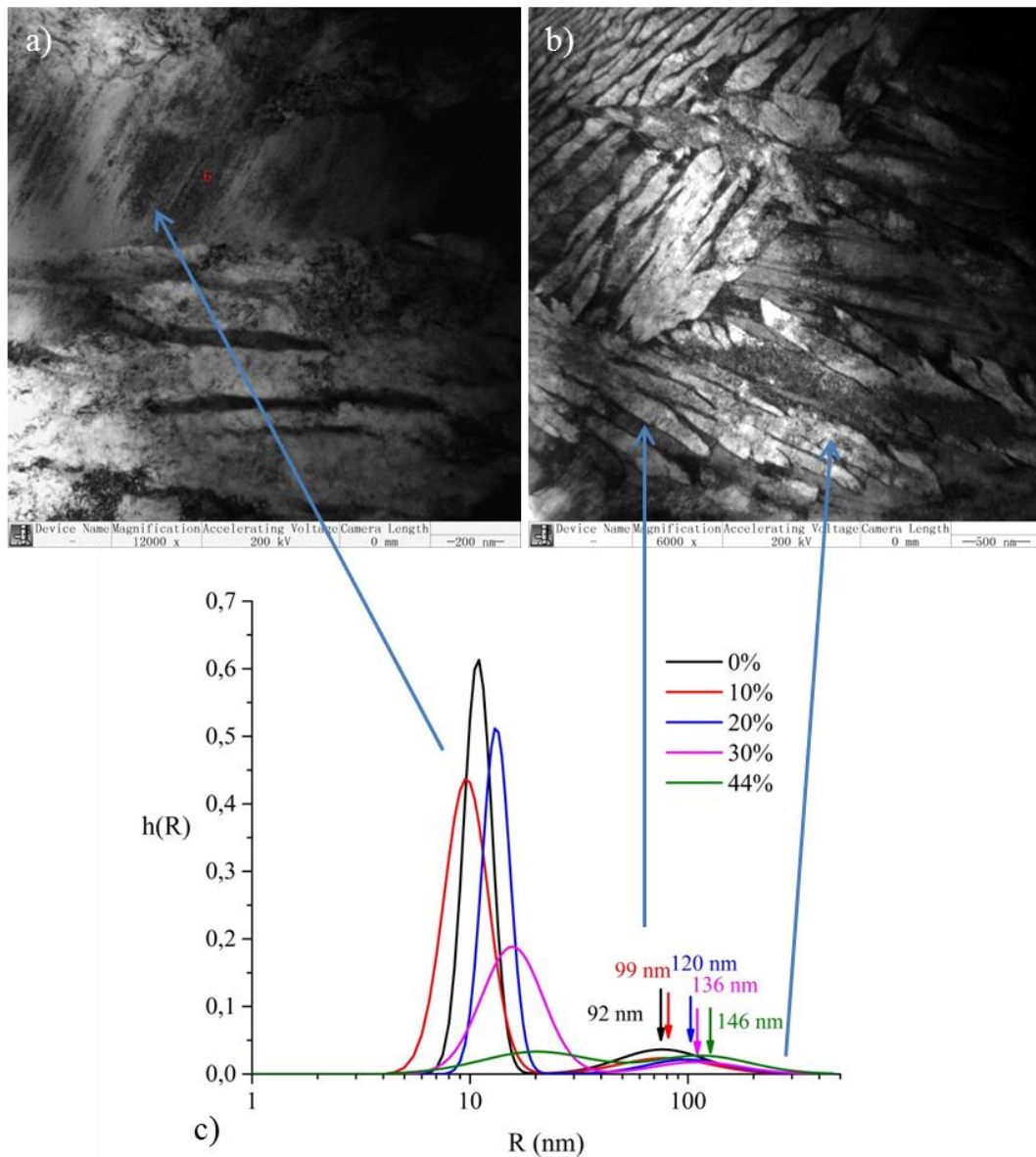


Figure 5.14 a) TEM micrograph (bright field) of ADI (austempered at 350°C for 30min and compressed to 42% strain level), showing the twin structure of martensite.
 b) TEM micrograph of the same sample with lower resolution showing the larger grains of austenite and ferrite.
 c) Particle size distribution functions of ADIs austempered at 350°C and plastic deformed to 10%, 20%, 30% und 44%. The x-axis (particle size) was converted to logarithmic form for a better overview.

The probability of carbide and carbon cluster splitting into smaller particles during the plastic deformation is quite small. So the change in the small particle region is likely been caused by the formation of sizeable numbers of martensite grains (Fig. 5.14, subgrains and twin structures in austenite). The diameter of the martensite grains is slightly larger than carbides, therefore the average size of small particles also increases with increasing

deformation (Fig. 5.14 c). A similar change also occurred in the large particle region. Some large particles (mainly ferrite grains, larger than 465 nm and therefore out of measuring range) are split into several grains within the measuring range, increasing the overall fraction of large particles and reducing the fraction of small particles. Although this change has not been observed in SEM or TEM directly, it can be reasonable speculated from the increasing average size of large particles and slight rise of the distribution function of large particle region (Fig. 5.14 c).

5.3 Phase analysis and carbon content in unstrained ADI

5.3.1 Phase fraction of austenite and ferrite in ADI after heat treatment

The results of the quantitative phase analysis on the unstrained ADI samples using neutron diffraction (section 4.10) and synchrotron diffraction (section 4.5), are shown in table 5.2.

Table 5.2 Austenite and ferrite phase fraction in ADI (with 3 different nickel content, austenitized at 900 °C and austempered at 5 different temperatures) after Rietveld-refinement using Maud (error bars are from standard deviation of the Rietveld refinement).

Austempering Temperature [°C]	250		300		350	
	Austenite	Ferrite	Austenite	Ferrite	Austenite	Ferrite
0 wt% Ni	15.1(2)	84.9(1)	22.4(1)	77.6(2)	33.5(2)	66.5(2)
0.5 wt% Ni	×	×	22.1(1)	77.9(2)	35.8(2)	64.2(2)
1.5 wt% Ni	×	×	25.9(1)	74.1(2)	39.6(2)	60.4(2)

Austempering Temperature [°C]	400		450	
	Austenite	Ferrite	Austenite	Ferrite
0 wt% Ni	40.2(2)	59.8(2)	45.0(2)	55.0(1)
0.5 wt% Ni	46.1(2)	53.9(2)	×	×
1.5 wt% Ni	47.2(2)	52.8(2)	×	×

5.3.2 Carbon diffusion during heat treatment

In the previous in-situ neutron diffraction study a systematic investigation on the carbon content changes in austenite and ferrite during austempering was carried out [Leop15]. However, in this study the neutron diffraction data suffered from some limitations like the relatively coarse time resolution $t \geq 20$ s, the small 2θ scattering angle coverage restricting the phase analysis to just three Bragg reflections [Leop15, Lmei13] and the relative large incremental peak resolution compared to synchrotron diffraction. Hence the peak position of a crystallographic phase could only be determined accurately in this investigation when the volume fraction of the phase exceeded over 2%. Therefore in the in-situ neutron diffraction study on the austempering process [Leop15, Lmei13], at the beginning of austempering - e.g. the first 2 ~ 5 mins depending on austempering temperature -, no information on the developing ferrite phase has been obtained. In order to compensate the lack of information on the ferrite phase in this time period, in-situ synchrotron diffraction has been performed to close this time gap.

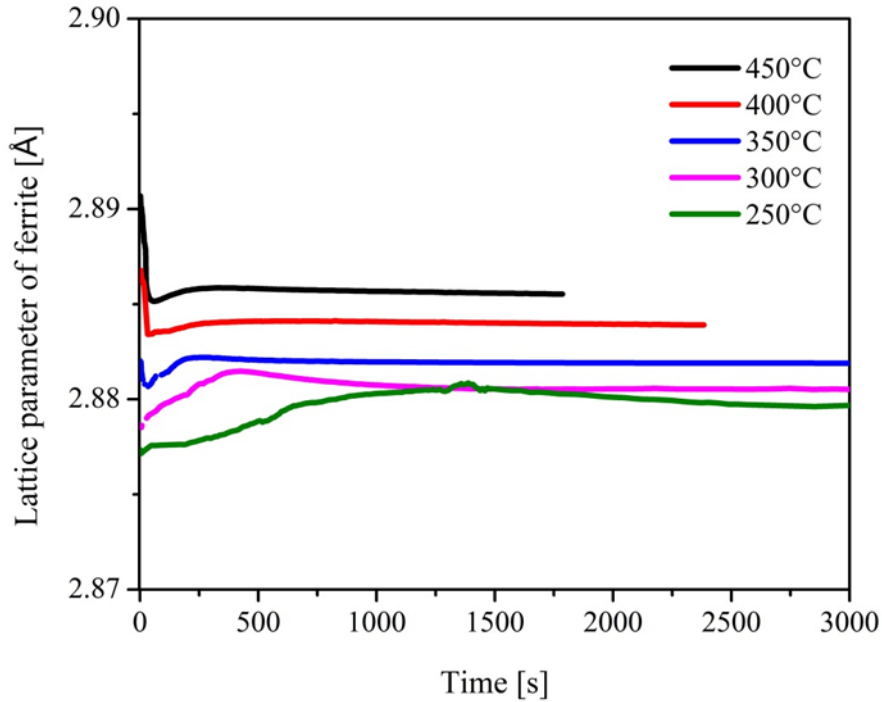


Figure 5.15 Lattice parameter change of ferrite in ADI during quenching and austempering at different austempering temperatures.

Figure 5.15 shows the evolution of ferrite lattice constant derived from single peak fitting of the ferrite (110) reflection of the synchrotron diffraction pattern (section 4.5) during quenching and austempering as a function of time. In all following Figures of this sub chapter the time $t = 0$ is set when the sample temperature reaches the austempering temperature (Fig. 4.1).

After quenching and austempering, the lattice parameter of ferrite eventually reaches a constant value after a period of some fluctuations. The fluctuations are caused by the temperature changes during quenching ($t < 0$) and carbon diffusion during austempering ($t > 0$). Assuming that the lattice changes in ferrite during austempering are solely from carbon diffusion and in order to visualize the carbon content changes in ferrite and exclude the interference of temperature and alloying element silicon using equation (5.7), the lattice parameter of ferrite has been converted to carbon content using equation (5.7) and 5.8 [Leop15] with the resulting graph shown in Figures 5.16 and 5.17. The parameter $a_{\alpha}^{Ref}(T)$ in equation (5.1) is the thermal expansion of ferrite in ADI with 0.0 wt% carbon and corresponds to a_{α}^0 in equation (5.8). The carbon content in ferrite during quenching and austempering has been shown in Figure 5.16 and 5.17 as a function of time.

$$a_{\alpha}^{Ref}(T) = a_{\alpha,RT}^{Ref} \cdot (1 + \alpha_{\alpha}^l \cdot T + \alpha_{\alpha}^q \cdot T^2) + a_{Si}^l \quad (5.7)$$

$a_{\alpha}^{Ref}(T)$: Lattice parameter of ferrite at temperature T [Å]

$a_{\alpha,RT}^{Ref}$: Lattice parameter of ferrite at room temperature (20°C) [Å], 2.8663 Å

α_{α}^l : Linear coefficient of thermal expansion, $1.294 \cdot 10^{-5} \text{ K}^{-1}$

α_{α}^q : Square thermal expansion coefficient, $2.729 \cdot 10^{-9} \text{ K}^{-2}$

T : Temperature difference to room temperature [K]

a_{Si}^l : Lattice expansion of ferrite by silicon, 2.5 wt% Si in ADI leads to -0.003Å expansion.

$$a_{\alpha}^c = a_{\alpha}^0 + k_{\alpha}^c \cdot x_{\alpha}^c \quad (5.8)$$

a_{α}^c : Lattice parameter of ferrite

a_{α}^0 : Lattice parameter of ferrite by $x_{\alpha}^c = 0.0\%$ [Å]

k_{α}^c : Lattice expansion coefficient of ferrite caused by carbon atoms, 0.0385 Å/wt%

x_{α}^c : Carbon content in ferrite [wt%]

Using the high time resolution of the synchrotron measurements the austenite to ferrite transformation has been observed to start already during the quenching process which took less than 10 s. The ferrite (110) reflection has been first observed to appear at about 650°C ~ 700°C (Fig. 5.16 bottom), which is very close to the eutectoid reaction temperature (727 °C) in the Fe-C phase diagram for a carbon content of 0.76 wt%.

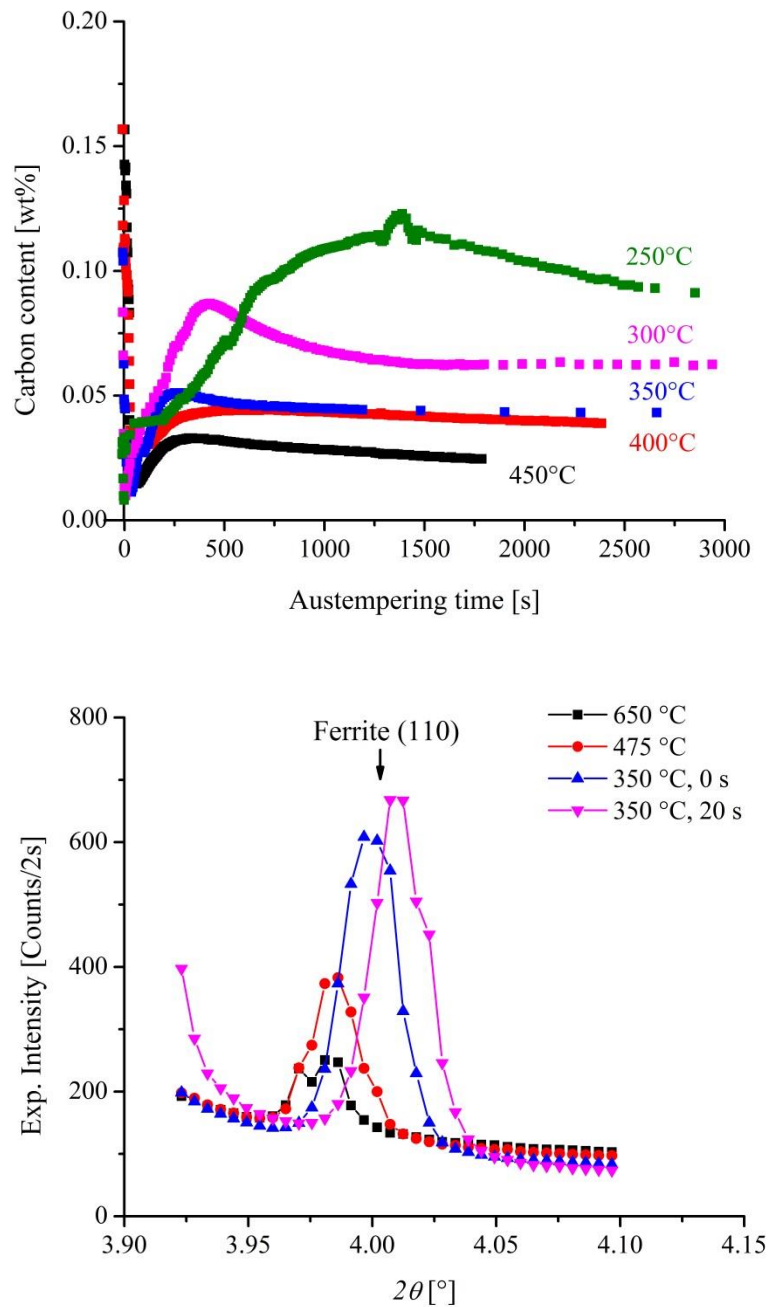


Figure 5.16 Top: Change of carbon content in ferrite during quenching and austempering. Bottom: Peak position change of ferrite (110) during quenching and austempering (350°C).

The lattice constant/carbon content in ferrite change in all ADI samples showing a decrease, increase and decrease again as a function of time (Fig. 5.16 top). To understand the reasons for this behaviour, two factors need to be considered: phase transformation rate and carbon diffusion rate. Taking the carbon content change in ferrite at 450 °C in Figure 5.17 as an

example, the carbon content change in ferrite has been divided into three stages with consideration of the phase transformation rate⁴.

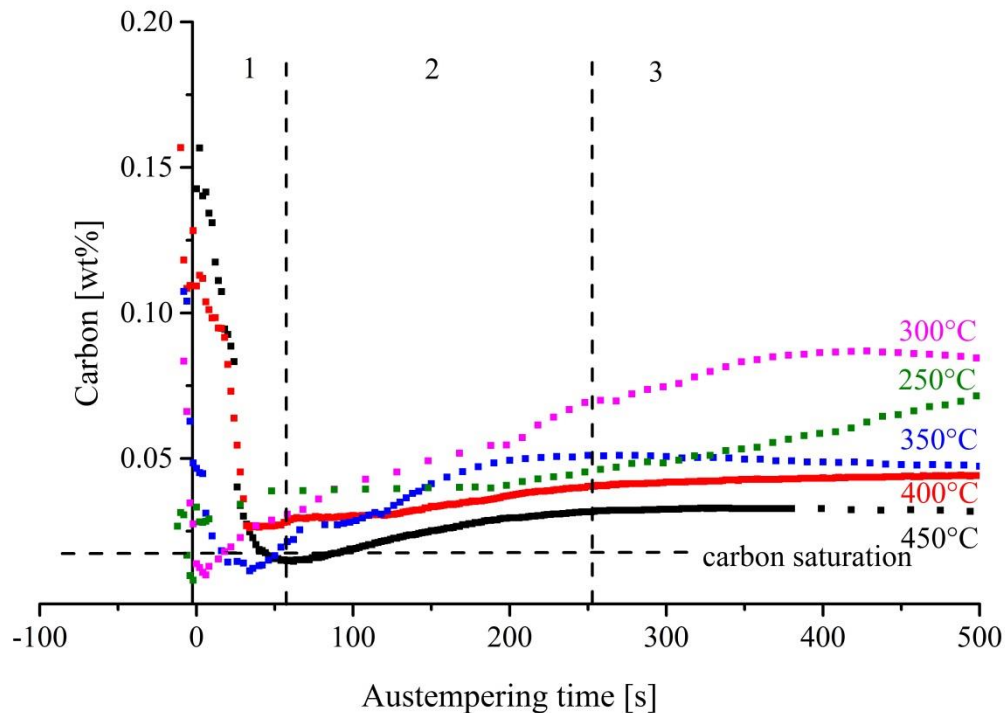


Figure 5.17 Enlarged view of Figure 5.16 in the first 500s of austempering. In the case of austempering at 450 °C as an example, carbon diffusion process has been divided into 3 stages with consideration on phase transformation rate (Fig. 5.15).

Stage 1 ($t < 60$ s): In the first stage of austempering, supersaturated ferrite grains nucleate on the austenite grain boundaries. Most of the carbon atoms already diffuse out of the ferrite grains (with 0.1~0.15 wt% carbon left in the ferrite phase (Fig. 5.17)). Although it is not possible to measure the diffusion coefficient of carbon in ferrite/austenite grains in ADI materials directly (grain size is too small), it is assumed from previously measured data (carbon diffusion coefficient in ferrite of other steels) [Eper12], the remaining carbon atoms only needs microseconds to diffuse out of ferrite grains around 200 ~ 500 nm (see for example micrographs in Fig. 5.5) large at this stage, so that the carbon content in adjacent ferrite / austenite can reach constrained paraequilibrium [Jspe03]. In this stage, the rate with which the carbon content decreases becomes slower for increasing austempering temperatures. At 250 °C, the carbon content decrease is almost invisible; and carbon content has already reached the minimum during ferrite nucleation. This is surprising as the relationship between

⁴ In-situ neutron diffraction can only capture part of the information at the end of 2nd stage and the information of 3rd stage [Leop15, Psaa16].

temperature and carbon diffusion in this stage is inconsistent with basic thermodynamic principles. Therefore, the phase transformation rate and transformation mechanism need to be taken into account as two other influence factors. The phase transformation rates during austempering are shown for all temperatures T_{Aus} in Figure 5.18.

The phase transformation occurs at the grain boundaries of austenite and continues to expand toward the center of the grains [Wgon13, Leop15]. The continuation of the phase transformation is due to the nucleation of new ferrite grains at the interface of austenite/ferrite, rather than the growth of already existing grains. At the beginning of austempering, the volume fraction of ferrite and the phase transformation rate are proportional to the austempering temperature (Fig. 5.18). It indicates that a larger amount of new supersaturated ferrite grains nucleate at higher temperature than at lower temperature. In contrast, almost no carbon supersaturation in ferrite nucleation was found at lower austempering temperature, for example at 250 °C (Fig. 5.17).

Stage 2 (60 s < t < 20 min): Depending on the austempering temperature, the 2nd stage lasts about 3 min (450°C) to 20 min (250°C). In this stage, the ferrite (110) reflection can be observed also in the in-situ neutron diffraction pattern [Leop15, Psaa16]. However, the small volume fraction of ferrite and the large FWHM of ferrite (110) reflection in the neutron diffraction pattern make the accurate calculation of carbon content in ferrite cumbersome. The phase transformation rate and time diagrams in the previous works [Leop15, Psaa16] indicate, that the phase transformation rate reaches its maximum in this stage. This in turn implies that more supersaturated ferrite is formed during this stage and the overall average carbon content of ferrite is increasing again.

Stage 3: As the phase transformation rate continues to decline [Psaa16], the average carbon content in ferrite also decreases until it reaches a constant value. However, due to the continuous increase in the carbon content of austenite during this stage, the difference between chemical potential of carbon in austenite and ferrite decreases, so that a constrained paraequilibrium of the carbon content in austenite and ferrite similar to quench and partitioning (Q&P) steels cannot be achieved [Jspe03, Jgsp05]. Hence the carbon content in ferrite is always maintained in supersaturated state for austempering temperatures $T_{Aus} < 400$ °C.

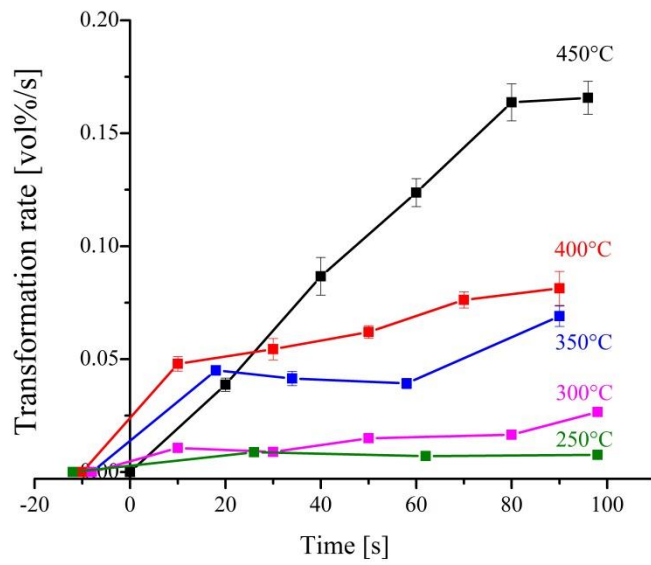
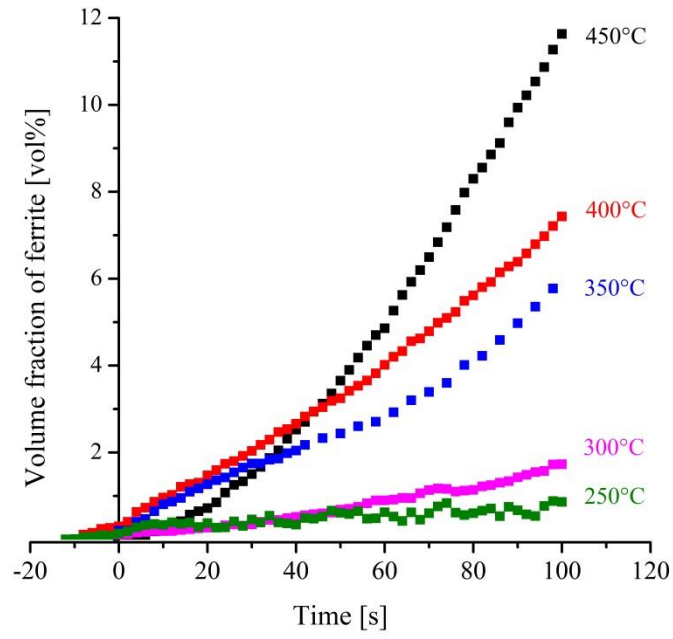


Figure 5.18 (top) Volume fraction of ferrite at the beginning of austempering.
 (bottom) Austenite to ferrite phase transformation rate at the beginning of austempering.

5.4 Atom-Probe-Tomography

5.4.1 Carbon content in austenite and ferrite

APT measurements were carried out on three different austempered (300°C, 375°C and 425°C) ADI samples to investigate the carbon distribution in the austenite and ferrite. These austempering times were selected based on earlier work to identify the factors that affect the carbon distribution [Leop15, Lmei13, Psaa16]. In the earlier work it was found that a sizeable fraction of carbon dissolved during austenitization is not redistributed into the retained austenite during austempering leading to the so called carbon gap [Leop15]. This carbon gap is largest in samples austempered at low temperatures and has a minimum at around 375°C. At higher austempering temperatures of $T_{Aus} > 400^\circ\text{C}$ already the stage 3 reaction in the ADI phase transformation sets in (cf. chapter 1.1) and carbides are formed increasing the carbon gap again.

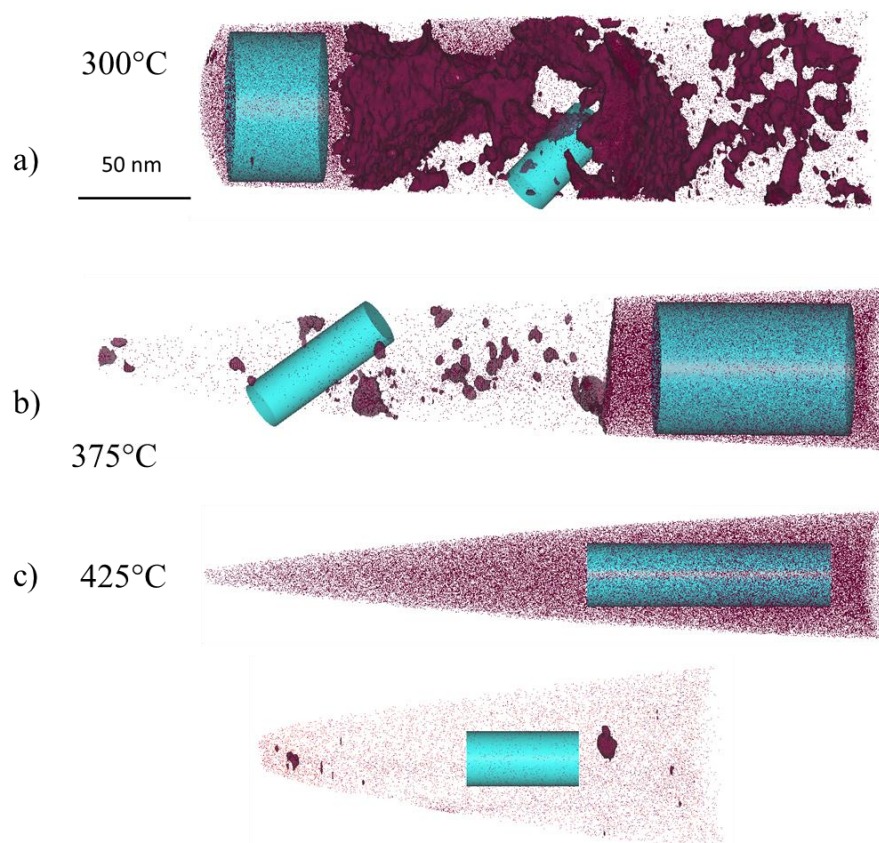


Figure 5.19 APT maps of carbon atoms in ADI. Red spots: carbon atom. Cyan cylinder: the area selected to calculate the averaged carbon content. a) ADI austempered at 300°C for 60 min. b) ADI austempered at 375°C for 43 min. c) ADI austempered at 425°C for 13 min.

Figure 5.19 shows the APT representation of carbon atoms in the three different austempered samples which allow direct albeit qualitative comparison. Austenite grains can

be identified through the distinctly higher density of carbon atoms. They show a uniform carbon distribution, while significant carbon segregation in ferrite was observed in all ADI materials. These carbon segregation regions decrease gradually as the austempering temperature increases. Quantitative results on the chemical compositions of the ADI samples were extracted in selected areas of the needles (blue cylinders) and are listed in 5.3. The distribution of silicon in the material has been observed to be almost uniformly distributed throughout the samples, independent on austempering temperature. The small differences of silicon in austenite and ferrite are caused by differences in carbon content (table 5.3).

Table 5.3 Averaged chemical composition (at%) in the sampling area of the APT measurements (e.g. cyan cylinder in Fig. 5.19)

Ion	ADI (300°C for 60min)		ADI (375°C for 43min)		ADI (425°C for 13min)	
	Austenite	Ferrite	Austenite	Ferrite	Austenite	Ferrite
Fe	88.60(2)	94.4(3)	88.355(9)	95.24(6)	89.728(8)	95.0(3)
C	6.377(7)	0.299(8)	7.269(4)	0.172(3)	5.463(3)	0.102(5)
Si	4.68(1)	5.1(3)	3.896(6)	4.19(7)	4.368(5)	4.6(3)
Mn, Cr, Al, O etc	0.343(8)	0.201(7)	0.480(4)	0.40(1)	0.441(3)	0.298(7)

For comparison the carbon content in ferrite as measured by synchrotron diffraction (section 5.3.2) and by APT (table 5.3) is shown in Figure 5.20. Although APT yields quite localized information on the chemical composition whereas synchrotron diffraction is a bulk method, still a good agreement between both methods can be observed. With both methods a direct relationship between carbon content and austempering temperature is found and can be approximated by a linear fitting (equation (5.9)) in the appropriate austempering temperature range (250 °C ~ 450 °C). From the graph one can conclude that throughout the standard austempering temperature range of ADI material, the ferrite is supersaturated with carbon with maximum carbon content at low austempering temperature.

$$x_C^{ferrite} = -0.0014 \cdot T_{Aus} + 0.7 \quad (5.9)$$

$x_C^{ferrite}$: Carbon content in ferrite [at%]

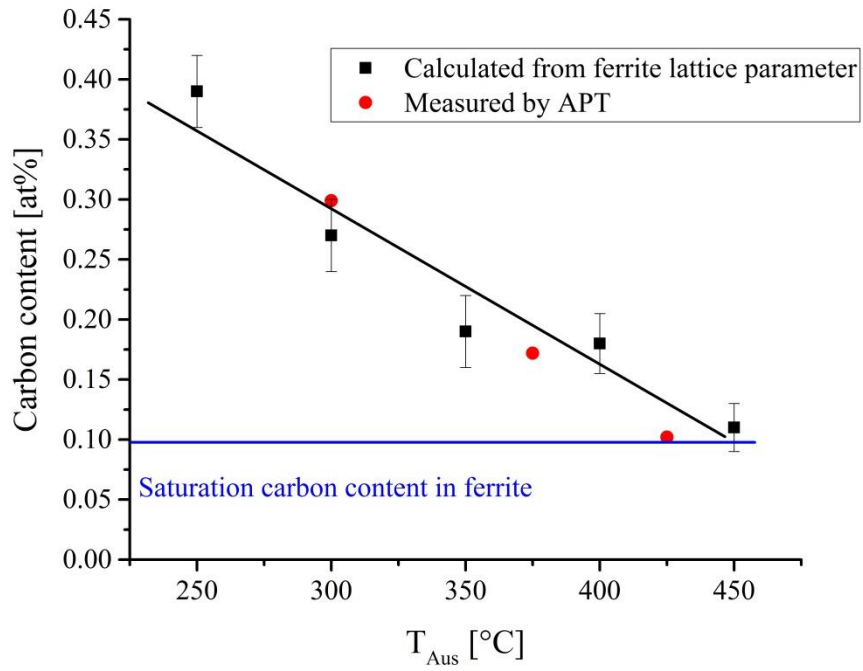
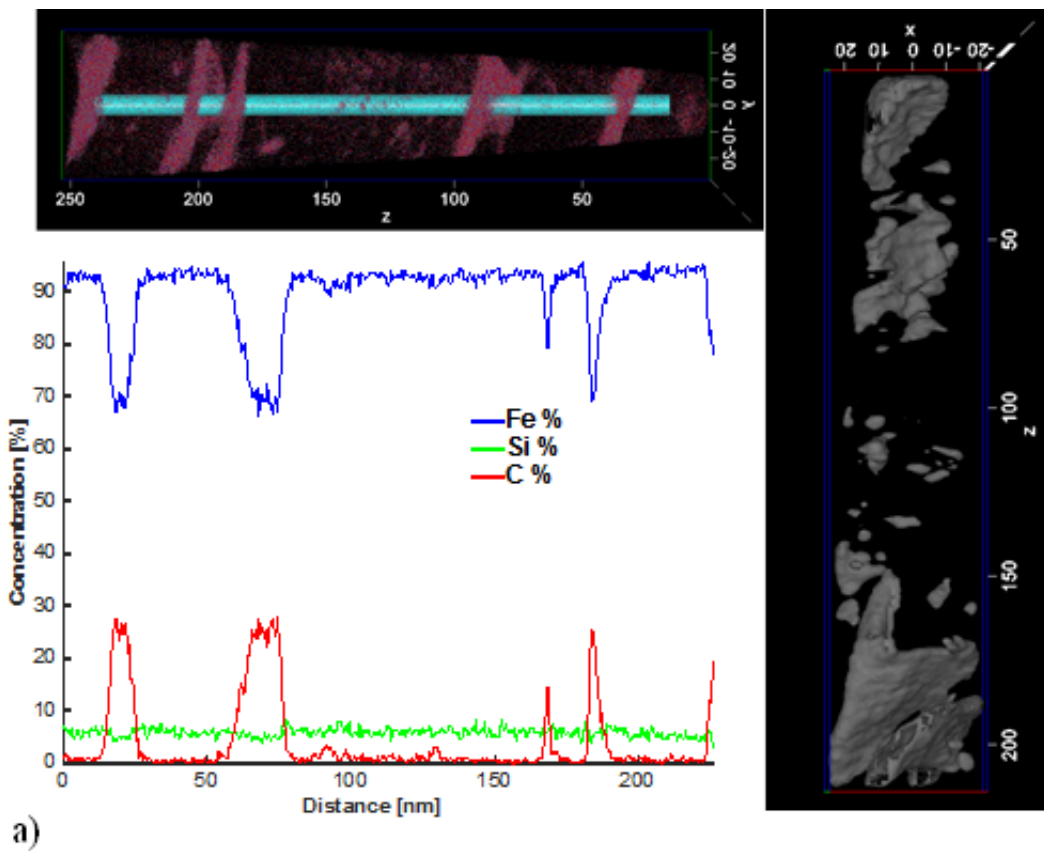


Figure 5.20 Carbon content [at%] of ferrite in ADI austempered at different temperatures. Black spots: calculated from fitting results of ferrite (110) peak using synchrotron diffraction pattern (Fig. 5.15). Red spots: measured by APT directly (table 5.3).



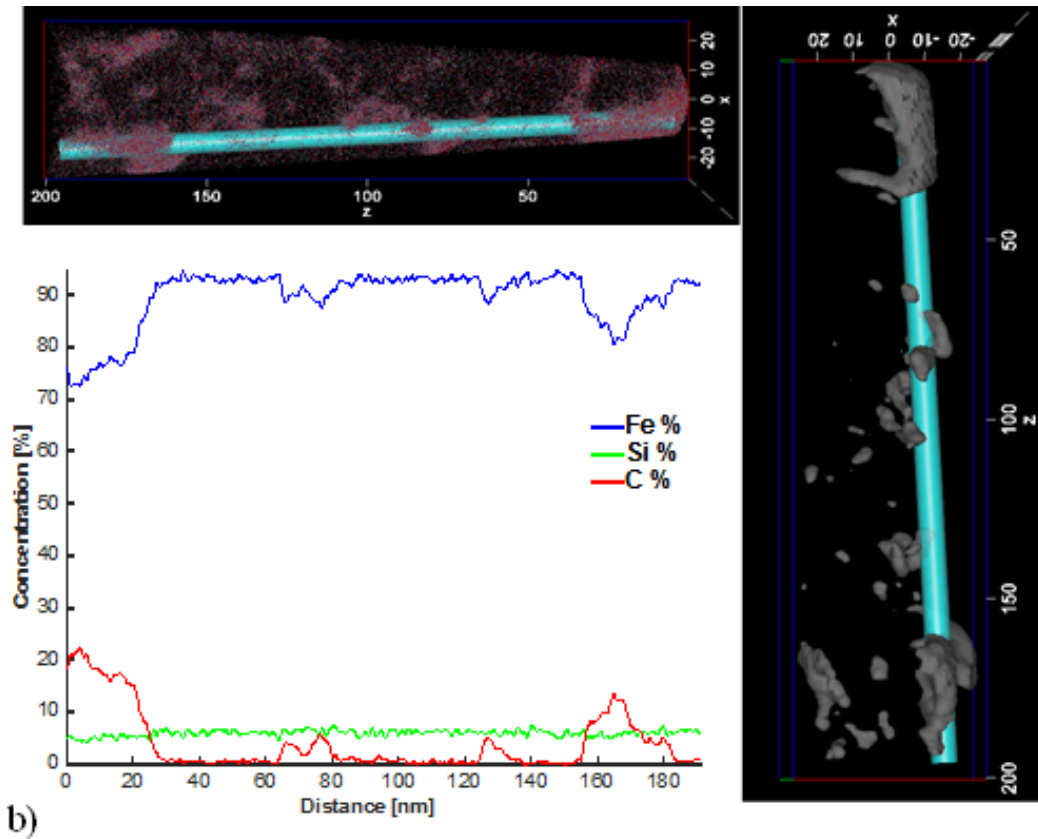


Figure 5.21 a) 3-D carbon atom map (top) of a ferrite grain and the corresponding 3-D particle form of the carbides in ADI austempered at 300°C for 60 min (right). The concentration profiles of Fe, Si and C in the selected cyan cylinder, which show a volume through the block/sheet-like carbon segregation area.

b) 3-D carbon atom map of a ferrite grain and the corresponding 3-D particle form of the carbides and carbon clusters in the same sample as a). The concentration profiles of Fe, Si and C in the selected cyan cylinder, which show a volume through the granular carbon segregation areas.

In the 3-D carbon atom mapping, the morphology of carbon segregation area was mainly divided into sheet-like or blocky carbon-enriched areas in the vicinity of the austenite/ferrite interface with a typical carbon content ≥ 20 at% (Fig. 5.19 a and 5.21 a) and sporadic small granular areas inside the ferrite grains having a carbon content between 5 ~ 15 at% (Fig. 5.21 b). Based on the proportions of the chemical elements in the carbon segregation area, the results of the SADP measurements (cf. Figure 5.6) and previous investigations in iron based materials [Awie11, Cmfa09] that undergo similar phase transformations, the phases existing in the sheet-like or block carbon segregation areas are identified most likely to be θ -Fe₃C and γ -Fe₂₃C₆. The ratio of carbon and iron in the small granular areas did not conform to any known carbide. Granular retained austenite (carbon content ≤ 8 at%) and carbon clusters (Carbon content 8 ~ 15 at%) are possible explanations to these areas [Dhsh07].

As APT is a very local probe, the content and morphology of carbide formed at different austempering temperatures cannot easily be compared to the bulk results from the diffraction experiments. However, it seems certain that the carbide formation in ferrite is always present through the entire austempering temperature range.

5.4.2 Carbon content at grain boundaries

In all the data sets of 3-D carbon atom mapping on the austenite/ferrite interface, a smooth rise in the carbon concentration profile has been observed at the interface of austenite/ferrite. The average carbon content at the austenite/ ferrite interface is 2.8 at%, less than that in austenite. No excess carbon atoms trapped at the interfaces have been observed in all investigated ADI materials, excluding the possible accumulation of carbon at grain boundaries.

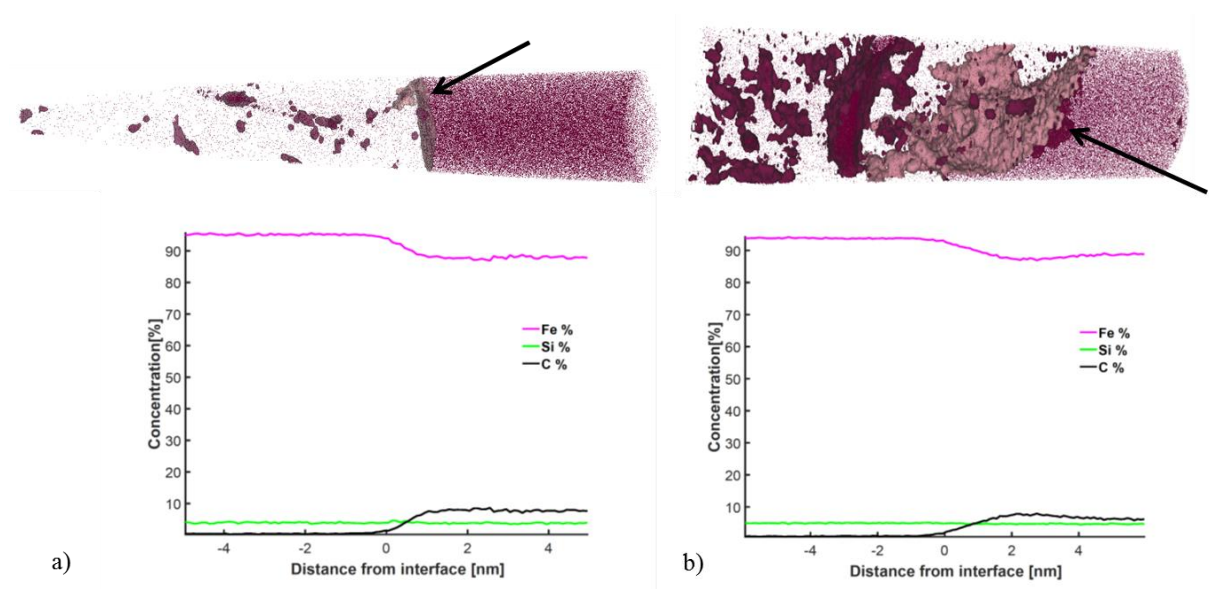


Figure 5.22 a) 3-D carbon atom map of an austenite/ferrite grain boundary in ADI austempered at 375°C for 43 min. Chemical composition vs distance from the marked interface.
b) 3-D carbon atom map of an austenite/ferrite grain boundary in ADI austempered at 300°C for 75 min. The arrows mark the grain boundary.

5.4.3 Carbon gap

The problem of the missing carbon or the carbon gap found in ADI materials [Leop15, pp. 158] can be elucidated by combination of the TEM, synchrotron diffraction and APT results. First, both synchrotron and neutron diffraction have shown that the initial carbon content in austenite is about 0.8 wt% (ω_C^{matrix}) after austenitization and at the beginning of austempering. The carbon gap (ω_{C-gap}) at different austempering temperatures has been

calculated by substituting the austenite phase fraction determined by neutron diffraction (table 5.2) and carbon content of austenite determined by synchrotron diffraction (Fig. 5.20) into equation (5.10) with corresponding results shown in Figure 5.23. The $\omega_C^{ferrite}$ in equation (5.11) has been calculated from the average carbon content of ferrite and ferrite phase fraction in Figure 5.20 and shown in Figure 5.23 simultaneously. About 9% to 12% of carbon atoms missing (carbon gap) are dissolved in the ferrite matrix forming supersaturated ferrite. The residual large amount of carbon atoms distributes in the form of carbides and carbon clusters in the ferrite grains.

$$\omega_{C-gap} = \omega_C^{matrix} - \omega_C^{austenite} \quad (5.10)$$

$$\omega_C^{carbide+carbon\ cluster} = \omega_{C-gap} - \omega_C^{ferrite} \quad (5.11)$$

ω_C^{matrix} : Measured carbon content in austenite matrix at 900°C [wt%], 0.8 wt%

ω_{C-gap} : Carbon gap in ADI [wt%]

$\omega_C^{austenite}$: Carbon content in austenite matrix [wt%]

$\omega_C^{carbide+carbon\ cluster}$: Carbon content in carbide and carbon cluster [wt%]

$\omega_C^{ferrite}$: Carbon content in ferrite matrix [wt%]

The carbon gap (Fig. 5.23) calculated using synchrotron diffraction are very close to the values calculated in the previous work using neutron diffraction [Leop15], which means both diffraction methods can be used to reveal the relationship between carbon gap and austempering temperature of ADI effectively and accurately. However, the lattice parameter of ferrite determined by synchrotron diffraction seems to be more accurate. This is most obvious from the lattice parameter evolution of ferrite in the end stage of austempering. In the end stage of austempering, both phase fraction and carbon content in austenite and ferrite have reached the plateau value, and the carbon content in ferrite measured by in-situ neutron diffraction has larger errors as that measured by synchrotron diffraction ([Leop15] and Figure 5.16). The linear relationship between carbon content in ferrite and austempering temperature (see Figure 5.20) has not been revealed by in-situ neutron diffraction, while in the carbon gap problem in the previous work [Leop15], the carbon content in ferrite was not taken into account. However, the fraction of carbon atoms dissolved in ferrite (9 ~ 12%, Figure 5.23) does not change the correlation between carbon gap and austempering temperature. Considering the location of carbon atoms contributing to the carbon gap, all the carbon atoms are present in the ferrite matrix with 10% dissolved in the ferrite matrix and 90% segregated

in as carbides and carbon cluster. Figure 5.23 also shows that the carbon content dissolved in ferrite matrix is continuously reduced as the austempering temperature increases, as the diffusion rate of carbon is increased with temperature thus enabling easier redistribution either into carbides or the austenite matrix.

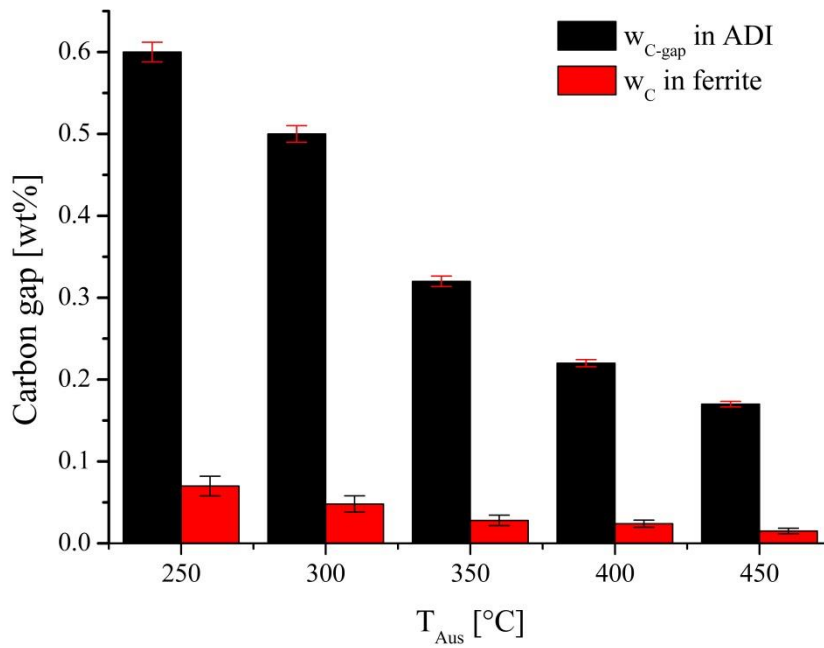


Figure 5.23 Comparison of carbon gap in ADI $w_{C\text{-gap}}$ austempered at different temperatures and the whole carbon content w_C in ferrite.

5.5 Martensite-Start Temperature

The results of the quantitative phase analysis of the quench tests (Fig. 4.1) showing the resulting martensite to initial austenite ratio against quenching temperature are illustrated in Figure 5.24. Using the Koistinen-Marburger relation (equation (5.12), [Dpko59]) the dependence of the ratio of resulting martensite fraction to initial austenite content on quenching and the corresponding M_s temperature can be calculated in steels. The parameter b is a material dependent parameter related to M_s and martensite finish (M_f) temperature and has been found originally to have a value of 0.011 in low carbon steels [Dpko59].

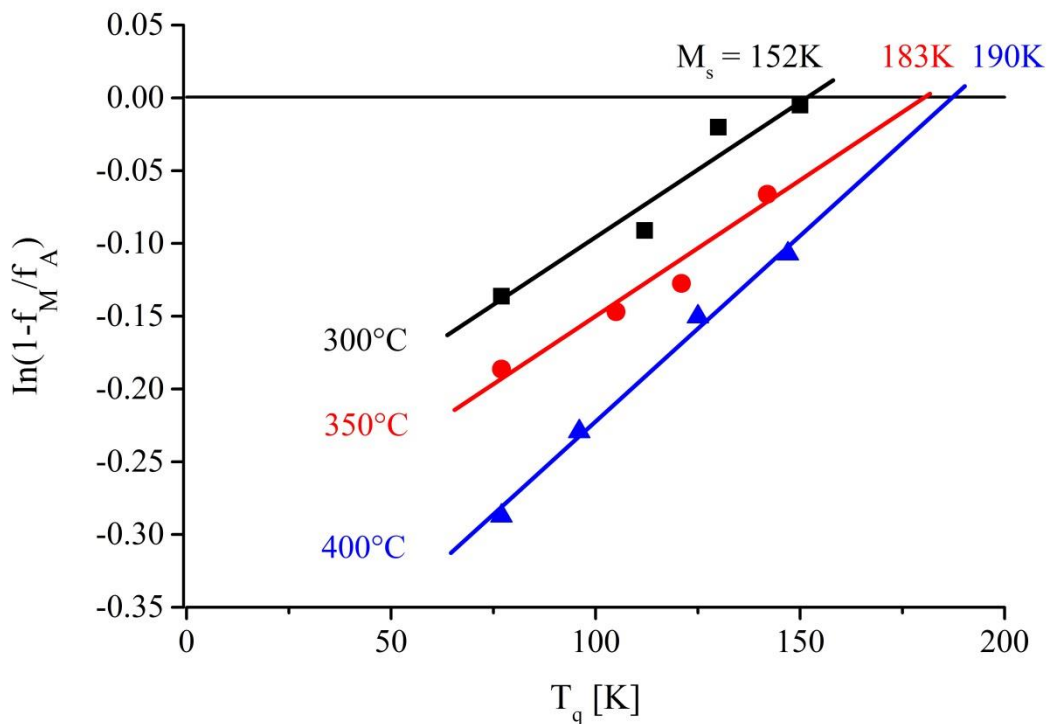


Figure 5.24 Resulting martensite volume fraction of ADI samples with 0 wt% Ni (austempered at 573 K (300 °C) , 623 K (350 °C) and 673 K (400 °C)) versus quenching temperature. The lines are fits using the K-M relation, with resulting M_s temperatures also shown at the intercept with the T axis. The resulting M_s of ADI samples with 0.5 wt% and 1.5 wt% Ni are shown in Figure 8.1.

$$\ln(1 - f_M/f_A) = b \times (T_q - M_s) \quad (5.12)$$

f_M : volume fraction of martensite.

f_A : initial volume fraction of retained austenite after heat treatment.

T_q : quenching temperature.

b : parameter related to M_s and M_f (martensite-finish temperature).

The b parameter can be derived from the slope of the fits in Figure 5.24 ranging from 1.7×10^{-3} to 2.7×10^{-3} . The M_s temperature is then determined as the intersection with the temperature axis.

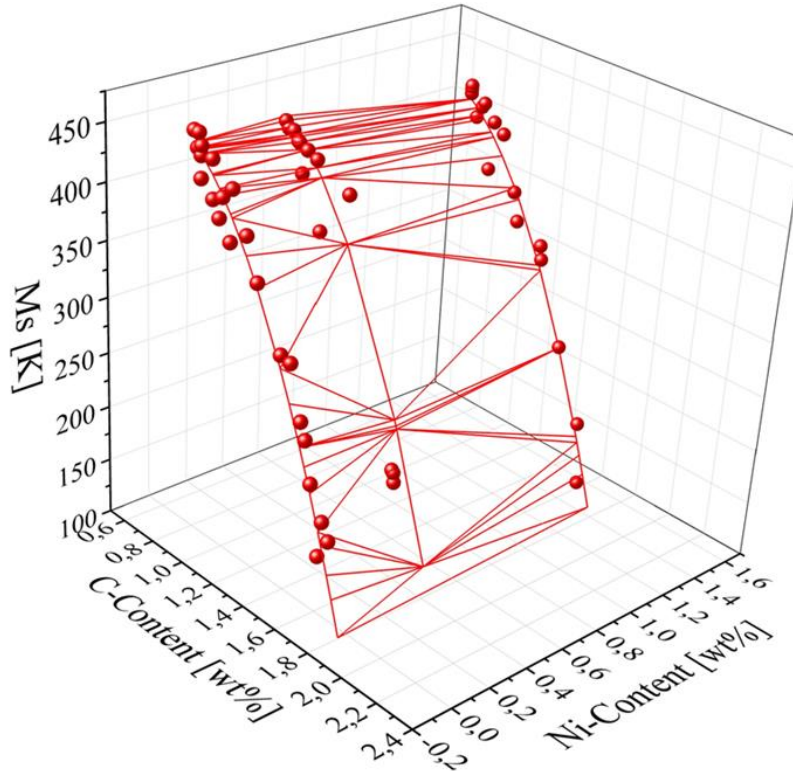


Figure 5.25 Determination of the alloying element influence (C and Ni) on the ADI M_s temperature. Symbols: measured M_s temperatures. Connecting lines: The M_s -plane as expressed in equation (5.13).

Figure 5.25 combines the results of measurements to determine the M_s temperature using dilatometry (high temperature) and neutron diffraction (low temperature) as a function of carbon and Ni content. A strong negative and non-linear dependence of the M_s temperature on increasing the carbon content can be observed. This reduction in M_s temperature is related to the increase in necessary strain energy to activate the displaced transformation from carbon enriched austenite to martensite. On the other hand alloying with Ni, which was added as a further austenite stabilizer, shows only weak tendency to decrease the M_s temperature in the measured ADI samples.

In steels mostly empirical models have been proposed to describe the influence of the chemical composition on the martensite start temperature M_s [Esro46, Wste56, Kwan65, Asto12]. The equations proposed by Steven [Wste56] and Andrews [Kwan65] are the most widely used in this respect. In general M_s was found to have a linear dependence on the

carbon content in the range from 0.1 wt% to 0.6 wt%. However, in high carbon alloyed steels, this linear relationship is no more adequate and polynomial functions were developed instead to calculate the dependence of the M_s temperature on carbon content. The M_s temperature and carbon content in ADI seems to have a similar parabolic relationship (Fig. 5.25). Therefore a polynomial fit in the form of equation (5.13) was performed on the measured M_s temperature data to approximate the evolution of the M_s temperature as a function of carbon and nickel content.

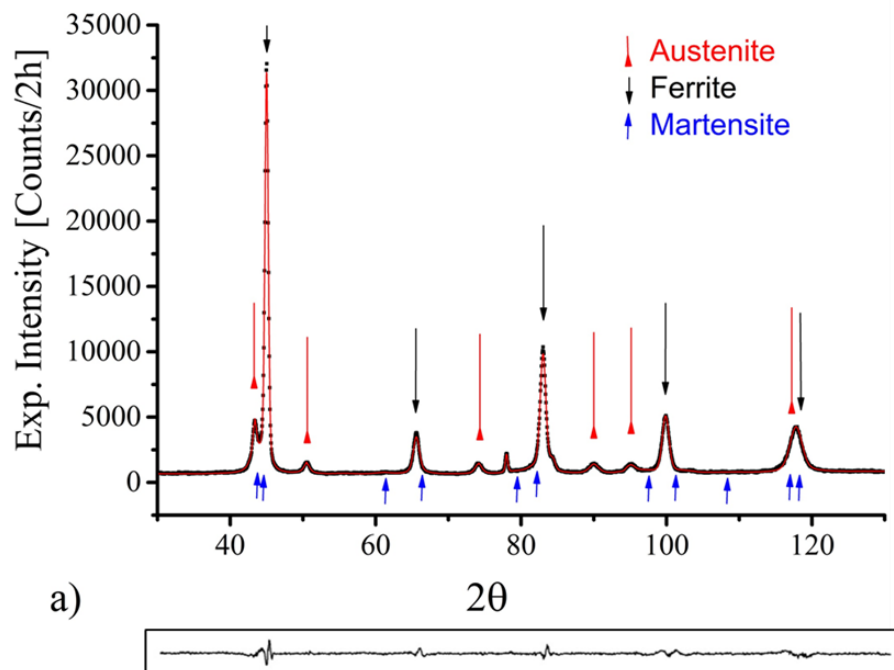
$$M_s = 384.5 - 254.9 \times C^2[\text{wt}\%] + 278.5 \times C[\text{wt}\%] - 19.4 \times Ni[\text{wt}\%] \quad [K] \quad (5.13)$$

Using this empirical equation with the known relationship of carbon content on austempering temperature and time [Lmei13], the M_s temperatures of all prepared deformation ADI samples in section 4.4 were calculated and are listed in table 5.4 (section 5.8).

5.6 Texture analysis

5.6.1 Pole figures and ODFs of compressed and cold rolled ADI

Figure 5.26 a) shows high resolution diffraction data of a sample which was prepared with the heat treatment parameters $T_\gamma = 1173$ K (900 °C) / $T_{Aus} = 623$ K (350 °C) and then compressed to strain levels of 40%. During plastic deformation the carbon enriched retained austenite partly transforms to martensite. Due to the very similar lattice parameters of ferrite and martensite and peak broadening effects, martensite and ferrite reflections strongly overlap in the neutron diffraction patterns. Thus, the strain induced martensitic transformation can best be seen in the diffraction data by a decrease of the austenite peak intensity and an increase of the ferrite peak intensity. Martensite reflections can be identified as shoulders close to the ferrite peak positions (Fig. 5.26 b)). However, the extensive peak broadening and overlap of austenite (111), ferrite (110) and martensite (101), (110) reflections make a direct extraction of individual martensite peak intensities difficult using ordinary peak fitting methods and also renders it impossible to extract the ferrite (110) pole figure. Therefore, a single reflection pole figure - e.g. from the (200) peak - for the ferrite ODF calculation was used as a way to overcome the peak overlapping problem.



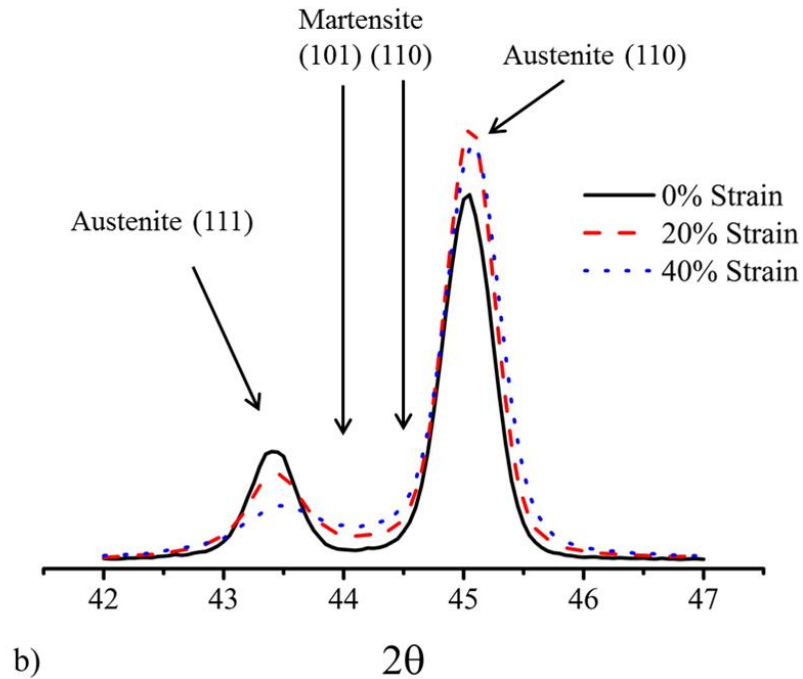


Figure 5.26 a) Neutron diffraction pattern and Rietveld refinement results of ADI sample, austempered at 623 K (350 °C) and deformed to 40% strain. The symbols correspond to the experimental data, the line describes the calculated diffraction pattern (Rietveld refinement) based on all phases. The peak positions of each phase are indicated by arrows. Peak positions of graphite are not shown in the Figure. The line at the bottom describes the difference between calculated and experimental data. b) An enlarged view of the diffraction pattern between $2\theta = 42^\circ \sim 47^\circ$ for three different strain levels during compression.

The ODFs and inverse pole figures of austenite and ferrite in ADI after compression and cold rolling are shown in Figure 5.27. Comparing the calculated ODFs (Fig. 5.27) with the theoretical predictions of Figure 3.12, the texture formation of austenite and ferrite in ADI during the plastic deformation (tension, compression and cold rolling) can be summarized as follows:

- (1) In tensile deformation no obvious texture changes were found; most likely due to the limited sample elongation (3~9%) achievable in the tensile experiments.
- (2) The strongest components of austenite phase in the compressed samples are α -fiber // LD plus (111) $[0\bar{1}1]$ and (001) $[\bar{1}\bar{1}0]$, and the component in cold rolled samples is a (110) $[001]$ Goss component [Mdah89].
- (3) In ferrite the compressive deformation leads to the formation of a texture characterized by two distinct components: (110) $[1\bar{1}2]$ Brass and (112) $[11\bar{1}]$ Copper, and the cold rolling deformation leads to a complete γ -fiber texture // ND.

strain hardening in some *fcc* metals [Abha05, Rjas85, Drit02, Srbo94]. However, in *bcc* metals, the strain rate was observed to have only a rather limited effect on the texture development [Hyuu97].

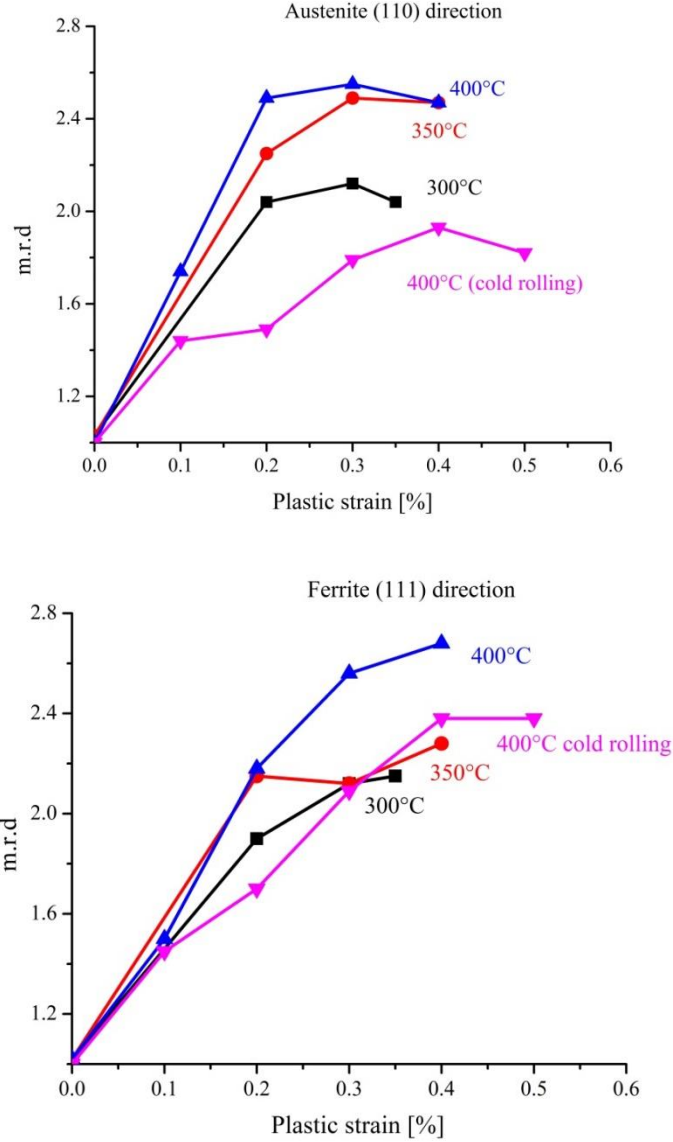


Figure 5.28 Texture evolution of compressed ADI samples austempered at 573 K (300 °C), 623 K (350 °C) and 673 K (400 °C) and cold rolled samples austempered at 673 K (400 °C). The multiple random distribution (m.r.d) of austenite 110 direction (top) and ferrite 111 direction (bottom), are plotted against plastic strain.

Figure 5.28 shows also a strong increase in texture sharpness during compression deformation until about 20% total strain and during cold rolling until about 30% total strain in *fcc* austenite after which almost no texture change is observed. This might be attributed to the increased number of strain induced martensite grains inside the austenite matrix, which inhibit

possible dislocation gliding (and consequently further texture development). In contrast, the texture formation in the *bcc* ferrite phase increases almost continuously with plastic strain.

5.7 Phase analysis in deformed ADI

5.7.1 Deformation behavior of ADI

The strain hardening behavior of the ADI samples during compressive deformation was analyzed using a model developed by Crussard and Jaoul ([Chcr50], equation (5.14)) based on an empirical approach to describe the relationship between root-mean-square values of shear stress and incremental strain of metallic materials during the strain-hardening process [Hws52]. Crussard and Jaoul have developed this model with consideration of two different deformation mechanisms. This model has already been proven to be very effective in the study of strain hardening behavior of dual-phase and TWIP steel [Bkjh87, Zjia95 and Vcol09], in which more than one deformation mechanism was found. The true stress and strain during the compressive deformation as calculated from the data according to equation (5.14) is shown in Figure 5.29.

$$\ln\left(\frac{d\sigma}{d\varepsilon}\right) = (1 - m)\ln \sigma - \ln(Km) \quad (5.14)$$

σ : true stress

ε : true strain

m : strain hardening exponent

K : material constant

The analysis reveals that in the deformation behavior of ADI for all the samples that three distinct stages can be observed, which are marked by arrows in Figure 5.29. Due to the critical strain values (the split points of stage 1, 2 and 3), stage 2 and 3 in Figure 5.29 correspond to the two typical distinct low and high strain regions in dual-phase steel [Zjia95]. In contrast, the strain hardening exponent m of ADI in stage 2 has no fixed value like in dual-phase steels. This suggests that the hardening process of ADI cannot simply be described by two mechanisms as in dual-phase steel, but there are other factors that dominate the mechanism of its hardening process.

In stage 1, the curves of ADI samples austempered at three different temperatures are almost the same, which means the deformation mechanism of the samples at the beginning of plastic deformation is only due to the primary deformation of austenite and ferrite (e.g. dislocation formation in ferrite and austenite). The difference in stress experienced by the materials at 1% strain level is mainly caused by their different microstructures and phase compositions. The results in Figure 5.13 and table 5.2 confirmed that ADI samples austempered at higher temperature contains more austenite (Note: austenite has lower strength

as ferrite and martensite) and has on average larger grain size. Less strength of a phase implies dislocation formation is easier at the same stress condition and larger grain size leads to smaller grain boundary density. These characteristics determine that dislocations are more likely to occur in ADI austempered at higher temperature.

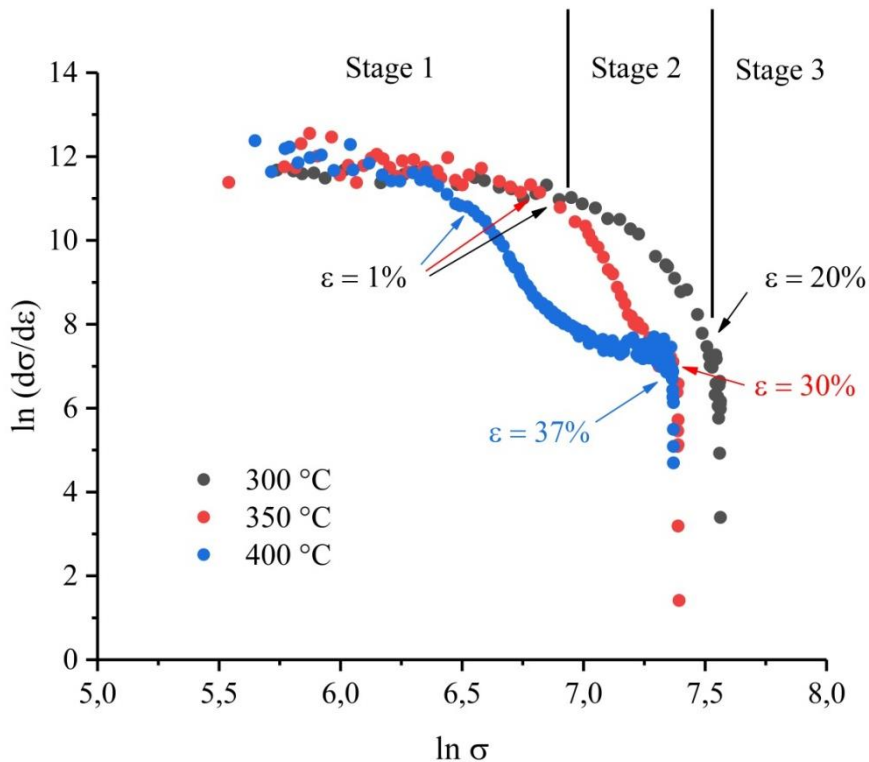


Figure 5.29 $\ln (d\sigma/d\varepsilon)$ vs. $\ln \sigma$ of ADI austempered at 300°C, 350°C and 400°C.

As the plastic strain increases more than 1%, all the curves enter the 2nd stage simultaneously, but with different m values (strain hardening exponent). Different m values indicate that the deformation mechanisms begin to be dominated by martensitic transformation as a new factor. The cut-off point at 1% plastic strain between stage 1 and 2 is most likely the starting point of martensitic transformation, as if only austenite and ferrite were present during the whole plastic deformation, the curves in ADI should be the more or less the same as in dual-phase steel, with similar m values. However, the martensitic transformation breaks the equilibrium conditions of a typical deformation process of a two phase system. The process of ferrite deformation through dislocation/twinning formation is relative stable and has been proved to have fixed m value ([Bkjh87, Zjia95 and Vcol09]), while austenite deformation and martensitic transformation are interrelated. The deformation mechanism in ADI is therefore dominated by 4 factors: austenite deformation, ferrite deformation, martensite deformation as well as martensitic transformation.

The martensite formation will prevent further formation of dislocations in austenite (section 5.6), while the martensitic transformation rate also varies with increasing plastic strain (Fig. 5.32) and together with different austenite/ferrite contents in the three ADI samples (table 5.2) results in the observable differences in the deformation curves of the samples.

In stage 3, the strain hardening rate drops rapidly until the failure of the samples, indicating that, due to the formation of large number of martensite grains - reaching over 50 vol%, comparing the critical plastic strain at the end of stage 2 in Figure 5.29 and the corresponding martensite phase fraction in Figure 5.32 - and high dislocation density in ferrite, the ADI material gradually loses good plastic deformation properties and becomes quickly brittle.

5.7.2 Phase analysis of tensioned, compressed and cold rolled ADI

Figure 5.30 and 5.31 show the martensite phase fractions in ADI after tensile, compressive and cold rolling deformation. The data were extracted from Rietveld refinements of the lattice constants, peak shape parameters and phase contents using the recalculated ODFs as additional input. The initial austenite and ferrite phase fractions in ADI after heat treatment are shown in table 5.2. The martensite phase fractions in the graphs are converted into vol% compared to the initial retained austenite content from table 5.2.

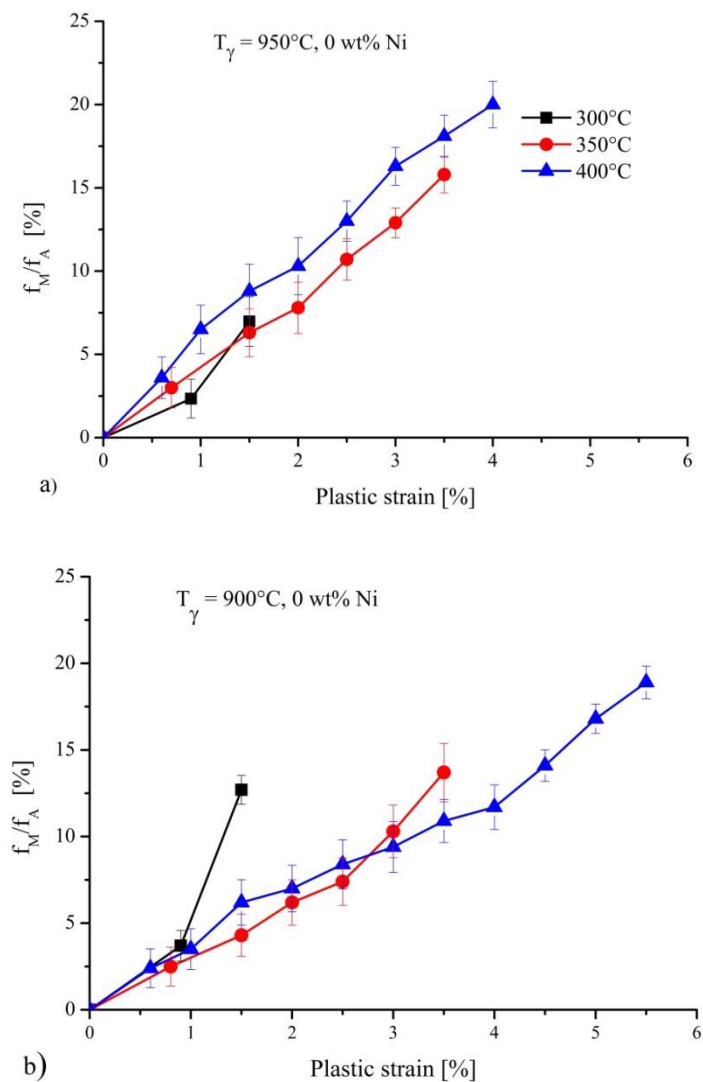


Figure 5.30 Fraction of martensite f_M/f_A after tensile deformation vs plastic strain in ADI containing no nickel and austenized at 950 °C (a) and 900 °C (b), respectively. The martensite phase fractions f_M/f_A are converted in % to the initial retained austenite content f_A .

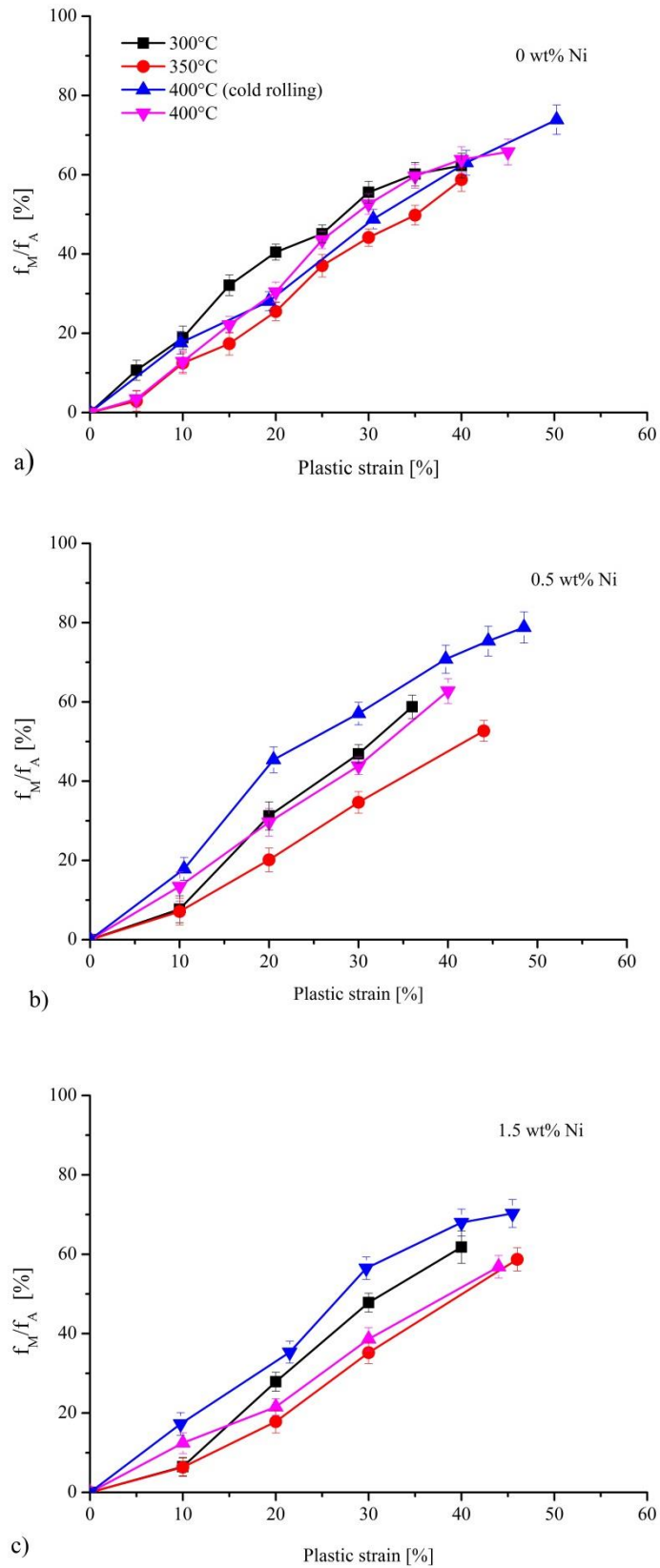


Figure 5.31 Fraction of martensite f_M after compression and cold rolling deformation vs plastic strain in ADI with 3 different Ni content. The martensite phase fractions f_M/f_A are converted in % to the initial retained austenite content f_A .

In our previous work [Psaal16] we have already determined that the alloy element nickel stabilizes austenite during the austenite-to-ferrite transformation. The phase analysis results in table 5.2 also show that higher nickel alloying results in higher retained austenite content after the heat treatment cycle is completed. Comparing the martensitic transformation curves in Figure 5.31 with the austenite phase fractions in table 5.2 one can see, that the strain induced martensite transformation in ADI during plastic deformation is not proportional to the initial retained austenite content. For instance in the ADIs exhibiting less retained austenite (austempered at 300 °C) the martensitic transformation proceeds faster and to a larger extent. The tensile experiments also illustrate that the strain induced martensitic transformation occurs simultaneously with plastic transformation. In the ADI samples between 12 to 20% (tensile deformation) and 60 to 80% (compressive and cold rolling deformation) of the retained austenite transforms into martensite at the respective maximal plastic deformation level. The stabilization effect of nickel on the austenite content during the strain induced martensitic transformation cannot be clearly observed in the curves of Figure 5.31. However, when considering the stabilization of retained austenite, the carbon content in retained austenite as another important austenite stabilizer also needs to be taken into account. On one side alloying with nickel will stabilize the retained austenite itself, but on the other hand it will inhibit the carbon saturation in retained austenite during austempering at higher temperature (350 °C and 400 °C) [Psaal16], which again escalates the probability of martensite transformation. As thermodynamic meaningful measure of austenite stability the M_s temperature can be used [Gnha96, Aita95]. Therefore the determined M_s temperatures (chapter 5.5) are used in the following to clarify the contrariety of these influences to the martensitic transformation and to determine the relationship of retained austenite stability and martensitic transformation kinetic quantitatively.

5.8 Simulation and development of martensitic transformation model

The simulation of strain induced martensitic transformations kinetic in ADI material is based on the model developed by Shin *et al* (equation (3.4)) [Hcsh01]. The results in section 5.7.2 (Fig. 5.30 and 5.31) were simulated using equation (3.4) to illustrate the relationship between martensite phase fraction and its related influence factors. Figure 5.32 shows exemplarily results of fitting the martensite fraction after compression deformation of ADI containing no nickel. The deformation mode parameter n was determined to have values in the range of 1.7 to 2 in compressive deformation while smaller values of 1.5 in cold rolling and ~ 1 in tensile deformation were found. Table 5.4 lists the fitting results for all sample compositions and heat treatment parameters.

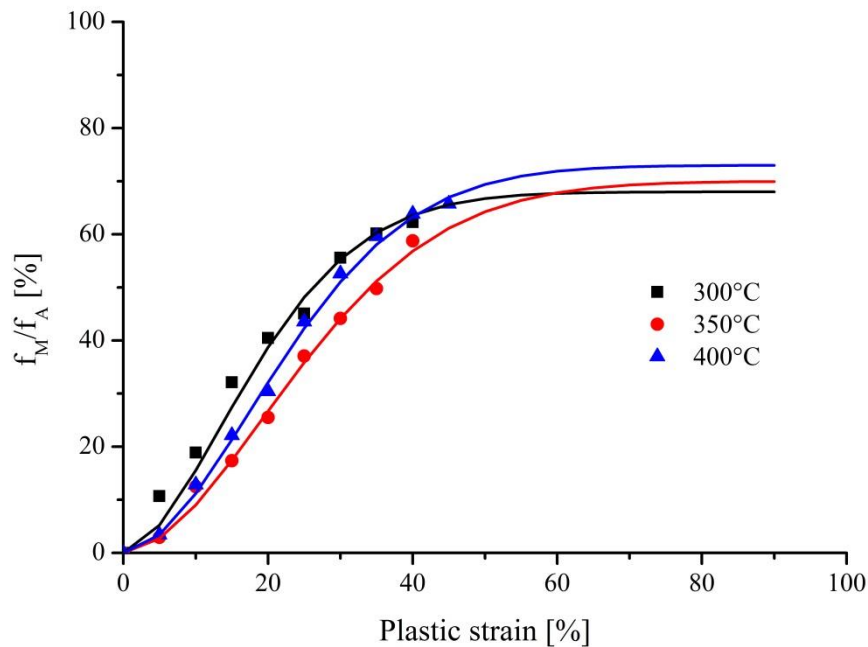


Figure 5.32 Martensite phase fraction after compressive deformation of ADI (0 wt% Ni) austempered at 300 °C, 350 °C and 400 °C, respectively. The lines are fits to the data using the model of Shin *et al* [Hcsh01] as described in the text.

The austenite stability β in equation (3.4) has been shown in [Hcsh01] to depend mainly on chemical composition and loading temperature. Alloying element content, grain size and internal stress state of austenite on the other hand have been all included as main parameters determining the M_s temperature. Using peak shape analysis of the neutron diffraction pattern it can be shown, that the variation in grain size and stress state of the retained austenite in differently heat treated ADI samples is negligible. Therefore the content of alloying elements remains as the main contributing factor to influence the M_s temperature in our ADI samples.

Table 5.4 M_s temperature of ADI samples in the tensile, compression and cold rolling experiments after calculation with equation (5.13) and the results of martensitic transformation kinetic using equation (5.14).

Ni content [wt%]	0.0						0.0	0.5	1.5
	950 (tension)			900 (tension)			900 (cold rolling)		
T_A [°C]									
T_{Aus} [°C]	300	350	400	300	350	400	400		
β	--	4.8(2)	4.5(2)	--	5.3(2)	6.5(2)	6.8(2)	7.0(3)	8.0(3)
n	--	1.0(1)	1.0(1)	--	1.0(1)	1.0(1)	1.4(1)	1.5(1)	1.5(1)
f_s	--	0.80(5)	0.80(5)	--	0.80(5)	0.80(5)	0.90(5)	0.88(3)	0.75(3)
M_s [K]	--	156(5)	134(5)	--	149(5)	177(5)	185(5)	199(5)	202(5)

Ni content [wt%]	0.0			0.5			1.5		
	900 (compression)								
T_A [°C]									
T_{Aus} [°C]	300	350	400	300	350	400	300	350	400
β	15.0(3)	5.5(3)	8.8(3)	13.0(5)	4.5(3)	8.5(3)	11.0(3)	5.0(3)	7.2(2)
n	1.7(1)	1.6(1)	1.7(1)	2.0(1)	1.7(1)	1.7(1)	2.0(1)	1.8(1)	1.8(1)
f_s	0.65(5)	0.80(5)	0.75(5)	0.70(5)	0.80(5)	0.72(3)	0.75(5)	0.80(5)	0.70(5)
M_s [K]	219(5)	139(5)	172(5)	204(5)	127(5)	189(5)	190(5)	143(5)	175(5)

Plotting the extracted austenite stability parameter β against the martensite start temperature for all samples reveals a linear relationship depending on the deformation mode (Fig. 5.33). The more stable the austenite is, the smaller the β value will be; and β will tend towards 0 at the martensite upper limit temperature (M_d), at which the internal strain energy caused by plastic deformation is not sufficient for strain induced martensitic transformation. After linear fit this relationship can be expressed as:

$$\begin{aligned}\beta &= -0.09(T_{compression} - M_s) + 22 \\ \beta &= -0.05(T_{tension\ or\ cold\ rolling} - M_s) + 12\end{aligned}\quad (5.15)$$

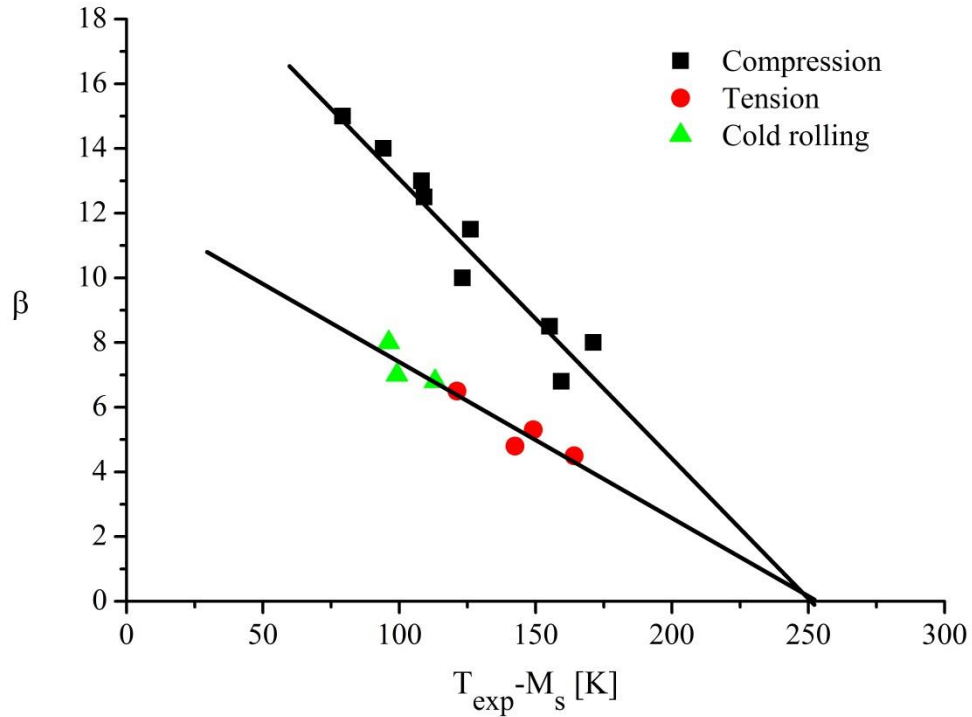


Figure 5.33 Relationship between austenite stability β and martensite-start temperature M_s . T_{exp} : experiment temperature by compression, tension and cold rolling, is equal to room temperature here.

Although the M_s temperature dependence of austenite stability β in tensile, cold rolled and compressed ADI is slightly different ($\beta \sim 0.09 \times M_s$ in compression and $\sim 0.05 \times M_s$ in tension and cold rolling), a fixed value of about 250 K between M_d and M_s in ADI is found for all samples. After inserting equation (5.15) into (3.4) the martensite phase transformation of ADI can be expressed using the martensite start temperature in the following form:

$$f_M/f_S = 1 - \exp\{[0.09(T_{compression} - M_s) - 22] \times (\varepsilon - \varepsilon_0)^n\}$$

$$f_M/f_S = 1 - \exp\{[0.05(T_{tension\ or\ cold\ rolling} - M_s) - 12] \times (\varepsilon - \varepsilon_0)^n\} \quad (5.16)$$

This allows predicting the resulting martensite phase fraction using the measured M_s temperature for ADI containing Ni. As the M_s temperature depends mainly on the chemical composition it is believed that it will also be possible to use this relationship for other phase compositions.

6. Summary

This research project had two main goals: First, using in-situ neutron diffraction to reveal the relationship between ausferritic transformation, austempering time and temperature in ADI materials during heat treatment. Some of the experimental studies in this dissertation are a direct continuation of previous studies on ausferrite transformation [Leop15, Lmei13, Psaa16] complementing and answering open questions that have not been explored in the previous investigations. Based on these results the second and main aim was then to establish and develop a model to describe the strain induced martensitic transformations in ADI. The issues addressed and the progress made in this dissertation will be introduced as follows.

Microstructure of ADI

The influence effects of austempering temperature, time and alloying element Ni on ADI materials and the whole process of phase transformation have been systematically presented in the previous work using optical microscope [Leop15, Lmei13, Psaa16]. The ausferrite microstructure in the ADI material is thought to consist of acicular ferrite (Width: several hundred nm, Length: 1~5 μm) and blocky retained austenite (Diameter: several μm) with coarser austenite/ferrite grains formed at higher austempering temperature and finer grains formed at lower austempering temperature. However, an opposite observation is found due to the results of neutron diffraction peak broadening analysis (section 5.2) and also in previous work [leop15], that a significant part of austenite/ferrite grains have their size in nanometer range rather than micronmeter range as previously observed. Although the observation results from SEM measurements (section 5.1.2) are mainly consistent with the results of optical microscopy used in the earlier studies, they additionally also show that austenite forms as films in the nanometer range on the developing ferrite needles. The TEM and APT investigations confirm that the actual grain size of austenite and ferrite is indeed concentrated in nanometer range, which austenite present as film and blocky structures (Fig. 5.2, 5.3, 5.4 and 5.5), and ferrite as subunits between the austenite films (Fig. 5.5). Furthermore the strain-induced martensite in ADI was found to form subgrain structures in the austenite films and twin structures in the blocky austenite (Fig. 5.8). In addition in blocky austenite grains of plastic deformed ADI, a new metastable ω phase of martensite has also been found using TEM and electron diffraction (SAED).

The observation results of TEM and APT also indicated that smaller nanometer ranged carbides and carbon clusters are present in the ferrite matrix, which provided important clues to the carbon gap problem.

The influence effect of austempering temperature on the austenite/ferrite grain size distribution has been illustrated in section 5.2 using characterization with SANS Showing that the austenite/ferrite grain size increases with arising austempering temperature (Fig. 5.13). The effect of plastic deformation on grain size distribution was also quantitatively characterized by SANS measurements. All grains are separated into smaller particles by the dislocations produced during the plastic deformation with nanometer sized martensite particles also forming inside the austenite grains during plastic deformation. With increasing deformation the width of the average grain size distribution also increases indicating that, part of the austenite/ferrite grains having a diameter larger than 1 μm (the blocky austenite), are separated into nanometer sized grains, however, those being larger than the initial average grain size before the plastic deformation (Fig. 5.14).

These results on the microstructure of ADI show that studying nanocrystalline material requires a combination of different methods to yield a more complete picture of the morphology.

Carbon distribution

The ausferritic transformation during austempering leads to redistribution of carbon atoms between retained austenite and ferrite. The carbon atoms diffuse from ferritic regions into the retained austenite and stabilize it. Using the changes in lattice parameter of austenite and ferrite before and after austempering as determined by synchrotron diffraction, the carbon contents in austenite and ferrite have been calculated. A substantial part of the carbon atoms which have been diluted into austenite after austenitization are missing in the retained austenite after quenching and subsequent austempering. These missing carbon atoms could not be detected directly by in-situ neutron diffraction [Loep15] or conventional metallographic method and are denoted as carbon gap firstly proposed in previous work [Lmei13]. With the help of APT analysis on single austenite/ferrite grains and TEM measurements, the missing carbon atoms were identified mainly in the form of nano-sized carbides and carbon clusters distributed in the ferrite matrix. In addition the in-situ synchrotron diffraction data indicate the formation of supersaturated ferrite with a linear relationship between austempering temperature and carbon content (at%) in ferrite being also confirmed by APT as shown in Figure 5.20. Supersaturated ferrite was found to exist in the ADI materials with austempering temperature below 425°C while the carbon content in the ferrite increases as austempering temperature decreases. The resulting carbon gap values in ADI with austempering temperatures are shown in Figure 5.23 being inversely proportional

to the austempering temperature. About 90% of carbon atoms in the carbon gap are present in form of carbides and carbon clusters with only 10% dissolved in the ferrite matrix.

Martensitic transformations kinetic

Metastable retained austenite will transform into martensite during plastic deformation. The texture formation of austenite and ferrite in ADI during plastic deformation was identified after calculating the orientation distribution function from the measured Pole figures. Accurate quantitative phase analysis of deformed ADI samples was possible using the Rietveld method taking into account the texture information. The accurate quantification of martensite formation during tensile, compressive and cold rolling deformation made it possible modelling the transformations kinetics in ADI. This model incorporates all the influence factors on martensite formation in just two parameters - the deformation mode and the austenite stability, respectively. Quantifying the austenite stability using M_s temperature further simplifies the description of martensitic transformations kinetic. A linear relationship between austenite stability and martensite start temperature was found depending on deformation mode. Using this relationship the content of the martensite phase fraction with plastic strain in ADI containing Ni can be predicted by directly measuring the M_s . However, as the M_s temperature depends mainly on the chemical composition it is believed that it will also be possible to use this relationship for other and arbitrary phase compositions.

7. References

- [Abha05] A. Bhattacharyya, D. Rittel and G. Ravichandran: *Scr. Mater.* (2005) Vol. 52, pp.657-661
- [Adbo17-1] A. D. Boccardo, P. M. Dardati, D. J. Celentano and L. A. Godoy: *Met. Mater. Trans. A* (2017) Vol. 48A, pp.524-535
- [Adbo17-2] A. D. Boccardo, P. M. Dardati, D. J. Celentano and L. A. Godoy: *Finite Elem. Anal. Des.* (2017) Vol. 134, pp.82-91
- [Agar15] A. Garcia-Junceda, C. Capdevila, F. G. Calallero and C. Garcia de Andres: *Scr. Mater.* (2008) Vol. 58, pp. 134-137
- [Ahal08] A. Haldar, S. Suwas, D. Bhattacharjee: *Microstructure and Texture in Steels and Other Materials* (2008): ISBN: 978-1-4471-6003-8
- [Ahei15] A. Heinemann and S. Mühlbauer: *Journal of large-scale research facilities*, 1, (2015) A10; <http://dx.doi.org/10.17815/jlsrf-1-32>
- [Aita95] A. Itami, M. Takahashi and K. Ushioda: *ISIJ International* (1995) Vol. 35, No.9 pp.1121-1127
- [Asto12] A. Stormvinter, A. Borgenstam and J. Agren: *Metall. Mater. Trans. A* (2012) Vol. 43, pp.3870-3879
- [Asto13] A. Stormvinter, P. Hedström and A. Borgenstam: *J. Mater. Sci. Technol.* (2013) Vol. 29, pp 373-379
- [Awie11] A. Wiengmoon: *Naresuan University Engineering Journal* (2011) Vol 6, No 1
- [Bewa50] B. E. Warren and B. L. Averbach: *J. App. Phys.* (1950) Vol. 21, pp. 595-599
- [Bkjh87] B. K. Jha, R. Avtar, V. Sagar Dewivedi and V. Ramaswamy: *J. of Mat. Sci. Letters* (1987) Vol. 6, pp. 891-893
- [Brsh14] B. R. Shendy, M. N. Yoozbashi, B. Avishan and S. Yazdani: *Acta Metall. Sinica* (2014) Vol. 27(2), pp. 233-238
- [Ccap03] C. Capdevila, F. G. Caballero and C. G. de Andrés: *Mater. Sci. Technol.* (2003) Vol. 19, pp. 581-586
- [Chcr50] C. H. Crussard and B. Jaoul: *Rev. Met.* (1950) Vol. 42, pp. 589-600
- [Chsh55] C. H. Shih, B. L. Averbach and M. Cohen: *AIME Trans* (1955) Vol.203, pp. 183-187
- [Clma70] C. L. Magee: *Phase Transformations, ASM*, (1970), pp. 115-156
- [Clma71] C. L. Magee: *Metall. Trans.* (1971), Vol.2, pp. 2419-2430
- [Cmfa09] C. M. Fang, M. A. van Huis and H. W. Zandbergen: *Phy. Rev. B* (2009) Vol. 80, 224108
- [Cmfa10] C. M. Fang, M. A. van Huis, M. H. F. Sluiter and H. W. Zandbergen: *Acta Mater.* (2010), Vol. 58, Issue 8, pp. 2968-2977
- [Csm92] C. S. Smith: A History of Martensite: Early Ideas on the Structure of Steel. In *Martensite, A tribute to M. Cohen*, G. B. Olson and W. S. Owen, Eds. ASM International: Materials Park, OH, USA, (1992), pp. 21–39

- [Dbal99] D. Balzar: Voigt-function model in diffraction line-broadening analysis; Microstructure Analysis from Diffraction, edited by R. L. Snyder, H. J. Bunge and J. Fiala, International Union of Crystallography (1999)
- [Dhsh07] D. H. Sherman, S. M. Cross, S. Kim, F. Grandjean, G. J. Long and M. K. Miller: *Metall. Mater. Trans. A* (2007) Vol. 38A, pp. 1698-1711
- [Dhto56] D. H. Tombouliau and P. L. Hartman: *Phy. Rev.* (1956) Vol. 102, pp. 1423-1447
- [Djla13] D. J. Larson, T. J. Prosa, R. M. Ulfing, B. P. Geiser and Th. F. Kelly: Local Electrode Atom Probe Tomography A User' Guide; (2013) XVII 318p; ISBN: 978-1-4614-8720-3
- [Dmys14] D. Myszk, E. Skolek and A. Wieczorek: *Arch. Metall. Mater.* (2014) Vol. 59 pp.1217-1221
- [Dpko59] D. P. Koistinen and R. E. Marburger: *Acta Metall.* (1959) Vol. 7, pp. 59-60
- [Drab94] D. Rabbe and K. Lücke: *In Textures of Materials ICOTOM-10* (1994) pp. 597-610
- [Drit02] D. Rittel, G. Ravichandran and S. Lee: *Mech. of Mater.* (2002) Vol.34 pp. 627-642
- [Eper12] E. Pereloma and D. V. Edmonds: *Phase transformations in steels* (2012); Woodhead Publishing Limited; ISBN 978-1-84569-971-0
- [Erpe70] E. R. Petty: *Martensite*, London: Longman (1970) p. 95
- [Esma52] E. S. Machlin and M. Cohen: *Trans. AIME* (1952) Vol. 194 p. 489
- [Esro46] E. S. Rowland and S. R. Lyle: *Trans. ASM* (1946) Vol. 37 pp.27-47.
- [Fbar10] F. Barcelo, J. L. Bechade and B. Fournier: *Phase transitions* (2010) Vol. 83, pp. 601-614
- [Fgca08] F. G. Caballero, M. K. Miller, C. Carcia-Mateo, C. Capdevila and C. Garcia de Andres: *The Member Journal of the Minerals, Metals & Materials Society* (2008) Vol. 60, No. 12 pp. 16-21; <http://www.tms.org/pubs/journals/JOM/0812/caballero-0812.html>
- [Fhai08] F. Hairer, A. Karelouva, C. Kremaszky, E. Werner, T. Hebesberger and A. Pichler: *Eching techniques for the microstructural characterization of complex phase steels by light microscopy* (2008); https://www.mtf.stuba.sk/docs/internetovy_casopis/2008/4mimorc/hairer.pdf
- [Fhuy15] F. Huyan, P. Hedström and A. Borgenstam: *Materials Today: Proceedings* (2015) Vol. 2, pp. 561-564
- [Gbol72] G. B. Olson and M. Cohen: *J. Less-Common Metals* (1972) Vol. 28, pp. 107-118
- [Gbol75] G. B. Olson and M. Cohen: *Metall. Trans. A* (1975) Vol. 6A, pp.791-795
- [Gfbo69] G. F. Bolling and R. H. Richman: *Philos. Mag.* (1969) Vol. 19, pp. 247-264
- [Gfbo70-1] G. F. Bolling and R. H. Richman: *Scr. Metall.* (1970) Vol. 4, pp. 539-543
- [Gfbo70-2] G. F. Bolling and R. H. Richman: *Acta Met.* (1970) Vol. 18, pp. 673-681

- [Gnha96] G. N. Haidemenopoulos and A. N. Vasilakos: *Mater. Tech.* (1996) steel research 67 No. 11 pp. 513-519
- [Hbun87] H. Bunge: *Int. Mater. Rev.* (1987) Vol. 32 pp. 265-291
- [Hcsh01] H. C. Shin, T. K. Ha and Y. W. Chang: *Scr. Mat.* (2001) Vol. 45, pp.823-829
- [Hjbu65] H. J. Bunge: *Z. Metallkde.* (1965) Vol. 56, pp. 872-874
- [Hjbu82] H. J. Bunge, H. R. Wenk and J. Pannetier: *Textures and Micro- structures* (1982) Vol. 5 pp. 153-170
- [Hkdh05] H. K. D. H. Bhadeshia, Hard bainite, In J. M. Howe, D. E. Laughlin, J. K. Lee, U. Dahmen, and W. A. Soffa, editors, *Solid→Solid Phase Transformations*, TME–AIME, Warrendale, USA, (2005) Vol.1, pp. 469–484
- [Hkdh82] H. K. D. H. Bhadeshia: *J. Mat. Sci.* (1982) Vol. 17, pp. 383-386
- [Hkdh90] H. K. D. H. Bhadeshia, J.W. Christian: *Metall. Trans. A* (1990) Vol. 21A, pp. 767-797
- [Hnha04] H. N. Han, C. G. Lee, C. S. Oh, T. H. Lee and S. J. Kim: *Acta Mater.* (2004) Vol. 52, pp.5203-5214
- [Hrwe03] H.-R. Wenk and S. Grigull: *J. Appl. Cryst.* (2003) Vol. 36, pp. 1040-1049
- [Hsun74] Hsun Hu: *Texture* (1974) Vol. 1, pp. 233-258
- [Hsya07] H. S. Yang and H. K. D. H. Bhadeshia: *Mat. Sci. and Tech.* (2007) Vol.23 No.5
- [Hyle10] H. Y. Lee, H. W. Yen, H.T. Chang and J.R. Yang: *Scr. Mater.* (2010) Vol. 62, pp. 670-673
- [Hyuu97] H. Y. Yu: *Metall and Mat Trans A* (1997) Vol.28, pp. 2499-2506
- [Hwsw52] H. W. Swift: *J. Mech. Phys. Solids* (1952) Vol. 1 No. 1
- [Jara97] J. Aranzabal, I. Gutierrez, J. M. Rodriguez-Ibabe and J. J. Urcola: *Metall. and Mat. Trans. A* (1997) Vol. 28A, pp.1143-1156
- [Jbur65] J. Burke: *Kinetics of Phase Transformation in Metals*, Pergamon Press, Oxford, United Kingdom, (1965)
- [Jbse13] J. B. Seol, D. Raabe, P. Choi, H. S. Park, J. -H. Kwak and C. G. Park: *Scr. Mater.* (2013) Vol. 68, pp. 348-353
- [Jchi11] J. Chiang, B. Lawrence, J. D. Boyd and A. K. Pilkey: *Mat. Sci. Eng. A* (2011) Vol. 528, pp.4516-4521
- [Jcer14] J. Cermak and L. Kral: *J. Alloys Compd.* (2014) Vol. 586 pp. 129-135
- [Jens03] J. Gründling, C. Bartels and U. Schliephake: *Konstruktion (Zeitschrift für Produktentwicklung und Ingenieur-Werkstoffe)*: Heft 6 (2003)/Heft 7-8 (2004)
- [Jgsp05] J. G. Speer, F. C. Rizzo Assunçao, D. K. Matlock and D. V. Edmonds: *Mater. Res.* (2005) Vol. 8 No. 4, pp. 417-423

- [Jila80] J. I. Langford: *In Accuracy in Powder Diffraction*, NBS Special Publication (1980) No. 567; edited by S. Block and C. R. Hubbard, pp. 255-269.
- [Jinw95] J. W. Kim, D. R. Peacor, D Tessier and F Elsass: *Clays and Clay Minerals* (1995) Vol. 43 No. 1, pp. 51-57
- [Jkoh13] J. Kohlbrecher: SASfit: A program for fitting simple structural models to small angle scattering data (2013)
- [Jlga03] J. L. Garin and R. L. Mannheim: *J Mater. Process Tech* (2003) Vol. 133-134, pp.347-351
- [Jmar99] J. Ma. Rincon and M Romero: Characterization techniques of glasses and ceramics (1999): ISBN 978-3-642-08348-8
- [Jmos90] J. Moser, H. Liao and F. Levy: *J. Phys. D: Appl. Phys.* (1990) Vol. 23, pp. 624-626
- [John00] John R. Keough and Kathy L. Hayrynen: *Society of Automotive Engineers* (2000): 2000-01-0764
- [Jspe03] J. Speer, D. K. Matlock, B. C. De Cooman and J. G. Schroth: *Acta Mater.* (2003) Vol. 51, pp. 2611-2622
- [Ksug92] K. Sugimoto, N. Usui, M. Kobayashi and S. Hashimoto: *ISIJ International* (1992) Vol. 32 No. 12, pp.1311-1318
- [Ksug92] K. Sugimoto, M. Kobayashi and S Hashimoto: *Metall. Trans. A* (1992) Vol. 23A, pp.3085-3091
- [Kwan65] K. W. Andrews: *J.I.S.I.*, (1965) Vol. 203, pp.721-727
- [Lafe87] L. A. Feigin and D. I. Svergun: *Structure Analysis by Small-Angle X-Ray and Neutron Scattering* (1987), Springer Science + Business Media New York, pp. 275-320; ISBN 978-1-4757-6626-4
- [Lbra07] L. Bracke, L. Kestens and J. Penning: *Scr. Mater.* (2007) Vol. 57, pp. 385-388
- [Leop15] Leopold Meier: *In-situ-Messung der Phasenumwandlungskinetik von ausferritischem Gusseisen* (2015), Dissertation, TU München
- [Llut97] L. Lutterotti, S. Matthies, H.-R. Wenk, A. J. Schultz and J. Richardson: *J. Appl. Phys.* (1997) Vol.81, pp. 594-600
- [Lmei13] L. Meier, M. Hofmann, P. Saal, W. Volk and H. Hoffmann: *Mater. Char.* (2010) Vol. 85, pp. 124-133.
- [Mdah89] M. Dahms and H. J. Bunge: *J. Appl. Cryst.* (1989) Vol.22, pp.439-447
- [Mfer94] M. Ferrari and L. Lutterotti: *J. Appl. Phys.* (1994) Vol. 76 (11), pp.7246-55
- [Mgst88] M. G Stout, J. S Kallend, U. F Kocks, M. A Przystupa and A. D Rollett: *In Eighth Int. Conf. on Texture of Materials* (1988) pp. 479-484

- [Mhoe13] M. Hoelzel, W. M. Gan, M. Hofmann, C. Randau, G. Seidl, P. Juettner and W. W. Schmahl: *Nuclear Instruments and Methods in Physics Research A* (2013) Vol. 711, pp.101-105
- [Mhoe15] M. Hoelzel, A. Senyshyn and O. Dolotko; *J. large-scale research facilities*, (2015) Vol. 1 A5
- [Mhof15] M. Hofmann, W. M. Gan und J. Rebelo-Kornmeier: *J. of large-scale research facilities* (2015) Vol.1 A6; <http://dx.doi.org/10.17815/jlsrf-1-25>
- [Mmaa10] M. Maalekian and E. Kozeschnik: *Mater. Sci. For.* (2010) Vol. 638-642, pp. 2634-2639
- [Moka90] M. Oka, H. Okamoto, K. Ishida: *Metall. Trans. A* (1990) Vol. 21A, pp. 845-851
- [Msud81] M. Sudo, S. Hashimoto and I. Tsukatani: *In Sixth Int. Conf. on Textures of Materials* (1981) pp. 1076-1085
- [Mume75] M. Umemoto and W.S. Owen: *Metall. Trans.* (1975) Vol. 5, 2041.
- [Mvil14] M. Villa, M. A. J. Somers and K. pantleon: *Isothermal Martensite Formation*. (2014) Kgs. Lyngby: DTU Mechanical Engineering
- [Norb14] N. Schell, A. King, F. Beckmann, T. Fischer, M. Müller and A. Schreyer: *Mate. Sci. Forum* (2014) Vol. 772, pp. 57-61
- [Ntsu00] N. Tsuchida and Y. Tomota: *Mater. Sci. Eng.* (2000) Vol. A285 pp. 345-52.
- [Omat87] O. Matsumura, Y. Sakuma and H. Takechi: *Scri. Met.* (1987) Vol. 21, pp.1301-06.
- [Psaal16] P. Saal, L. Meier, X. H. Li, M. Hofmann, M. Hoelzel, J. N. Wagner and W. Volk: *Metall. Mater. Trans. A* (2016) Vol. 47, pp.661-671, DOI: 10.1007/s11661-015-3261-1
- [Ragr46] R. A. Grange and H. M. Stewart: *Trans. AIME* (1946) Vol. 167 pp.467-490.
- [Rajn14] Rajnovic D., Eric Cekic O., Labus D., Dramicanin M., Balos S. and Sidjanin L. (2014) ICM Poster (The microstructure characterization of unalloyed austempered ductile iron)
- [Rece56] R. E. Cech and D. Turnbull: *Trans. AIME* (1956) Vol. 206, pp. 124-132.
- [Rgst92] R. G. Stringfellow, D. M. Parks and G. B. Olsen: *Acta Metall Mater.* (1992) Vol.40, pp.1703-1716
- [Rhri71] R. H. Richman and G. F. Bolling: *Met. Trans.* (1971) Vol.2, pp. 2451-2462
- [Rjas85] R. J. Asaro and A. Needleman: *Acta Metall.* (1985) Vol.33 No.6, pp. 923-953
- [Rjro65] R. J. Roe: *J. Appl. Phys.* (1965) Vol. 36, pp. 2024-2069
- [Rkra93] R. K. Ray, J. J. Jonas and R. E. Hook: *Int. Mater. Reviews* (1993) Vol. 39, pp. 129-172

- [Rpfe13] R. Pfeifer, C. W. Müller, C. Hurschler, S. Kaierle, V. Wesling and H. Haferkamp: *Procedia CIRP* 5 (2013) pp. 253-258
- [Rund04] RUNDMAN, K. B.: “*It’s About Austenite and Carbon, Mate*” -A Story of the *Physical Metallurgy of ADI - Part II* (35th Australian Foundry Institute National Conference). Adelaide, 2004
- [Sdan70] S. D. Antolovich and B. Singh: *Metall. Trans.* (1970) Vol. 1, pp. 3463-3465
- [Smcv09] S. M. C. Van Bohemen and J. Sietsma: *Metal. Mater. Trans. A* (2009) Vol. 40, pp. 1059-1068
- [Smcv12] S. M. C. van Bohemen: *Mater. Sci. Techn.* (2012) Vol. 28 No.4.
- [Srbo94] S. R. Bodner and M. B. Rubin: *J. Appl. Phys.* (1994) Vol. 74, pp. 2742-47
- [Srpa67] S. R. Pati: Dissertation “Nucleation of the isothermal martensitic transformation in Iron-Nickel-Manganese alloys” (1967): MIT
- [Ssuw14] S. Suwas, R.K. Ray: *Crystallographic Texture of Materials* (2014): ISBN: 978-1-4471-6313-8
- [Tiwa98] T. Iwamoto, T. Tsuta and Y. Tomita: *Int. J. Mech. Sci.* (1998) Vol. 40, No. 2-3, pp. 173-182
- [Twli15] T. Liu, D. Zhang, Q. Liu, Y. Zheng, Y. Su, X. Zhao, J. Yin, M. Song and D. Ping: *Sci. Rep.* (2015) 5, 15331; doi: 10.1038/srep15331
- [Ufko98] U. F. Kocks, C. N. Tome and H.-R. Wenk: *Texture and Anisotropy* (1998): ISBN 0 521 46516 8
- [Vaya14] V. A. Yardley and E. J. Payton: *Mater. Sci. Tech.* (2014) Vol. 30, pp. 1125-1130
- [Vcol09] V. Colla, M. De Sanctis, A. Dimatteo, G. Lovicu, A. Solina and R. Valentini: *Metall. and Mater. Trans. A* (2009) Vol. 40, pp. 2557-67
- [Wboh15] W. Böhme and L. Reissig: *Adv. Eng. Mater.* (2015) Vol. 17 No.8, pp.1189-1196
- [Wgon13] W. Gong, Y. Tomota, Y. Adachi, A. M. Paradowska, J. F. Kelleher and S. Y. Zhang: *Acta Mater.* (2013) Vol. 61, pp. 4142-4154
- [Will68-01] Williams RO: *J. App. Phys* (1968) Vol. 39, pp. 4329-4335
- [Will68-02] Williams RO: *Trans. Metall. Soc. AIME* (1968) Vol. 242, pp. 105-115
- [Wrei08] W. Reimers, A. R. Pyzalla, A. Schreyer and H. Clemens: *Neutrons and Synchrotron Radiation in Engineering Materials Science*: WILEY-VCH Verlag GmbH & Co. KGaA, Weinheim: ISBN 978-3-527-315338
- [Wste56] W. Steven and A. G. Haynes: *J. Iron Steel Inst.* (1956) Vol. 183, pp. 349-359
- [Www-01] <http://www.mlz-garching.de/instrumente-und-labore.html>
- [Www-02] <https://commons.wikimedia.org/wiki/File:Fe-C.svg>
- [Yguo15] Y. Guo, K. Feng, F. Lu, K. Zhang, Z. Li, S. R. E. Hosseini and M. Wang: *Appl. Sur. Science* (2015) Vol. 357, pp. 309-316

- [Yohm01] Y. Ohmori: *ISIJ Int.* (2001) Vol.41, pp. 554-565
- [Yohm96] Y. Ohmori, Y.-C. Jung, H. Ueno, K. Nakai, H. Ohtsobo: *Mater. Trans., JIM*, (1996) Vol. 37, pp. 1665-1671
- [Yywe14] Y. Y. Wen, F. Huang, Y. H. Rong and Z. H. Guo: *International Conference on Material Science and Material Engineering* (2014), pp. 209-213
- [Zjia95] Z. Jiang, Z. Guan and J. Lian: *Mate.s Sci. Eng. A* (1995) Vol. 190, pp. 55-64
- [Znis78] Z. Nishiyama: *Martensitic Transformation* (1978), Academic Press INC: ISBN 0-12-519850-7

8. Attachment

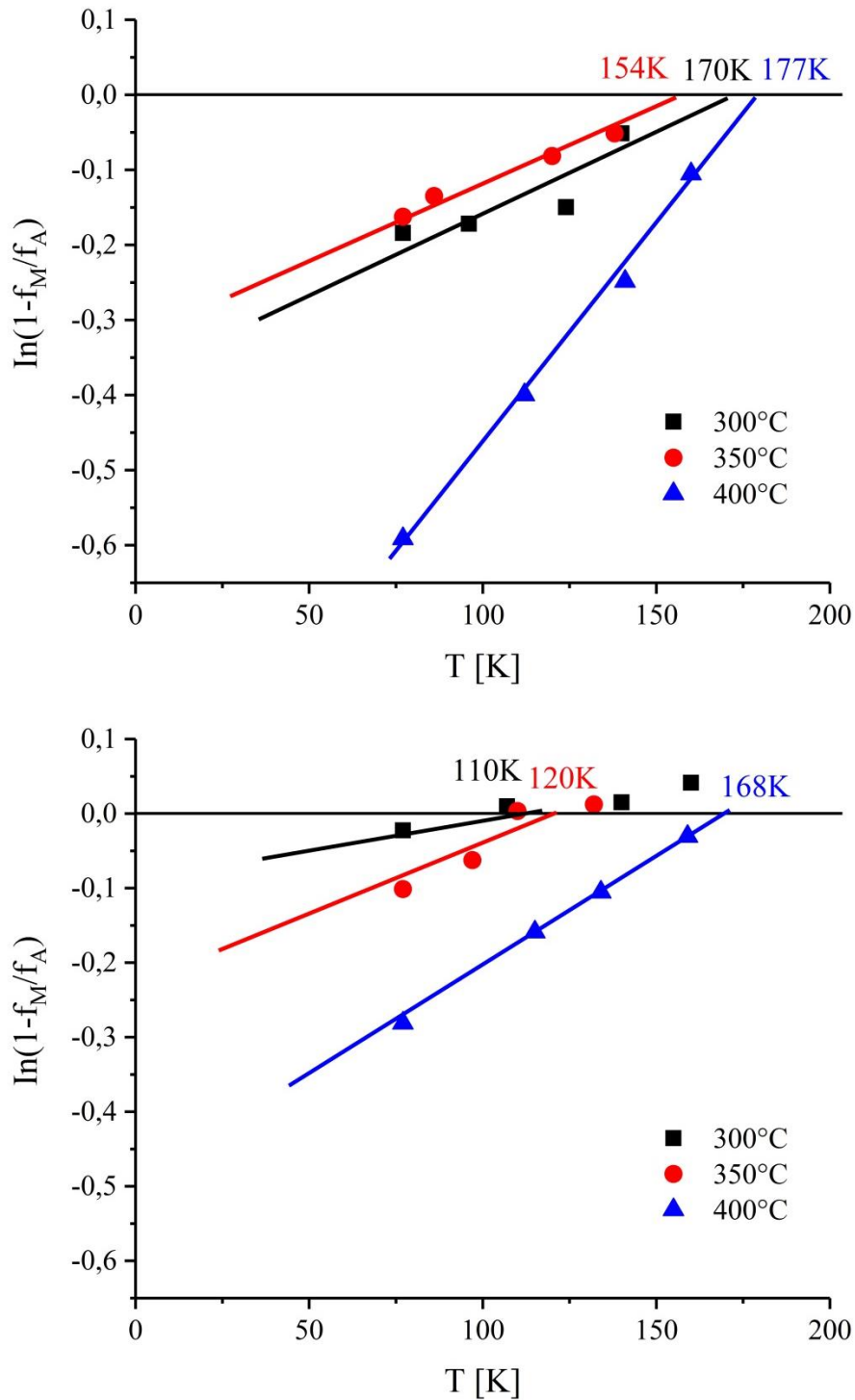


Figure 8.1 Resulting martensite volume fraction of ADI samples with (top) 0.5 wt% Ni , (bottom) 1.5 wt% Ni (austempered at 573 K (300 °C) , 623 K (350 °C) and 673 K (400 °C)) versus quenching temperature. The lines are fits using the Koistinen-Marburger relation, with resulting M_s temperatures also shown at the intercept with the T axis.

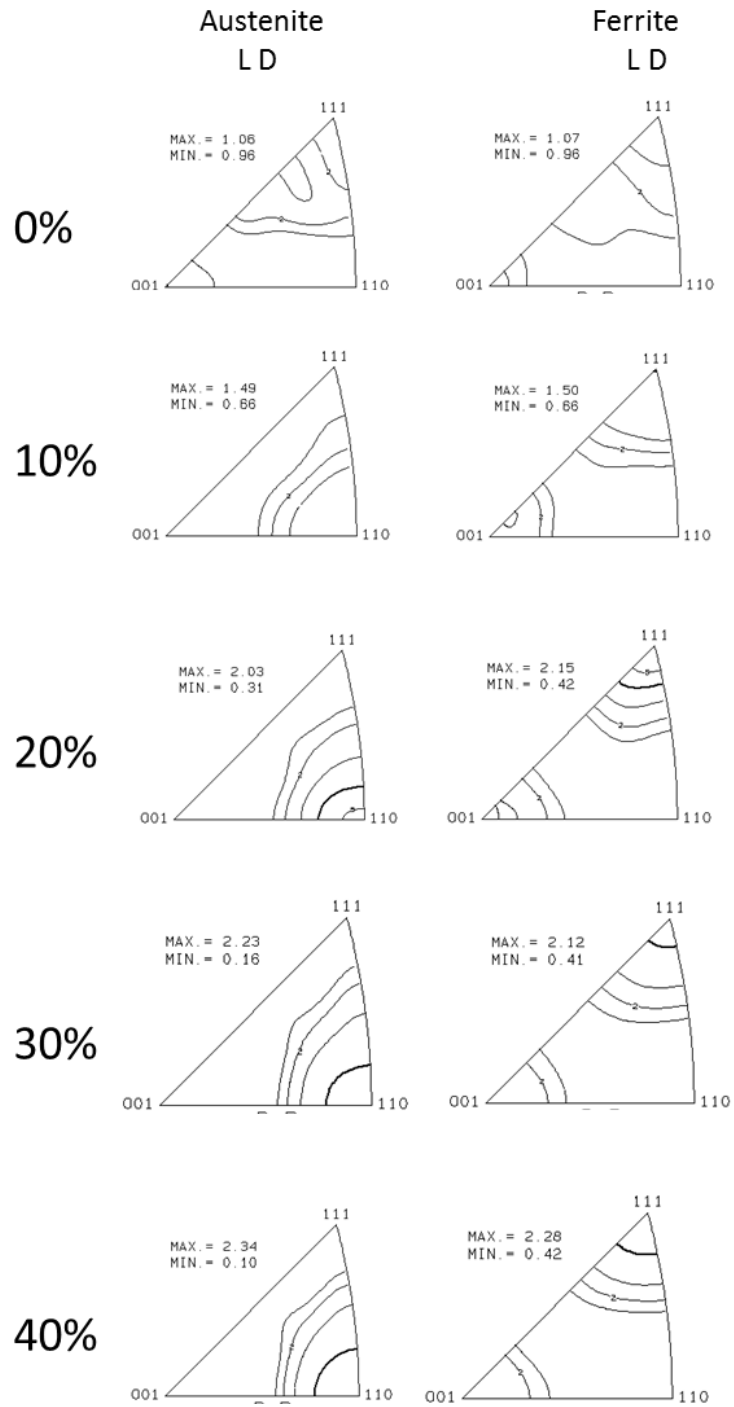


Figure 8.2 Inverse pole figures of austenite and ferrite phases in compressive deformed ADI (austempered at 350°C) for different strain levels up to 40%.

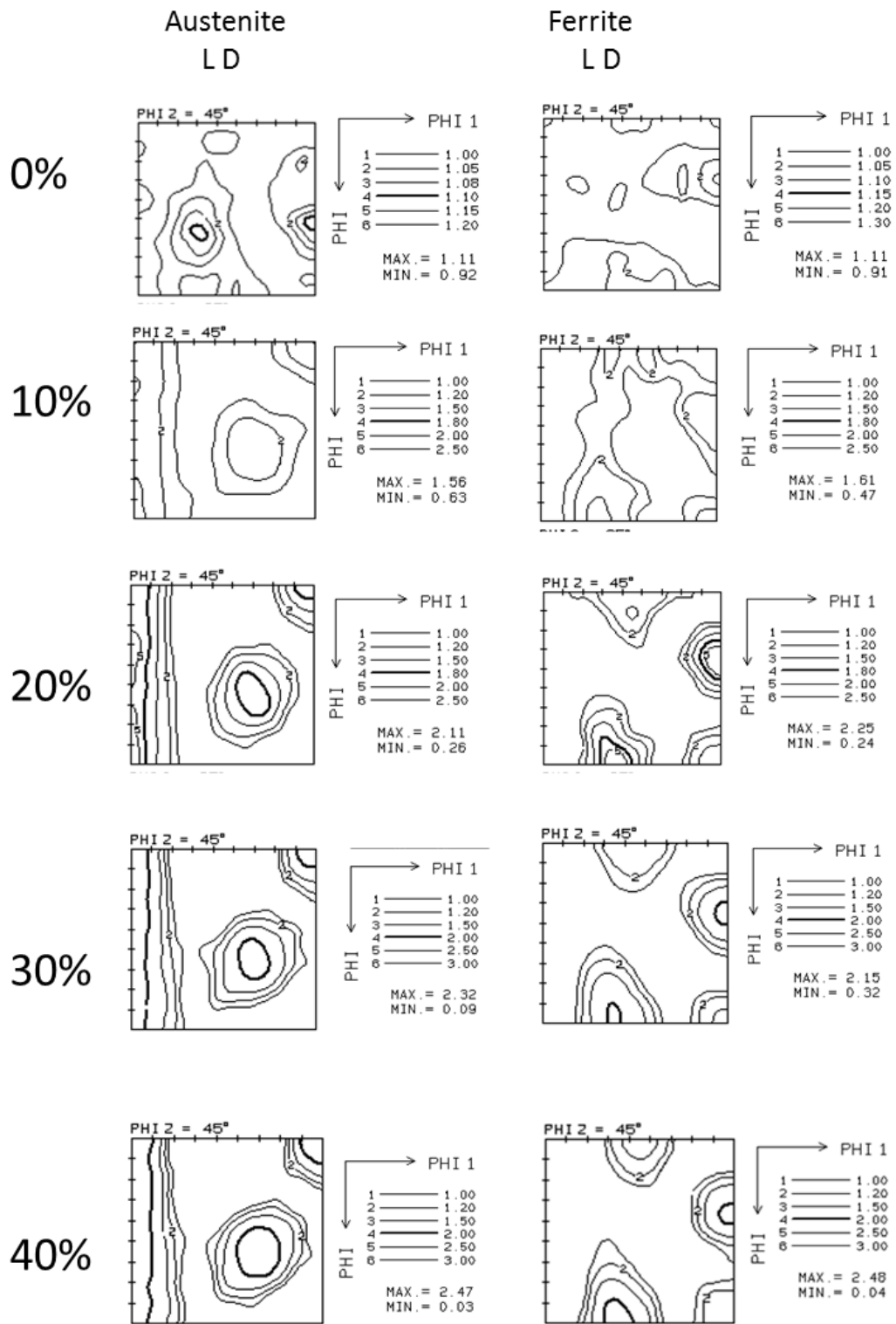


Figure 8.3 ODFs of austenite and ferrite phases in compressive deformed ADI (austempered at 350°C) for different strain levels up to 40%.

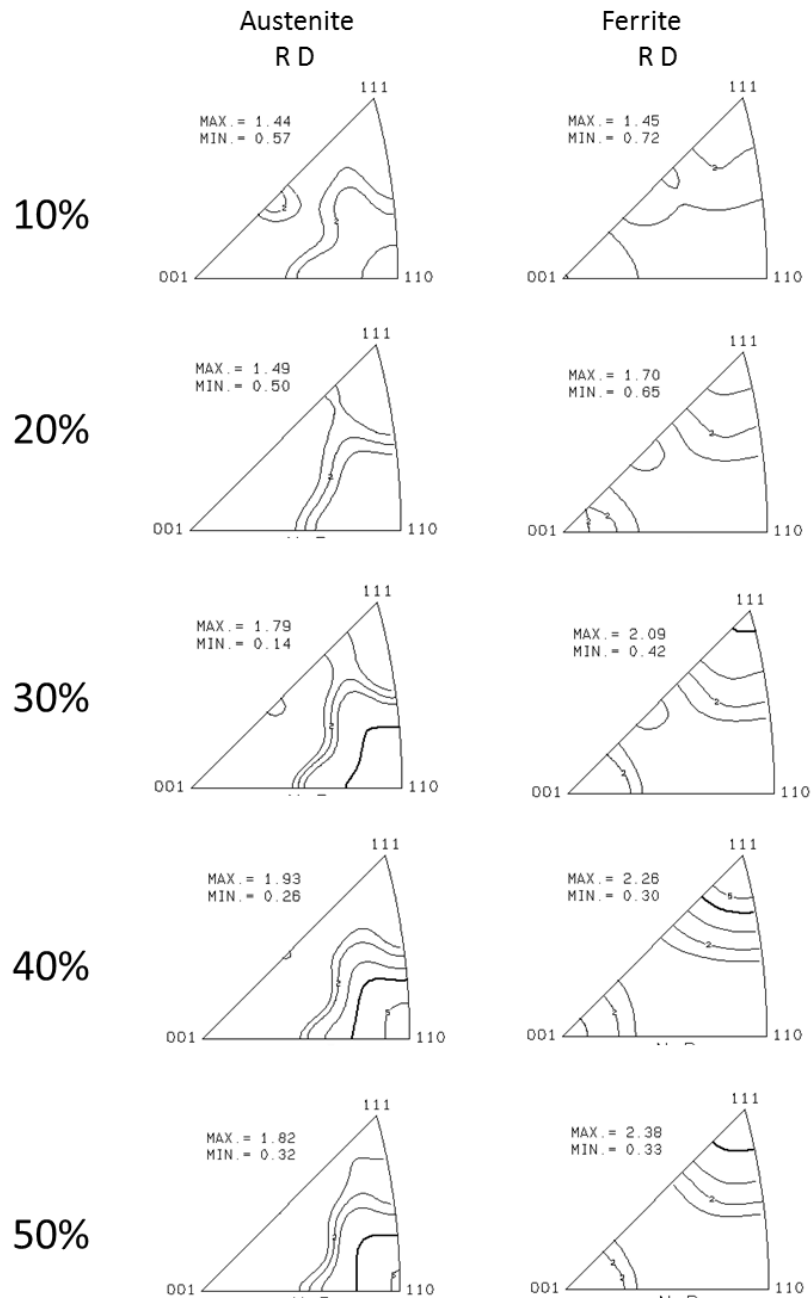


Figure 8.4 Inverse pole figures of austenite and ferrite phases in cold rolled ADI (austempered at 350°C) for different strain levels up to 50%.

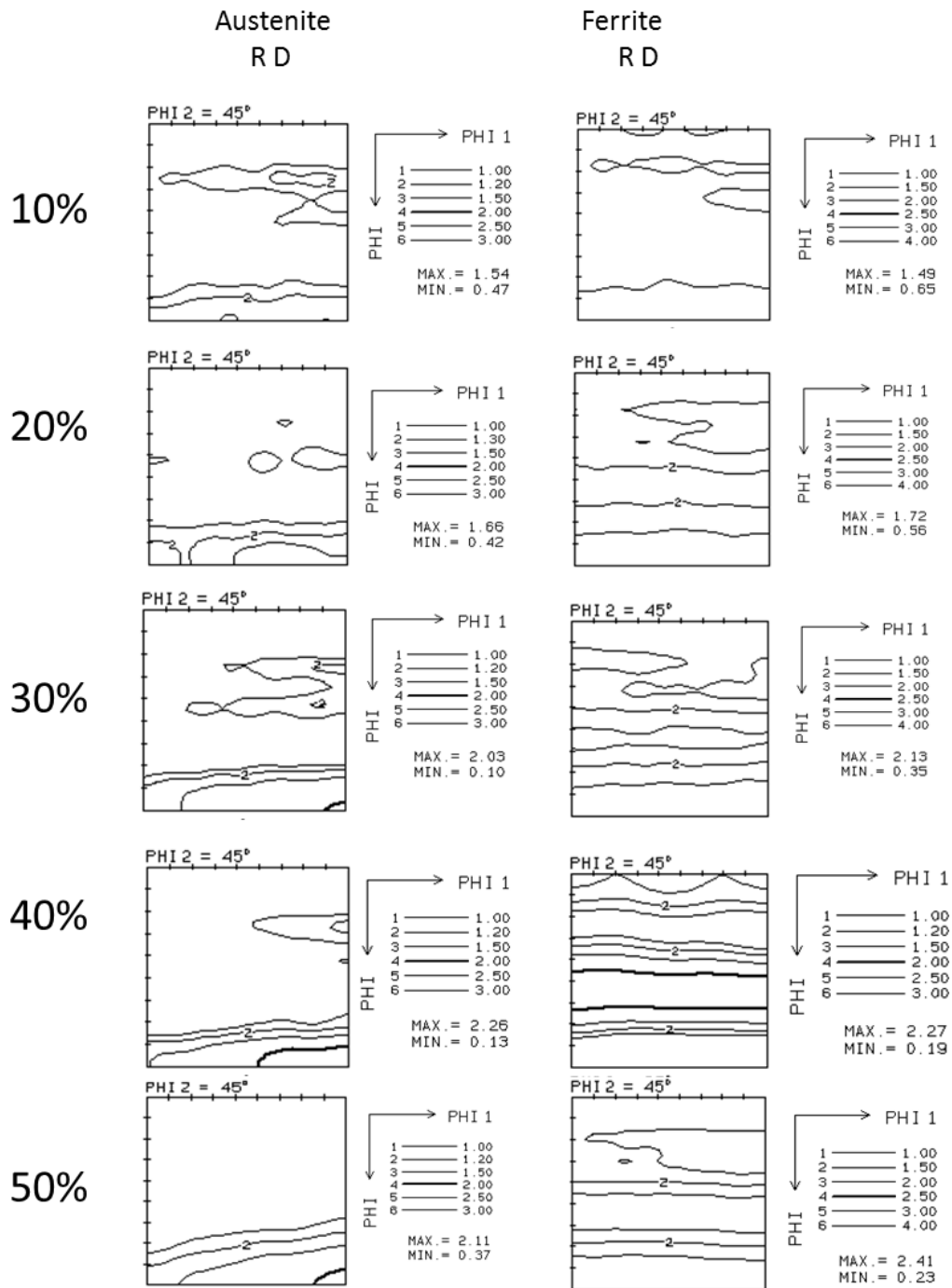


Figure 8.5 ODFs of austenite and ferrite phases in cold rolled ADI (austempered at 350°C) for different strain levels up to 50%.

9. Own Publications:

- [1] X. H. Li, P. Saal, W. M. Gan, M. Landesberger, M. Hoedel and M. Hofmann: “Strain Induced Martensitic Transformation in Austempered Ductile Iron (ADI)”, J. Physics: Conference Series (2016) 746 012055, DOI: 10.1088/1742-6596/746/1/012055
- [2] P. Saal, L. Meier, X. H. Li, M. Hofmann, M. Hoedel, J. N. Wagner and W. Volk: “In Situ Study of the Influence of Nickel on the Phase Transformation Kinetics in Austempered Ductile Iron”, Metall. Mater. Trans. A (2016) Vol. 47, pp.661-671, DOI: 10.1007/s11661-015-3261-1
- [3] X. H. Li, P. Saal, W. M. Gan, M. Hoedel, W. Volk, W. Petry and M. Hofmann: “Strain-Induced Martensitic Transformation Kinetic in Austempered Ductile Iron (ADI)”, Metall. Mater. Trans. A (2017), <https://doi.org/10.1007/s11661-017-4420-3>
- [4] X. H. Li, J. N. Wagner, A. Heinemann, G. J. Cao, W. Petry and M. Hofmann: “Carbon redistribution and morphology of ausferrite in Austempered Ductile Iron (ADI)”, in preparation